Free-standing Cu-based NanoZymes for colorimetric sensing of glucose in human urine

A thesis submitted in fulfilment of the requirements for the degree of

Master of Science

Sanjana Naveen Prasad

Bachelor of Engineering (Biotechnology) – Visvesvaraya Technological University

School of Science

College of Science, Engineering and Health

RMIT University

September 2019

Declaration

I certify that except where due acknowledgment has been made, the work is that of the author alone; the work has not been submitted previously, in whole or in part, to qualify for any other academic award; the content of the thesis is the result of work which has been carried out since the official commencement date of the approved research program; any editorial work, paid or unpaid, carried out by a third party is acknowledged; and, ethics procedures and guidelines have been followed.

Sanjana Naveen Prasad

30/09/2019

Acknowledgments

I take this opportunity to express my sincere gratitude to everyone who has been a part of my journey. Your generous support and encouragement will always be appreciated. All the memories and influences I've had towards making me a better person that will forever be treasured.

First and foremost, I want to thank my supervisor *Prof. Vipul Bansal* for believing in me and giving me this opportunity to begin a career in research. The chance he has given me to be part of his fantastic research group at *NanoBiosensing Research Laboratory* has helped me grow both personally and professionally. His concern and support throughout my candidature will never be forgotten. His extensive knowledge in multi-disciplinary areas, critical thinking, and perseverance for excellence motivates me to work harder. Watching him analyse a problem during weekly group meetings was truly inspiring. I am extremely glad to have him as my mentor.

I am extremely grateful to *Dr Rajesh Ramanathan*, my supervisor for his invaluable guidance throughout my candidature. His constant encouragement to believe in myself has helped me face tricky situations. The mentoring opportunities he has given me have been a rewarding experience that helped improve my communication and problem-solving skills. I will always be indebted for his time and patience with me. His constant strive for perfection and constructive criticism pushed me to do better in all of my endeavours. His occasional pep-talks have lifted my spirits whenever I wasn't doing well. I thank him for inspiring and motivating me.

I could not have done any of this without the support and encouragement from my parents, *Indira* and *Naveen Prasad.* Their constant belief in me is highly motivating especially when I doubt myself. They always made sure to provide everything necessary, so I had little to worry

about. All the hour-long phone calls have been well-needed breaks to catch up and I very much appreciated them. I am eternally grateful for their advice and guidance.

I would also like to thank *Prof. Ewan Blanch* and *Dr James Tardio* for their comments and encouragement provided during my progress reviews of candidature. Special thanks to *Dr Ravi Shukla* for helping me look at the big picture of any research. I appreciate the help provided by the technical staff at the School of Science, *Mrs Zahra Homan, Mrs Ruth Cepriano-Hall, Mr Bebeto Lay, Mrs Nadia Zakhartchouk, Mr Frank Antolasic, Mr Zeyad Nasa, Dr Lisa Dias,* and *Mrs Claire Bayly.* My special thanks to *Dr Babu Iyer* for all the help with laboratory resources and management. I would also like to thank the staff of RMIT Microscopy and Microanalysis Facility, especially the duty microscopists for always being around to help.

I will take this opportunity to also thank all my friends and colleagues at *NanoBiosensing Research Laboratory* for their helpful comments suggestions during group meetings. I am grateful to *Sam Anderson, Dr Pabudi Weerathunge,* and *Dr Nurul Karim* for always being around to guide me. I am grateful to *Pyria Mariathomas* and *Sabeen Hashmi* for always showing me the bright side when I was being too hard on myself. Our celebratory lunches will be cherished.

Sanjana Naveen Prasad

Table of Contents

List of Figures

CHAPTER 1: Introduction

CHAPTER 2: Characterization techniques

CHAPTER 3: Copper nanoparticles embedded within a matrix of cotton fabric as recoverable NanoZyme catalyst for the colorimetric detection of glucose in urine

List of Tables

CHAPTER 1: Introduction

CHAPTER 3: Copper nanoparticles embedded within a matrix of cotton fabric as recoverable NanoZyme catalyst for the colorimetric detection of glucose in urine

CHAPTER 4: Galvanic replacement mediated synthesis of peroxidase-mimicking bimetallic nanoparticles as free-standing NanoZyme catalysts for the colorimetric detection of glucose in urine

ABSTRACT

Glucose is one of the most critical metabolites in our body, and the abnormality in its concentration range is associated with a variety of diseases and disorders. Therefore, accurate sensing of glucose in different body fluids is of high biomedical significance. A commonly known such disease is *Diabetes mellitus*, which is increasing globally with an alarming rate. An important aspect of diabetes management is to regularly monitor glucose levels. Although glucose detection in blood is rather easy by using low-cost commercial devices, renal glycosuria is another important condition that is commonly observed in patients with extended period of high glucose levels or in Type I juvenile diabetes. This condition leads to the excretion of glucose in urine. This is also a common occurrence in patients with Fanconi syndrome, and many other disorders. As such, the urine glucose levels can be considered as reliable indicators for screening patients with high glucose levels. Urine glucose test strips are commercially-available, however, they suffer from limited sensitivity in the human body-relevant glucose concentration range. Further, these urine test strips are time-sensitive *i.e*. the color response varies even if the strip is read within 1 min error interval of the recommended time. This tends to lead to false-positives.

As such, the glucose monitoring tools typically employ a combination of glucose oxidase (GOx) and Horseradish peroxidase (HRP) enzymes for glucose detection. In this reaction, GOx oxidises glucose to produce gluconic acid and H_2O_2. The H_2O_2 is then either detected electrochemically (in commercial blood glucose monitoring strips) or it serves as a substrate for HRP to catalyse the conversion of a non-colored substrate to a colored product (in pathological tests). A potential drawback of this system is that the HRP can be easily inactivated by H_2O_2. A viable alternative to using HRP is more robust artificial enzymes. A recent discovery that certain nanoparticles can show enzyme-mimic activity (commonly

referred to as NanoZymes) can offer a potential solution, wherein HRP is replaced with nanoparticles with peroxidase-mimic activity. While such solution-based NanoZymes have shown promise in glucose sensing, they are limited to detecting pM to µM concentrations of the analyte, while the concentration of glucose in urine is in the mM range. Keeping this aspect in mind, this thesis attempts to develop a sensing system that can detect glucose in the biologically-relevant range. This is achieved by loading catalytically active copper nanoparticles as NanoZymes on high surface area templates such as cotton fabric (**Chapter 3**), and subsequently further improving the ability to detect glucose colorimetrically by creating free-standing bimetallic NanoZymes on the surface of cotton fabric (**Chapter 4**).

In the first working chapter of this thesis (Chapter 3), the outstanding catalytic properties of copper nanoparticles embedded within the 3D matrix of cotton fabric (Cu@Fabric) is established. This is the first time that the catalytic activity of a NanoZyme is observed to result in the generation of the second oxidation product of the peroxidase substrate, TMB (3,3',5,5' tetramethylbenzidine) at mildly acidic conditions. Notably, this process typically requires highly acidic conditions (pH 1). The absorbent and porous nature of the template in combination with the inherent high catalytic activity of copper nanoparticles appears to be responsible for this outstanding catalytic performance. Considering the high catalytic activity, the HRP in the typical glucose sensing system is subsequently replaced with the Cu@Fabric NanoZyme to effectively quantify glucose in the biologically-relevant concentrations even in the presence of complex biological matrix of urine.

To further improve the colorimetric response and stability of the Copper@Fabric (decrease the leaching of the copper during assay), in Chapter 4 of this thesis, the copper is galvanically replaced with small quantities of noble metals to create bimetallic fabrics. Considering that bimetallic nanomaterials display enhanced catalytic properties over their

individual counterparts, the bimetallic fabrics obtained after the galvanic replacement reactions showed improved peroxidase-mimicking catalytic activity. Among the four bimetallic systems (Cu-Au, Cu-Ag, Cu-Pd and Cu-Pt), the Cu-Pt@Fabric NanoZyme showed the highest initial rate of the reaction. The formation of the bimetal also reduced the surface oxidation of copper as well as the leaching of Cu ions during glucose sensing assays. The improved stability resulted in higher recovery and reduced standard deviation of the glucose sensing system in comparison to the pristine Cu@Fabric used in Chapter 3. The bimetal system also showed a more intense colorimetric response which is attributed to the fact that the bimetallic NanoZyme system did not favour the double oxidation of TMB.

Overall, this thesis makes an important contribution towards highly accurate, user-friendly colorimetric sensing of glucose in urine in biologically-relevant range, which is likely to be of high clinical and commercial interest.

CHAPTER 1

Introduction

This chapter gives an overview of the field of nanotechnology including the syntheses approaches for nanoparticles and its application in different fields. Specifically, the application of nanomaterials in sensing and as a catalyst is detailed. In particular, emphasis is given to the new field of using nanoparticles as an enzyme-mimicking catalyst, commonly referred to as NanoZymes in the field of sensing. The gaps in research with respect to this field is discussed leading into the reasons to perform the research in this thesis is explained. At the end, a chapter-wise breakdown of the thesis is given along with a brief containing the information presented in each chapter.

1.1 Nanotechnology

It has been sixty years since the idea of nanotechnology was first introduced by Nobel Laureate Richard P. Feynman. In his lecture dated on the 29th December 1959 at the American Physical Society meeting at Caltech titled "*There's Plenty of Room at the Bottom*", Feynman discussed the possibility of controlling the behaviour of materials by manipulating them at the nanoscale [1]. Following this with Prof. N. Taniguchi's coining of the term '*Nanotechnology*' in 1974 and the publication of Engines of Creation by Eric Drexler, the field of nanotechnology received considerable attention influencing widespread research into the development of a suite of nanomaterials and understanding their properties [2, 3].

Nanotechnology plays an essential role in the primary level of atoms and molecular composition of materials in both organic and inorganic systems [4]. It is best described as the set of technological processes improved by the amalgamation of various fields of science such as physics, chemistry, biology, electronics, materials science and engineering [5]. The word '*nano'* originates from the Greek word *nanos* that means one billionth (10^{-9}) of a unit. In general, nanotechnology concerns the understanding, design, fabrication, and manipulation of materials at one billionth of a meter (10^{-9} m) level. This gives rise to interesting optical, electronic, and physical properties. Therefore, it is of no surprise that nanotechnology has found applications in energy, electronics, manufacturing, healthcare, information, and biotechnology, thus transforming the creation of new technologies [6, 7].

1.1.1 Nanomaterials

Any material is considered as a nanomaterial if at least one of its dimensions is below 100 nm [8]. Nanomaterials exhibit unique physical, optical, electrical, chemical, mechanical and biological properties from their bulk counterparts [9]. For example, the ferromagnetism of iron oxide shifts to superparamagnetism at the nanoscale [10]. Gold nanomaterials display

surface plasmon resonance (SPR) resulting in different colors ranging from red, orange or even blue depending on their size and shape while bulk gold is yellow in color [11]. Size, shape, composition, interface, structural features, and defects influence the unique physicochemical properties of nanomaterials [11-15]. To understand these properties and their potential applications it is essential to develop synthesis approaches. Nanomaterials are synthesized by two methods *viz*. 'top-down' approach or 'bottom-up' approach (**Figure 1.1**) [9, 16, 17].

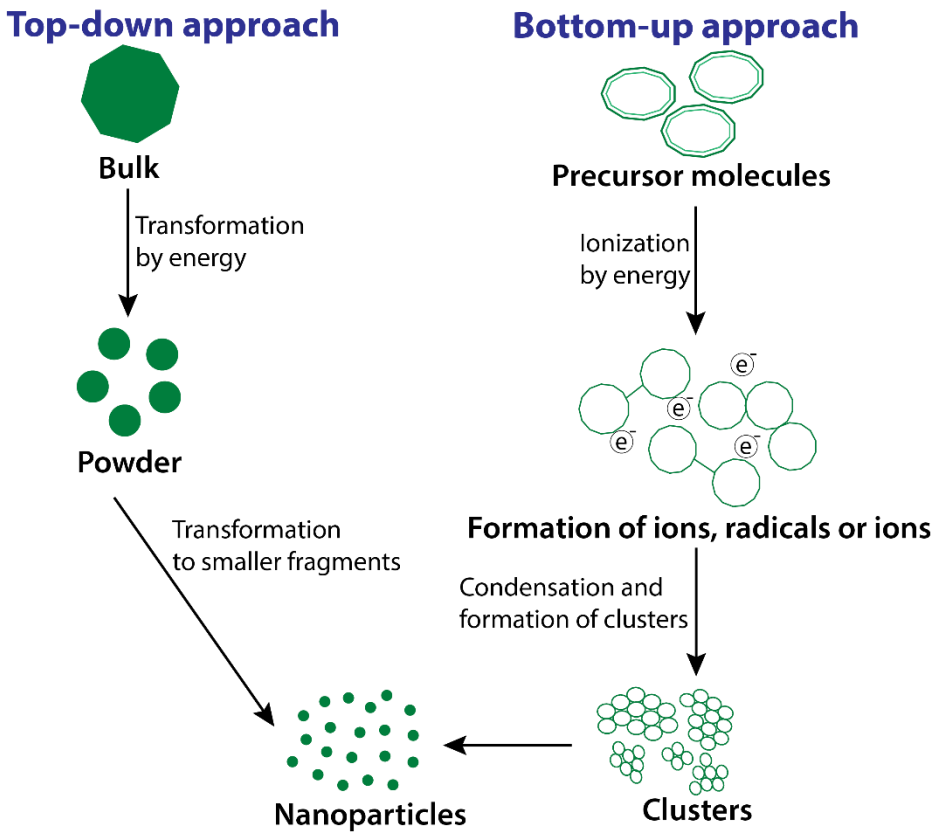

Figure 1.1 *Schematic representation of top-down and bottom-up approaches for nanomaterial synthesis.*

In the top-down synthesis method, bulk components are broken down into smaller units by slicing or successively removing the building blocks of the bulk material using chemical, mechanical or another form of energy, thereby leaving behind nanostructures. Typical top-down approaches include attrition or milling, lithography (photolithography,

electron beam lithography), sputtering, etching, laser ablation, electrospinning [18]. In bottom-up synthesis approach, nanomaterials are built up an atom, molecule or cluster at a time *via* self-assembly or chemical reaction. The atomic or molecular precursors gradually assemble, or the precursor particles grow in size until the desired nanostructure arrangement is realized. Some of the commonly reported bottom-up approaches include plasma arcing, hydrothermal/solvothermal, matrix-mediated processing, sol-gel, reverse micelle method, sonochemical, self-assembly, chemical vapour deposition, and chemical vapour condensation [18].

1.1.2 Metal nanoparticles

Nanomaterials are categorized depending on the number of their dimensions that fall in the nanoscale [19]. Nanoparticles are zero-dimensional where all their dimensions lie in the nanoscale. Nanoparticles are made up of several atoms or molecules and can vary in size and morphology. They display unique physical properties owing to their small size, large surface area and quantum tunneling effect [18]. Of the different kind of nanoparticles, metal nanoparticles of copper, gold, silver, platinum, and palladium have been widely investigated for their rich optical [20, 21], catalytic [21-23], and antimicrobial properties [24, 25]. Therefore, it is unsurprising to see its applicability in various fields and new technologies [11, 26-29].

For the synthesis of metal nanoparticles, a bottom-up approach is popular. During fabrication, a few desirable characteristics of the resulting nanoparticles are kept in mind such as (i) uniform size distribution, (ii) uniform shape or morphology, and (iii) identical composition *i.e.*, the core and surface composition of individual particles must be the same. The various synthesis techniques are grouped into two broad approaches; thermodynamic equilibrium and kinetic. In the thermodynamic equilibrium approach, a three-step process of

(i) supersaturation generation, (ii) nucleation and (iii) growth is involved [9]. Nanostructured metal colloids are typically synthesized by chemical reduction of metal complexes. Various precursors, reducing reagents and other chemicals are used to either promote or control the formation of preliminary nuclei and consequent growth of nanoparticles. Transition metal salts reduce in the presence of stabilizing agents in organic or aqueous media to form zerovalent metal colloids [30]. During nucleation, metal salts reduce to zerovalent atoms of the metal, which then go on to collide with other metal ions, atoms or clusters in solution and form stable, irreversible metal nuclei "*seed*" [9, 18]. The difference in the reduction potentials between the metal salt and the reducing agent determines the metal-metal bond strength along with the size to which the initial seed nucleus grows [31, 32]. A strong reducing agent speeds up the rate of reaction and favours the growth of smaller nanoparticles, whereas weak reducing agents lead to a slow reaction favouring larger particles. Stabilizing agents are not only required to prevent agglomeration but also influence the growth process of nanoparticles by interacting with the solute or solvent or even the catalyst [28]. **Table 1.1** lists some of the precursors (metal complexes), reducing agents and stabilizers commonly used.

Table 1.1 *List of precursors, reducing agents and stabilizers commonly used in metal nanoparticle synthesis.*

Precursors	Reducing agents	Stabilizers
Elemental metals	Ammonium ions	Polyethyleneimine
Inorganic salts	Citric acid	Polyvinylalcohol, PVA
Metal complexes	Formaldehyde	Poly(vinylpyrrolidone), PVP
	Hydrogen	Poly(methyl vinyl ether)
	Hydrogen peroxide	Sodium polyacrylate
	Methanol	Sodium polyphosphate
	Sodium citrate	
	Sodium carbonate	
	Sodium hydroxide	

The other method by which metal nanoparticles are synthesized is by the kinetic approach. In this strategy, nanoparticles are fabricated by either confining the process to a limited space or limiting the amount of precursors available for growth. Typically kinetic approaches include aerosol pyrolysis, micelle synthesis, microemulsion, molecular beam epitaxy and template-based deposition [9].

1.1.3 Bimetallic nanoparticles

Multicomponent nanoparticles composed of two different metals are of significance from both the scientific and technological perspectives for improved optical properties and applicability, specifically in catalysis. In fact, in-depth studies of bimetallic catalysts have shown that there is a relationship between the catalytic activity and the particle structure/composition of the catalyst [33]. At the nanoscale, bimetallic nanoparticles offer enhanced physical, optical and catalytic properties over their individual counterparts [34-36]. A number of solution-based approaches for bimetallic nanoparticle synthesis have been reported such as thermal decomposition, co-reduction, microwave, seeded growth, and galvanic replacement [34]. Among the various methods, galvanic replacement is especially desirable as its only requirement is a favourable difference in the reduction potential between two metals. A galvanic replacement reaction involves an oxidation-reduction between a sacrificial metal template and metal ions in solution. The difference in the reduction potential between the two metals drives the oxidation of the metal template and reduction of metal ions to deposit on the surface of the sacrificial metal template [37, 38]. Through this approach, nanoparticle composition, size, morphology, and porosity can be controlled essentially in a single step [26, 27, 39, 40]. Further, the electroless nature of this method provides a significant advantage in terms of ease of the reaction. By controlling the reaction parameters during galvanic replacement, one can influence the nature of nanostructures that are eventually formed [35]. Conditions such as template morphology [41], reaction medium [42]

and the oxidation state of metal ions [43] can be modulated to obtain the desired nanostructure.

1.1.4 Use of templates for nanoparticle loading

Spontaneous aggregation of nanoparticles poses challenges specifically for its biological applications as the high salt content in biological media induces nanoparticle aggregation. Therefore, their stabilisation becomes crucial especially to maintain their catalytic activity. Studies have shown that the nanoparticles anchored on specific supports prevent aggregation and thereby preserve catalytic activity [44]. A wide range of substrates have been explored in this area including thin films, polymers, and foils [26]. In particular paper, textiles and diatom frustules have been widely used as these templates show a fibre network-like structure [21, 34, 45-48]. The potential of using textiles as substrates for fabricating nanomaterials is interesting as the interwoven threads of the cotton textiles provide a 3-dimensional (3D) matrix for assemblies of nanoparticles. Textiles have come to be used in this technique owing to their well-established manufacturing processes that allow for facile integration of new functionalities with economic viability. Textiles are versatile materials providing flexibility, absorbency, porosity, and wettability along with a large surface area thereby being a robust template for loading of nanostructured materials [46, 47, 49-51]. In fact, nanoparticle loaded fabrics or commonly termed as functional fabrics have been used in catalysis [21, 34], sensing [51, 52], optoelectronics [49, 51], self-cleaning [53], and antimicrobial applications [54, 55].

Current strategies for creating metal and metal oxide nanostructures on fabrics involve sputtering, sol-gel, sonochemical methods or a layer by layer process. All of these techniques possess inherent challenges as these materials tend to detach from the surface of the fabric during its applicability [49, 51]. Further, the challenges associated with depositing

nanoparticles post-synthesis on a template can also result in nanoparticle detachment. One strategy to overcome this limitation is to fabricate nanoparticles on the surface of the fabric directly using a facile electroless deposition technique [56]. This strategy involves several reactions occurring simultaneously in aqueous media without the use of any external potential [57, 58]. Through this method, uniform deposition of several metals has been achieved including silver, gold, aluminium, copper, nickel and iron [56]. Through previous studies, it has been recognised that nanostructures of copper exhibit high catalytic ability [21]. Given that copper is relatively cheap in comparison to gold, and additionally it possesses SPR in the visible range [59], the current work focuses primarily on copper.

Copper nanoparticles were synthesized on the cotton fabrics by an electroless deposition method [56, 57, 60]. Electroless deposition is a method of metallization involving galvanic displacement reaction, where the deposition takes place in the presence of reducing agents and a disproportionation reaction [60]. The reducing agent must have a higher redox potential than copper in order for this reaction to be thermodynamically favourable. Deposition begins by a method of substrate catalysation referring to a seed layer deposition which is catalytically capable of invoking the initial anodic oxidation of the reductant [61]. This layer is developed by sensitising the substrate in a solution of tin and palladium resulting in a surface of high-density catalytic sites available for metallization [62, 63]. In a two-step seeding process, a non-catalytic surface of the cotton fabric is treated by immersion in an acidic solution of $SnCl_2$; following by $Pd(NO_3)_2$ [64]. The reaction is represented in **Equation 1.1** and **Equation 1.2**.

$$Sn^{2+} \rightleftharpoons Sn^{4+} + 2e^- \qquad E^0 = -0.151 \qquad (\textit{Equation 1.1})$$

$$Pd^{2+} + 2e^- \rightleftharpoons Pd^0 \qquad E^0 = +0.951 \qquad (\textit{Equation 1.2})$$

The reduced Pd acts as catalytic sites for the oxidation of the reducing agent *i.e.*, formaldehyde and thereby the subsequent electroless deposition of copper (**Equation 1.3** and **Equation 1.4**) [58]. Studies have shown that the splitting of C-H bond in the methylene glycolate anion during the formaldehyde oxidation results in the formation of atomic hydrogen. The hydrogen ad-atoms further combine to form hydrogen gas which can also contribute as a supplementary reducing agent [61, 65].

$$HCHO + H_2O \rightarrow HCOOH + 2H^+ + 2e^- \qquad E^0 = +0.056 \quad (\textit{Equation 1.3})$$

$$Cu^{2+} + 2e^- \rightleftharpoons Cu^0 \qquad E^0 = +0.342 \quad (\textit{Equation 1.4})$$

Formaldehyde oxidation generates hydrogen (H^+) and hydroxyl ions (OH^-) which lower the pH of the reaction system which has a significant effect on the deposition rate and properties of the deposited metal. A change in the pH can also cause metal precipitation in solution. However, copper deposition is thermodynamically favourable in alkaline conditions. Therefore, in order to sustain a deposition reaction at high pH, complexants are added. Complexants such as ethylenediaminetetraacetic acid (EDTA), triethanolamine, sodium potassium tartrate (Rochelle salt), Glycolic acid, *etc*., are commonly used in copper deposition systems to maintain the concentration of free metal ions at a level that is defined by the dissociation constant of the metal complex. This allows the deposition to occur at higher alkaline pH [56]. In some instances, buffers such as carboxylic acids are used for pH stabilization. Instability of deposition systems due to the presence of active nuclei in the form of metallic or dust particles is overcome by using stabilizers in small concentrations. The commonly used stabilizers include oxygen, 2-mercaptobenzo-thiazole, thiourea, vanadium pentoxide, and diethyldithio-carbamate. Exaltants such as O-phenanthroline, propionitrile, and cyanide also accelerate the rate of deposition which might sometimes be lowered by complexants.

1.2 Applications of Nanotechnology

Given the unique properties of nanoparticles, it is not surprising to see their widespread use to improve existing technologies or create new technologies in fields of pathogen, pesticide and other small molecule detection, antimicrobial, self-cleaning and superhydrophobic textiles (smart textiles), targeted drug delivery and nanomedicine, alterable light-transmission glass (smart glass) and self-cleaning glass, chemistry, heavy industries, environment and agriculture [66-73]. In the current work, the catalytic activity of nanoparticles is used in biosensing applications as detailed in the following sections.

Figure 1.2 *Applications of nanotechnology.*

1.2.1 Biosensors

Biosensors are analytical devices that combine the sensitivity and specificity of biological systems with the computational and logical competencies of a microprocessor [74]. Biosensors typically measure biochemical reactions by producing signals that are proportional to the concentration of the test analyte. A biosensor is comprised of a bioreceptor, transducer, and electronics (**Figure 1.3**) [75]. The bioreceptor is the molecular recognition element (MRE) that interacts with the analyte of interest and produces an effect that is measurable by the transducer [76]. MRE's are either naturally available biomolecules or receptors modelled after biological systems such as antigen/antibody, proteins/enzymes/, nucleic acid/aptamers, cells/cellular structures, ligands, microorganisms, and biomimetic

materials. The key to selecting a bioreceptor is that it needs to be highly specific to the target analyte as the target is typically present in a complex matrix of other chemical and biological components [77]. Depending on the type of transducer used, the biochemical signal from an analyte-bioreceptor interaction is converted to an optical, electronic, electrochemical, pyroelectric, piezoelectric or gravimetric signal [78]. This signal is then amplified, processed and displayed by the electronic system.

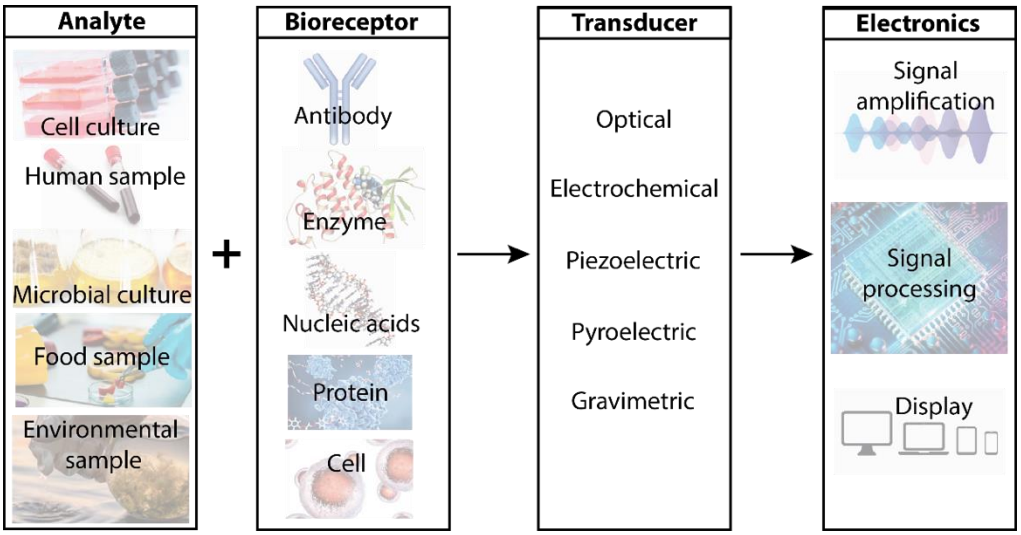

Figure 1.3 *Schematic of a typical biosensor.*

Of the different transducers, optical transducers have gained significant attention as these sensors provide a visual representation of the sensing event. This ability can, in principle, be beneficial for the translation of such sensors for point-of-care devices. The development of highly sensitive optical transducers has led to the use of optical biosensors in a variety of applications such as clinical diagnosis, drug design, food industry, environmental control and biomolecular engineering. Widely used optical biosensors are based on surface plasmon resonance (SPR) changes [79]. Optical nano-biosensors can be devised by incorporating nanostructures of gold and silver nanomaterials exhibiting rich optical properties [59]. This phenomenon is a result of their localized surface plasmon resonance (LSPR). LSPR is an optical phenomenon caused by the resonant oscillation of conduction

electrons in metal nanostructures surrounded by a dielectric when stimulated by incident light [80]. Absorption and scattering of light by metal nanostructures is enhanced when the LSPR is excited. Highly confined and intense electromagnetic fields induced by LSPR provide a highly sensitive probe for the detection of small changes in the dielectric environment around the nanomaterial. This is a particularly attractive feature for sensing applications [81]. The origin of LSPR changes differentiates the sensors into two categories: aggregation sensors and refractive index sensors. Aggregation sensors are based on the change in color induced by nanoparticle aggregation as a result of biochemical interaction between complementary molecules functionalised on the metal nanoparticles. Refractive index sensors are based on the red-shift of the LSPR brought about by an increase in the refractive index around the metal nanostructures [82]. Although such sensors have shown significant potential one major limitation of such sensors is that when these nanoparticles come in contact with biological media, the high salt content typically results in nanoparticle aggregation. This can lead to change in the color of the senor leading to false positives [70]. Therefore, there has been a significant push to explore new systems using nanoparticles for sensing applications [59].

1.2.2 Catalysts

Catalysts are inorganic molecules that lower the activation energy of thermodynamically unfavourable reactions and thereby accelerate the rate of a chemical reaction while remaining unused in the reaction [83]. Catalysis reactions are categorized into homogenous catalysis and heterogeneous catalysis reactions based on the phase of the catalyst with respect to the phase of the reactants [84-86]. In homogenous catalysis, the catalyst and reactants are in the same phase. However, recovery of nanocatalysts post-reaction has proved to be difficult; thereby limiting their applicability [45]. On the other hand, heterogeneous catalysis involves a catalyst in a phase different from that of the reactants. Heterogeneous catalysts are typically nanocatalyst adsorbed on a support allowing for easy separation from the reaction mixture

[26, 27, 87]. Nanostructures that are created on templates such as paper, textiles or diatom frustules exhibit hierarchical structuring at the nanoscale thereby enhancing access to the number of catalytic sites [21, 34, 45-48].

A subset of catalysts is enzymes – organic molecules that catalyse biological reactions responsible for biological metabolism and regulation [88, 89]. Distinct functional groups in their catalytic active site provide high substrate specificity and selectivity. However, due to their organic origins, enzymatic activity is often influenced by pH, enzyme-specific substrate concentration, temperature, *etc*., [90]. Extreme conditions can, in fact, lead to denaturing the enzymes by breaking bonds, which change the 3D orientation and thereby affect the enzymatic activity. Additionally, the high cost involved in the synthesis, purification and storage conditions of natural enzymes restricts their use [91]. To overcome these drawbacks, artificially synthesized materials that mimic the catalytic activity of enzymes are being explored. Ronald Breslow coined the term Artificial Enzymes for the branch of biomimetic chemistry that involves the imitation of natural enzymes using alternative materials [92]. Cyclodextrins, antibodies, hematin, hemin, porphyrins, metal complexes, nanoparticles, DNAzymes, and RNAzymes have all been studied to either imitate natural enzyme-like activity or to replicate the elusive structure of an enzyme active site [72]. Among them, nanomaterials have shown significant promise and are discussed in detail in the following section.

1.3 NanoZymes

The enzyme-mimicking activity of nanomaterials was initially reported in fullerene-based nanomaterials [93], ferromagnetic nanoparticles [94], and gold nanoparticles [95]. These nanomaterials were named based on the enzyme they mimicked. Later, the term *NanoZymes* for nanomaterials exhibiting enzyme-mimicking activity was coined by Scrimin, Pasquato,

and co-workers [96]. Since then, there has been an explosion in research to identify different metal, metal oxide, carbon-based and other nanomaterials for their enzyme-mimic activity [72, 73].

Despite the fact that enzymes are biomolecules with a size and shape different from the crystal structure of a nanomaterial, they share similarities in terms of size, morphology, and surface charge that might be responsible for the inherent enzyme-mimic catalytic activity [97]. Controllable size, shape, and composition, structure-dependent properties, large surface area with the possibility for bioconjugation and other modifications, self-assembling capabilities, tunable response to stimuli, storage stability, and cost-effectiveness make nanomaterials an interesting choice for enzyme alternatives [72, 98, 99].

1.3.1 Types of NanoZymes

Widely reported enzyme-mimic activities of nanomaterials are peroxidase, oxidase, superoxide dismutase, catalase, and hydrolase (**Figure 1.4**) [52, 70, 72, 73, 100-106]. Multi-enzyme-mimicking NanoZymes that exhibit two or more enzyme-mimic properties have been developed [107-111].

Oxidase enzymes are a class of oxidoreductase enzymes that catalyses the oxidation of a substrate to H_2O or H_2O_2 where molecular oxygen is the electron acceptor. The reaction can be represented by **Equation 1.5** and **Equation 1.6**.

$$O_2 + 2AH \xrightarrow{\text{oxidase}} H_2O + 2A \qquad \textit{Equation 1.5}$$

$$O_2 + 2AH \xrightarrow{\text{oxidase}} H_2O_2 + 2A \qquad \textit{Equation 1.6}$$

NanoZymes that exhibit oxidase-mimic activity generates a chromogenic or fluorogenic product depending on the substrate. For example, 3,3’,5,5’ tetramethylbenzidine

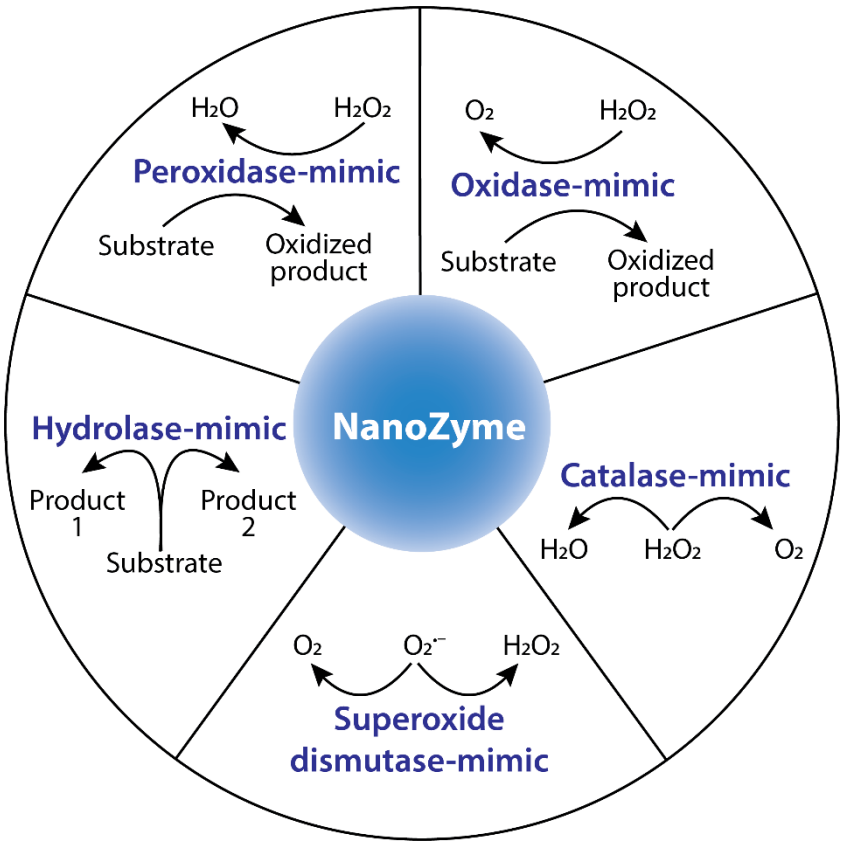

Figure 1.4 *Most commonly reported types of NanoZymes.*

(TMB) and 2,2'-azino-bis(3-ethylbenzothiazoline-6-sulfonic acid) (ABTS) generate a chromogenic response while Amplex red results in the formation of fluorescent resorufin. A wide range of NanoZymes have been studied to mimic oxidase activity including catechol oxidase, cytochrome *c* oxidase, ferroxidase, glucose oxidase, laccase, sulphite oxidase, *etc*., [73, 112].

Superoxide dismutase (SOD) enzymes eliminate superoxide anion $O_2{\cdot}^-$ by catalysing the dismutation of $O_2{\cdot}^-$ into either molecular oxygen or hydrogen peroxide (**Equation 1.7**). Superoxide radicals can cause oxidative damage if left unregulated [113]. SOD enzyme works along with catalase enzyme to effectively protect aerobic organisms from ROS-mediated oxidative stress.

$$2O_2{\cdot}^- + 2H^+ \xrightarrow{\text{SOD}} H_2O_2 + O_2 \qquad \textit{Equation 1.7}$$

Nanomaterials displaying SOD-mimicking activity were found to not only eliminate $O_2^{\cdot -}$ but also other free radicals. This property of NanoZymes is significant as it strengthens the protection of biological systems from ROS related injury [73, 110, 114].

Catalase enzymes catalyse the decomposition of H_2O_2 into water and oxygen gas (**Equation 1.8**) [115]. Hydrogen peroxide is typically generated from superoxide radicals' dismutation reaction in biological systems. Catalases prevent the possible conversion of stable H_2O_2 into highly reactive oxygen species [116].

$$2H_2O_2 \xrightarrow{\text{catalase}} 2H_2O + O_2 \qquad \textit{Equation 1.8}$$

Hydrolase enzyme catalyses the hydrolysis of a chemical bond resulting in the breakdown of a large molecule into smaller molecules (**Equation 1.9**) [117, 118]. Their degradative properties are responsible for the breakdown of fats, lipoproteins, and other large molecules.

$$AB + H_2O \xrightarrow{\text{hydrolase}} AOH + BH \qquad \textit{Equation 1.9}$$

Hydrolase-mimicking nanomaterials are of significance for environmental cleanup [53, 119, 120]. NanoZymes have been explored to mimic different hydrolase enzymes such as protease, carbonate ester-hydrolase, nuclease, phosphodiesterase, *etc*., [73].

Peroxidase enzymes are a class of oxidoreductase enzymes that catalyse the oxidation of a substrate in the presence of a peroxide, most commonly hydrogen peroxide (**Equation 1.10**). H_2O_2 is generated by cellular metabolism in an effort to eliminate more dangerous reactive oxygen species like superoxide. Peroxidase enzymes not only serve as detoxifying agents that prevent inflammatory diseases [121] but also build up a defence against infectious pathogens by producing hypohalous acids as in the case of myeloperoxidase [122].

$$2AH + H_2O_2 \xrightarrow{\text{peroxidase}} 2A + 2H_2O \qquad \textit{Equation 1.10}$$

Horseradish peroxidase (HRP) is a widely used peroxidase enzyme in clinical and bioanalytical applications. It is used as a detection reagent in immunohistochemistry, western blot, ELISA and other immunoassays. The activity of this enzyme is measured by the color, fluorescence or luminescence generated by the respective substrate by spectrophotometric methods. Chromogenic substrates for HRP include TMB, ABTS, *o*-Phenylenediamine (OPD), 3,3'-Diaminobenzidine (DAB), *etc*., Amplex red and luminol are the fluorogenic and chemiluminescent substrates, respectively [123].

The first reported enzyme-mimic activity of a nanomaterial was the peroxidase-mimicking activity of Fe_3O_4 [94]. Following which, a wide range of nanoparticles including iron, noble metals, vanadium, carbon, and metal-organic framework-based nanomaterials with peroxidase-mimic activity have been developed and used in a wide variety of applications such as biomolecule sensing [52, 70, 101-104], therapeutics [124], imaging [125, 126], antibacterial [100, 127], cancer therapy [105], anti-biofouling [128], wastewater treatment [94], *etc*.,

1.3.2 Application of NanoZymes in biosensing

As an alternative strategy to overcome the low sensor specificity of LSPR based optical nano-biosensors, enzyme-based biosensors have come to be used extensively for their sensitivity and selectivity towards the target. Their specific binding capabilities and catalytic activity contribute to analyte detection either (i) by the enzymatic conversion of the analyte to sensor-detectable products, (ii) by analyte induced enzyme activation or inhibition, or (iii) by changes in enzymatic properties as a result of enzyme-analyte interaction [129]. Such biosensors can be used continuously as the enzyme is not consumed in the reaction. However, the stability of enzymes limits the sensor's lifetime [130]. This is one of the primary reason

for the incorporation of NanoZymes in biosensors for a wide variety of biotechnological and biomedical applications such as diagnostic medicine, targeted drug delivery, analyte detection in food and health industry [98, 112]. Apart from electrochemical, fluorescent and chemiluminescent biosensing approaches, NanoZymes involved in colorimetric approaches have been fabricated and utilized for an easy, fast, selective, and cost-effective biosensing [131]. Colorimetric biosensors involve a simple UV-visible spectroscopic measurement or even naked-eye detection. The lack of any advanced instruments makes this biosensing approach easy to convert to a point-of-care format. The colorimetric NanoZyme based biosensing approach has been successfully used to detect biomolecules [36, 52, 102, 105, 132, 133], pesticides [70, 101, 103], virus [104], metal ions [134] *etc*.,

Among the various biomolecules, detection of glucose is of significance in clinical diagnostics, food analysis and research [78, 135]. An abnormal level of glucose in the blood is the primary symptom of *Diabetes mellitus* [136]. Regular monitoring of glucose levels in the body is the key to diabetes management. In Type I diabetic condition, renal complications arise such as renal glycosuria and Fanconi syndrome where glucose is eliminated in the urine. Therefore it is essential to develop analytical tools to monitor urine glucose levels.

Glucose biosensing is realized in a two-step process (**Figure 1.5**). First, glucose oxidase catalyses glucose oxidation to D-glucono-1,5-lactone and hydrogen peroxide in the presence of molecular oxygen. In the second step, the horseradish peroxidase (HRP) enzyme catalyses the reduction of while simultaneously oxidising a substrate. Typically, the oxidised substrate generates a measurable colorimetric signal. Glucose oxidase is a stable enzyme that is catalytically active at 37 °C in slightly acidic pH [137]. However, HRP can be easily inactivated by its substrate H_2O_2 [90]. Hence new strategies to replace HRP have come about including the use of peroxidase-mimicking NanoZymes.

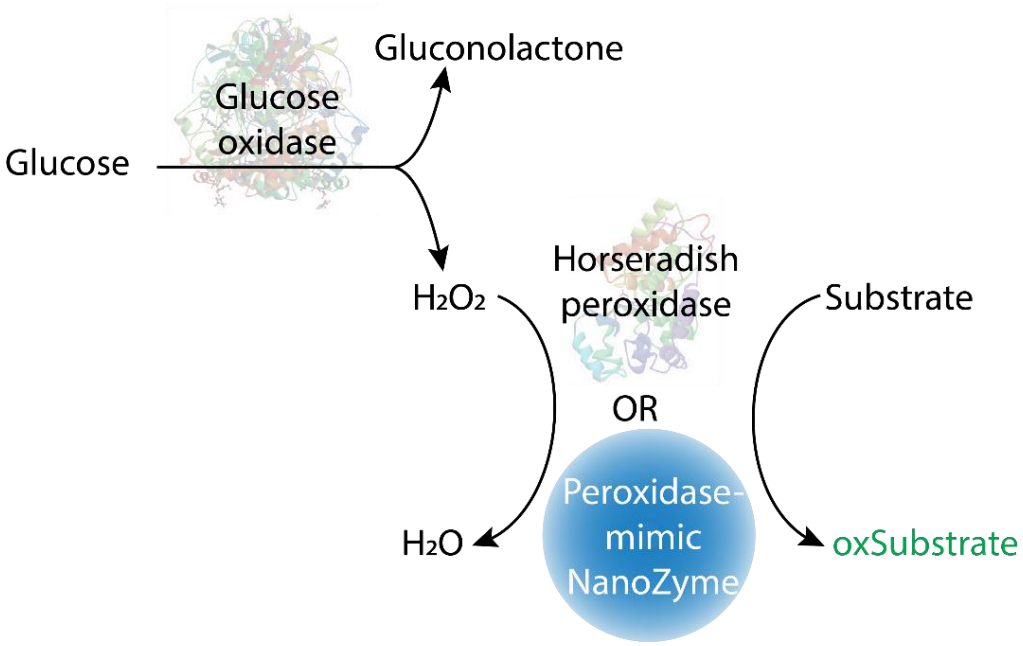

Figure 1.5 *Scheme depicting the mechanism of colorimetric glucose detection.*

This approach was used by Wei and Wang to detect glucose using peroxidase-mimicking magnetic Fe_3O_4 nanoparticles. The nanoparticles were found to be capable of detecting glucose in the range of 50 µM to 1 mM concentration. The system was also specific to glucose in the presence of interfering analogous of glucose such as fructose, lactose, and maltose [138]. The practical applicability of NanoZyme-based sensing systems have been demonstrated to detect glucose in a wide variety of real samples such as clinical samples of blood, urine, sweat and food samples including fruit juices. Specifically, a few examples of peroxidase-mimicking NanoZymes used for glucose sensing are summarised in **Table 1.2**.

Table 1.2 *Peroxidase-mimicking NanoZymes used for colorimetric glucose sensing.*

NanoZymes	Linear range (mM)	Sample type	Ref.
C-dots	0.001 – 0.5	Serum	[139]
g-C_3N_4	0.005 – 0.1	Serum	[140]
g-C_3N_4 nanosheets	0.0005 – 0.01	Serum	[141]
C_{60}-carboxyfullerenes	0.001 – 0.04	Serum	[142]
N-G quantum dots	0.025 – 0.375	Fruit juice and serum	[143]
Ag@fabric	0.1 – 2	Urine	[52]
Ch-Ag nanoparticles	0.005 – 0.2	Serum	[144]
Au@Ag nanorods	0.05 – 20	Fruit juice and serum	[145]
Au@Pt nanorods	0.045 – 0.4	N.R.	[146]
Au nanoparticles	0.001 – 0.04	Serum	[147]
CeO_2 nanoparticles	0.0066 – 0.13	Serum	[148]
CoFe nanoplates	0.001 – 0.01	Serum	[149]
CuO nanoparticles	0.1 – 8	N.R.	[150]
Cu nanoclusters	0.1 – 2	N.R.	[151]
Cu nanoparticles	0.001 – 0.1	Fruit juice and serum	[152]
Cu-Ag NPs/rGO NPs	0.001 – 0.03	Serum	[36]
GO-Fe_3O_4 nanocomposites	0.002 – 0.2	Urine	[153]
Fe_3O_4 G-nanocomposites	0.005 – 0.5	Serum	[154]
Fe_3O_4 nanoparticles	0.05 – 1	N.R.	[138]
Fe_3O_4-Pd nanohybrids	0.0005 – 0.06	Urine	[155]
MFe_2O_4 (M=Mg, Ni, Cu) NPs	0.00094 – 0.025	Urine	[156]
NiFe nanosheets	0.05 – 2	Fruit juice	[157]
NiO nanoparticles	0.05 – 0.5	Serum	[158]
NiPd nanoparticles	0.005 – 0.5	Urine	[159]
Pt nanoclusters	0 – 0.2	Serum	[160]
Pt-DNA complexes	0.0001 – 1	Fruit juice	[161]
Rh nanoparticles	0.005 – 0.125	Fruit juice and serum	[162]
$ZnFe_2O_4$ nanoparticles	0.00125 – 0.01875	Urine	[163]

N.R.: Not reported

1.4 Motivation

The increased occurrence of *Diabetes mellitus* has bought significant attention towards the development of glucose sensors. Blood glucose monitors have been quite successful commercially [164]. However, invasive methods of sample collection can be quite painful especially in the cases of high-level diabetes and juvenile diabetes where multiple testings are required in a single day. Long term effects of diabetes also lead to renal complications where glucose elimination occurs through urine. Therefore, there is a need for urine glucose sensors to not only monitor diabetes but also the health of the kidneys [135]. There have been several reports using colloidal NanoZyme-based sensing systems for urine glucose detection. However, such systems are easily saturated by the high concentrations of glucose in urine as the linear dynamic range for such sensors are typically in the pM range. One way to shift the dynamic range is to increase the concentration of NanoZyme. However, increasing the NanoZyme load to cope with a larger analyte concentration would affect the sensor response with LSPR or nanoparticle scattering interference. One possible way to overcome this limitation is to load NanoZymes on templates. This will create a system where the reaction can be controlled by either introducing the catalyst or removing the catalyst. Such on-demand catalytic systems are termed as free-standing NanoZyme systems [52]. By incorporating nanoparticles of high catalytic activity, the range of detection could be increased to the biologically relevant concentration. Further, as higher loading of NanoZymes may produce an intense color, it will eliminate the need for advanced instruments makes this colorimetric biosensing approach easy to convert to a point-of-care format.

1.5 Thesis outline

The work presented in this thesis illustrates strategies to improve the detection of glucose by NanoZymes. This was done by first determining the NanoZyme activity of Cu and bimetallic

nanoparticles of Cu, followed by the application of this activity towards biosensing of glucose.

A chapter-wise summary of the thesis is as follows:

Chapter 2 explains the working principle of all the instruments that were used for the characterization of the nanomaterials. The instruments include UV-visible absorption spectroscopy (UV-vis), fluorescence spectroscopy, Atomic Emission Spectroscopy (AES), Scanning Electron Microscopy (SEM), Energy Dispersive X-ray Spectroscopy (EDX), X-ray Diffraction (XRD), and X-ray Photoelectron Spectroscopy (XPS).

Chapter 3 explains a simple strategy for the synthesis of copper nanoparticles on the 3D matrix of a cotton textile (Cu@Fabric). The ability of the free-standing peroxidase-mimicking NanoZyme to detect glucose in urine in the biologically relevant range is then shown. The use of a template such as cotton fabric increases the NanoZyme load that participates in the reaction. The peroxidase-mimicking activity of the Cu@Fabric was evaluated using a peroxidase substrate – TMB. The performance of the Cu@Fabric NanoZyme as glucose sensor was assessed in terms of glucose detection range, limit of detection (LoD), specificity, accuracy, and precision. The practical feasibility of the sensor was validated for glucose detection in human urine samples and compared with the results obtained from laboratory gold standard (glucose oxidase-horseradish peroxidase) and commercial urine glucose test strips.

Chapter 4 describes the fabrication of bimetallic nanoparticles on the 3D matrix of cotton fabric (CuAg@Fabric, CuAu@Fabric, CuPt@Fabric, and CuPd@Fabric) using a simple method of galvanic replacement. These systems were evaluated for enhancement or decrement in their intrinsic peroxidase-mimicking catalytic activity in comparison to the Cu@Fabric. Further, the NanoZyme system with the highest catalytic activity – Cu-

Pt@Fabric – was chosen to develop a glucose-sensing system that can detect glucose in undiluted samples of urine. The colorimetric response of the system to glucose and the catalyst stability were evaluated against the Cu@Fabric NanoZyme system.

Chapter 5 summarises the significant outcomes of both the research projects worked on in this thesis. The potential for further work in this area is also provided.

1.6 References

1. Feynman, R.P., There's plenty of room at the bottom, in *Annual Physical Society*. 1960: California Institute of Technology, Engineering and Science magazine.
2. Drexler, K.E., *Engines of creation*. 1990: Anchor.
3. Taniguchi, N., C. Arakawa, and T. Kobayashi. On the basic concept of'nano-technology'. in *Proc. Int. Conf. Prod. Eng.* 1974.
4. Berger, M., *Nano-society: pushing the boundaries of technology*. Vol. 8. 2009: Royal Society of Chemistry.
5. Sanchez, F. and K. Sobolev, *Constr. Build. Mater.*, 2010. **24**(11): 2060-2071.
6. Murty, B., P. Shankar, B. Raj, B. Rath, and J. Murday, *Textbook of nanoscience and nanotechnology*. 2013: Springer Science & Business Media.
7. Poole Jr, C.P. and F.J. Owens, *Introduction to nanotechnology*. 2003: John Wiley & Sons.
8. Buzea, C., I.I. Pacheco, and K. Robbie, *Biointerphases*, 2007. **2**(4): MR17-MR71.
9. Guozhong, C., *Nanostructures and nanomaterials: synthesis, properties and applications*. 2004: World scientific.
10. Lopez-Diaz, L., L. Torres, and E. Moro, *Phys. Rev. B: Condens. Matter*, 2002. **65**(22): 224406.
11. Eustis, S. and M.A. El-Sayed, *Chem. Soc. Rev.*, 2006. **35**(3): 209-217.
12. Carnovale, C., G. Bryant, R. Shukla, and V. Bansal, *Prog. Mater. Sci.*, 2016. **83**: 152-190.
13. Ishida, T., N. Kinoshita, H. Okatsu, T. Akita, T. Takei, and M. Haruta, *Angew. Chem. Int. Ed.*, 2008. **47**(48): 9265-9268.
14. Liu, B. and J. Liu, *Nano Res.*, 2017. **10**(4): 1125-1148.
15. Sabri, Y.M., S.J. Ippolito, A.J. Atanacio, V. Bansal, and S.K. Bhargava, *J. Mater. Chem.*, 2012. **22**(40): 21395-21404.
16. Wang, Y. and Y. Xia, *Nano Lett.*, 2004. **4**(10): 2047-2050.
17. Drexler, K.E., *Nanosystems: molecular machinery, manufacturing, and computation*. 1992: Wiley New York.

18. Kumar, N. and S. Kumbhat, 2016.

19. Standardization, I.O.f., Nanotechnologies — Vocabulary — Part 2: Nano-objects. 2015.

20. Chan, G.H., J. Zhao, E.M. Hicks, G.C. Schatz, and R.P. Van Duyne, *Nano Lett.*, 2007. **7**(7): 1947-1952.

21. Anderson, S.R., M. Mohammadtaheri, D. Kumar, A.P. O'Mullane, M.R. Field, R. Ramanathan, and V. Bansal, *Adv. Mater. Interfaces*, 2016. **3**(6): 1500632.

22. Guo, X., C. Hao, G. Jin, H.Y. Zhu, and X.Y. Guo, *Angew. Chem. Int. Ed.*, 2014. **53**(7): 1973-1977.

23. Shan, Z., M. Lu, L. Wang, B. MacDonald, J. MacInnis, M. Mkandawire, X. Zhang, and K.D. Oakes, *Chem. Commun.*, 2016. **52**(10): 2087-2090.

24. Ruparelia, J.P., A.K. Chatterjee, S.P. Duttagupta, and S. Mukherji, *Acta biomater.*, 2008. **4**(3): 707-716.

25. Ren, G., D. Hu, E.W. Cheng, M.A. Vargas-Reus, P. Reip, and R.P. Allaker, *Int. J. Antimicrob. Agents*, 2009. **33**(6): 587-590.

26. Bansal, V., H. Jani, J. Du Plessis, P.J. Coloe, and S.K. Bhargava, *Adv. Mater.*, 2008. **20**(4): 717-723.

27. Bansal, V., A.P. O'Mullane, and S.K. Bhargava, *Electrochem. Commun.*, 2009. **11**(8): 1639-1642.

28. Henglein, A., *Chem. Mater.*, 1998. **10**(1): 444-450.

29. Selvakannan, P., R. Ramanathan, B.J. Plowman, Y.M. Sabri, H.K. Daima, A.P. O'Mullane, V. Bansal, and S.K. Bhargava, *Phys. Chem. Chem. Phys.*, 2013. **15**(31): 12920-12929.

30. Faraday, M., *Philos. Trans. Royal Soc.*, 1857(147): 145-181.

31. Lieser, K., *Angew. Chem. Int. Ed.*, 1969. **8**(3): 188-202.

32. Mer, V.K.L., *Ind. Eng. Chem. Res.*, 1952. **44**(6): 1270-1277.

33. Toshima, N. and T. Yonezawa, *New J. Chem.*, 1998. **22**(11): 1179-1201.

34. Anderson, S.R., A.P. O'Mullane, E. Della Gaspera, R. Ramanathan, and V. Bansal, *Adv. Mater. Interfaces*, 2019. **6**(16): 1900516.

35. Pearson, A., A.P. O'Mullane, S.K. Bhargava, and V. Bansal, *Inorg. Chem.*, 2012. **51**(16): 8791-8801.

36. Darabdhara, G., B. Sharma, M.R. Das, R. Boukherroub, and S. Szunerits, *Sens. Actuators, B*, 2017. **238**: 842-851.

37. Xia, X., Y. Wang, A. Ruditskiy, and Y. Xia, *Adv. Mater.*, 2013. **25**(44): 6313-6333.

38. da Silva, A.G., T.S. Rodrigues, S.J. Haigh, and P.H. Camargo, *Chem. Commun.*, 2017. **53**(53): 7135-7148.

39. Skrabalak, S.E., J. Chen, Y. Sun, X. Lu, L. Au, C.M. Cobley, and Y. Xia, *Acc. Chem. Res.*, 2008. **41**(12): 1587-1595.

40. Pearson, A., A.P. O'Mullane, V. Bansal, and S.K. Bhargava, *Chem. Commun.*, 2010. **46**(5): 731-733.

41. Zhang, Q., W. Wang, J. Goebl, and Y. Yin, *Nano Today*, 2009. **4**(6): 494-507.

42. Lu, X., H.-Y. Tuan, J. Chen, Z.-Y. Li, B.A. Korgel, and Y. Xia, *J. Am. Chem. Soc.*, 2007. **129**(6): 1733-1742.

43. Zhao, L., K. Ding, X. Ji, J. Li, H. Wang, and W. Yang, *Colloids Surf. A.*, 2011. **386**(1-3): 172-178.

44. Zhu, Q.-L. and Q. Xu, *Chem*, 2016. **1**(2): 220-245.

45. Polavarapu, L. and L.M. Liz-Marzán, *Phys. Chem. Chem. Phys.*, 2013. **15**(15): 5288-5300.

46. Hu, L. and Y. Cui, *Energy Environ. Sci.*, 2012. **5**(4): 6423-6435.

47. Hu, L., M. Pasta, F. La Mantia, L. Cui, S. Jeong, H.D. Deshazer, J.W. Choi, S.M. Han, and Y. Cui, *Nano Lett.*, 2010. **10**(2): 708-714.

48. Losic, D., J.G. Mitchell, and N.H. Voelcker, *Adv. Mater.*, 2009. **21**(29): 2947-2958.

49. Ramanathan, R., A.E. Kandjani, S. Walia, S. Balendhran, S.K. Bhargava, K. Kalantar-zadeh, and V. Bansal, *RSC Adv.*, 2013. **3**(39): 17654-17658.

50. Li, S., J. Huang, M. Ge, C. Cao, S. Deng, S. Zhang, G. Chen, K. Zhang, S.S. Al-Deyab, and Y. Lai, *Adv. Mater. Interfaces*, 2015. **2**(14): 1500220.

51. Ramanathan, R., S. Walia, A.E. Kandjani, S. Balendran, M. Mohammadtaheri, S.K. Bhargava, K. Kalantar-Zadeh, and V. Bansal, *Langmuir*, 2015. **31**(4): 1581-1587.

52. Karim, M.N., S.R. Anderson, S. Singh, R. Ramanathan, and V. Bansal, *Biosens. Bioelectron.*, 2018. **110**: 8-15.

53. López-Maya, E., C. Montoro, L.M. Rodríguez-Albelo, S.D. Aznar Cervantes, A.A. Lozano-Pérez, J.L. Cenís, E. Barea, and J.A. Navarro, *Angew. Chem. Int. Ed.*, 2015. **54**(23): 6790-6794.

54. Davoudi, Z.M., A.E. Kandjani, A.I. Bhatt, I.L. Kyratzis, A.P. O'Mullane, and V. Bansal, *Adv. Funct. Mater.*, 2014. **24**(8): 1047-1053.

55. Falletta, E., M. Bonini, E. Fratini, A. Lo Nostro, G. Pesavento, A. Becheri, P. Lo Nostro, P. Canton, and P. Baglioni, *J. Phys. Chem. C*, 2008. **112**(31): 11758-11766.

56. Mallory, G.O. and J.B. Hajdu, *Electroless plating: fundamentals and applications*. 1990: William Andrew.

57. Mak, C.Y., *MRS Bulletin*, 2013. **19**(8): 55-62.

58. Bindra, P. and J. Roldan, *J. Electrochem. Soc.*, 1985. **132**(11): 2581-2589.

59. Sepúlveda, B., P.C. Angelomé, L.M. Lechuga, and L.M. Liz-Marzán, *Nano Today*, 2009. **4**(3): 244-251.

60. Lahiri, A., G. Pulletikurthi, and F. Endres, *Front. Chem.*, 2019. **7**.

61. Ohno, I., O. Wakabayashi, and S. Haruyama, *J. Electrochem. Soc.*, 1985. **132**(10): 2323-2330.

62. Osaka, T., H. Takematsu, and K. Nihei, *J. Electrochem. Soc.*, 1980. **127**(5): 1021-1029.

63. Vanysek, P., *CRC handbook of chemistry and physics*, 2000. **8**.

64. Feldstein, N. and J. Weiner, *J. Electrochem. Soc.*, 1973. **120**(4): 475-479.

65. Okinaka, Y. and S. Nakahara, *J. Electrochem. Soc.*, 1976. **123**(4): 475-478.

66. Koo, O.M., I. Rubinstein, and H. Onyuksel, *Nanomed-Nanotechnol.*, 2005. **1**(3): 193-212.

67. Brown, P. and K. Stevens, *Nanofibers and nanotechnology in textiles*. 2007: Elsevier.

68. Bhattacharya, S., J. Jang, L. Yang, D. Akin, and R. Bashir, *J. Rapid Methods Autom. Microbiol.*, 2007. **15**(1): 1-32.

69. Durán, N. and P.D. Marcato, *Int. J. Food Sci. Technol.*, 2013. **48**(6): 1127-1134.

70. Weerathunge, P., T.K. Sharma, R. Ramanathan, and V. Bansal, *CHAPTER 23 Nanozyme-Based Environmental Monitoring*, in *Advanced Environmental Analysis: Applications of Nanomaterials, Volume 2*. 2017, The Royal Society of Chemistry. 108-132.

71. Akinwande, D., N. Petrone, and J. Hone, *Nat. Commun.*, 2014. **5**: 5678.

72. Wei, H. and E. Wang, *Chem. Soc. Rev.*, 2013. **42**(14): 6060-6093.

73. Wu, J., X. Wang, Q. Wang, Z. Lou, S. Li, Y. Zhu, L. Qin, and H. Wei, *Chem. Soc. Rev.*, 2019. **48**(4): 1004-1076.

74. Turner, A., I. Karube, and G.S. Wilson, *Biosensors: fundamentals and applications*. 1987: Oxford university press.

75. Turner, A.P.F., *Chem. Soc. Rev.*, 2013. **42**(8): 3184-3196.

76. Hierlemann, A., O. Brand, C. Hagleitner, and H. Baltes. Microfabrication techniques for chemical/biosensors. in *Proc. IEEE*. 2003.

77. Vo-Dinh, T. and B. Cullum, *Anal. Bioanal. Chem.*, 2000. **366**(6-7): 540-551.

78. Wang, J., *Chem. Rev.*, 2008. **108**(2): 814-825.

79. Homola, J., *Chem. Rev.*, 2008. **108**(2): 462-493.

80. Bohren, C.F. and D.R. Huffman, *Absorption and scattering of light by small particles*. 2008: John Wiley & Sons.

81. Gunnarsson, L., T. Rindzevicius, J. Prikulis, B. Kasemo, M. Käll, S. Zou, and G.C. Schatz, *J. Phys. Chem. B*, 2005. **109**(3): 1079-1087.

82. Liz-Marzán, L.M., *Langmuir*, 2006. **22**(1): 32-41.

83. Singh, S.B. and P.K. Tandon, *J. Energy Chem. Eng.*, 2014. **2**(3): 106-115.

84. Cole-Hamilton, D.J., *Science*, 2003. **299**(5613): 1702-1706.

85. Oyama, S.T. and G.A. Somorjai, *J. Chem. Educ.*, 1988. **65**(9): 765.

86. Philippot, K. and P. Serp, *Concepts in nanocatalysis*, in *Nanomaterials in Catalysis*. 2013. 1-54.

87. Zheng, G., L. Polavarapu, L.M. Liz-Marzán, I. Pastoriza-Santos, and J. Pérez-Juste, *Chem. Commun.*, 2015. **51**(22): 4572-4575.

88. De, M., P.S. Ghosh, and V.M. Rotello, *Adv. Mater.*, 2008. **20**(22): 4225-4241.

89. Chen, M., G. Zeng, P. Xu, C. Lai, and L. Tang, *Trends Biochem. Sci*, 2017. **42**(11): 914-930.

90. Nicell, J.A. and H. Wright, *Enzyme Microb. Technol.*, 1997. **21**(4): 302-310.

91. Valderrama, B., M. Ayala, and R. Vazquez-Duhalt, *Chem. Biol.*, 2002. **9**(5): 555-565.

92. Breslow, R. and L.E. Overman, *J. Am. Chem. Soc.*, 1970. **92**(4): 1075-1077.

93. Ali, S.S., J.I. Hardt, K.L. Quick, J.S. Kim-Han, B.F. Erlanger, T.-t. Huang, C.J. Epstein, and L.L. Dugan, *Free Radic. Biol. Med.*, 2004. **37**(8): 1191-1202.

94. Gao, L., J. Zhuang, L. Nie, J. Zhang, Y. Zhang, N. Gu, T. Wang, J. Feng, D. Yang, and S. Perrett, *Nat. Nanotechnol.*, 2007. **2**(9): 577.

95. Pasquato, L., F. Rancan, P. Scrimin, F. Mancin, and C. Frigeri, *Chem. Commun.*, 2000(22): 2253-2254.

96. Manea, F., F.B. Houillon, L. Pasquato, and P. Scrimin, *Angew. Chem.*, 2004. **116**(45): 6291-6295.

97. Kotov, N.A., *Science*, 2010. **330**(6001): 188.

98. Wang, Q., H. Wei, Z. Zhang, E. Wang, and S. Dong, *TrAC, Trends Anal. Chem.*, 2018. **105**: 218-224.

99. Zhou, Y., B. Liu, R. Yang, and J. Liu, *Bioconjugate Chem.*, 2017. **28**(12): 2903-2909.

100. Karim, M.N., M. Singh, P. Weerathunge, P. Bian, R. Zheng, C. Dekiwadia, T. Ahmed, S. Walia, E. Della Gaspera, S. Singh, R. Ramanathan, and V. Bansal, *ACS Appl. Nano Mater.*, 2018. **1**(4): 1694-1704.

101. Kumar Sharma, T., R. Ramanathan, P. Weerathunge, M. Mohammadtaheri, H. Kumar Daima, R. Shukla, and V. Bansal, *Chem. Commun.*, 2014. **50**(100): 15856-15859.

102. Singh, M., P. Weerathunge, P.D. Liyanage, E. Mayes, R. Ramanathan, and V. Bansal, *Langmuir*, 2017. **33**(38): 10006-10015.

103. Weerathunge, P., R. Ramanathan, R. Shukla, T.K. Sharma, and V. Bansal, *Anal. Chem.*, 2014. **86**(24): 11937-11941.

104. Weerathunge, P., R. Ramanathan, V.A. Torok, K. Hodgson, Y. Xu, R. Goodacre, B.K. Behera, and V. Bansal, *Anal. Chem.*, 2019. **91**(5): 3270-3276.

105. Weerathunge, P., D. Pooja, M. Singh, H. Kulhari, E.L. Mayes, V. Bansal, and R. Ramanathan, *Sens. Actuators, B*, 2019: 126737.

106. Walther, R., A.K. Winther, A.S. Fruergaard, W. van den Akker, L. Sørensen, S.M. Nielsen, M.T. Jarlstad Olesen, Y. Dai, H.S. Jeppesen, P. Lamagni, A. Savateev, S.L. Pedersen, C.K. Frich, C. Vigier-Carrière, N. Lock, M. Singh, V. Bansal, R.L. Meyer, and A.N. Zelikin, *Angew. Chem. Int. Ed.*, 2019. **58**(1): 278-282.

107. Weerathunge, P., B.K. Behera, S. Zihara, M. Singh, S.N. Prasad, S. Hashmi, P.R.D. Mariathomas, V. Bansal, and R. Ramanathan, *Analytica chimica acta*, 2019. **1083**: 157-165.

108. Dong, J., L. Song, J.-J. Yin, W. He, Y. Wu, N. Gu, and Y. Zhang, *ACS Appl. Mater. Interfaces*, 2014. **6**(3): 1959-1970.

109. Lin, Y., Z. Li, Z. Chen, J. Ren, and X. Qu, *Biomaterials*, 2013. **34**(11): 2600-2610.

110. Sun, J., J. Ge, W. Liu, M. Lan, H. Zhang, P. Wang, Y. Wang, and Z. Niu, *Nanoscale*, 2014. **6**(1): 255-262.

111. He, W., Y.-T. Zhou, W.G. Wamer, X. Hu, X. Wu, Z. Zheng, M.D. Boudreau, and J.-J. Yin, *Biomaterials*, 2013. **34**(3): 765-773.

112. Singh, N., M.A. Savanur, S. Srivastava, P. D'Silva, and G. Mugesh, *Angew. Chem. Int. Ed.*, 2017. **56**(45): 14267-14271.

113. Wang, X., Y. Hu, and H. Wei, *Inorg. Chem. Front.*, 2016. **3**(1): 41-60.

114. Hayyan, M., M.A. Hashim, and I.M. AlNashef, *Chem. Rev.*, 2016. **116**(5): 3029-3085.

115. Shen, X., W. Liu, X. Gao, Z. Lu, X. Wu, and X. Gao, *J. Am. Chem. Soc.*, 2015. **137**(50): 15882-15891.

116. Chelikani, P., I. Fita, and P.C. Loewen, *Cell. Mol. Life Sci.*, 2004. **61**(2): 192-208.

117. Gaetani, G.F., A. Ferraris, M. Rolfo, R. Mangerini, S. Arena, and H. Kirkman, *Blood*, 1996. **87**(4): 1595-1599.

118. Savelli, C. and R. Salvio, *Chem.: Eur. J.*, 2015. **21**(15): 5856-5863.

119. Kumar, J.P., G. Prasad, P. Ramacharyulu, P. Garg, and K. Ganesan, *Mater. Chem. Phys.*, 2013. **142**(2-3): 484-490.

120. Liu, Y., S.-Y. Moon, J.T. Hupp, and O.K. Farha, *ACS nano*, 2015. **9**(12): 12358-12364.

121. Janos, P., P. Kuran, M. Kormunda, V. Stengl, T.M. Grygar, M. Dosek, M. Stastny, J. Ederer, V. Pilarova, and L. Vrtoch, *J. Rare Earth.*, 2014. **32**(4): 360-370.

122. Fanjul-Bolado, P., M.B. González-García, and A. Costa-García, *Anal. Bioanal. Chem.*, 2005. **382**(2): 297-302.

123. Hillegass, L., D. Griswold, B. Brickson, and C. Albrightson-Winslow, *J. Pharmacol. Methods*, 1990. **24**(4): 285-295.

124. Veitch, N.C., *Phytochemistry*, 2004. **65**(3): 249-259.

125. Vernekar, A.A., D. Sinha, S. Srivastava, P.U. Paramasivam, P. D'Silva, and G. Mugesh, *Nat. Commun.*, 2014. **5**: 5301.

126. Hu, D., Z. Sheng, S. Fang, Y. Wang, D. Gao, P. Zhang, P. Gong, Y. Ma, and L. Cai, *Theranostics*, 2014. **4**(2): 142.

127. Fan, K., C. Cao, Y. Pan, D. Lu, D. Yang, J. Feng, L. Song, M. Liang, and X. Yan, *Nat. Nanotechnol.*, 2012. **7**(7): 459.

128. Tao, Y., E. Ju, J. Ren, and X. Qu, *Adv. Mater.*, 2015. **27**(6): 1097-1104.

129. Gao, L., K.M. Giglio, J.L. Nelson, H. Sondermann, and A.J. Travis, *Nanoscale*, 2014. **6**(5): 2588-2593.

130. Marazuela, M. and M. Moreno-Bondi, *Anal. Bioanal. Chem.*, 2002. **372**(5-6): 664-682.

131. Rocchitta, G., A. Spanu, S. Babudieri, G. Latte, G. Madeddu, G. Galleri, S. Nuvoli, P. Bagella, M. Demartis, and V. Fiore, *Sensors*, 2016. **16**(6): 780.

132. Nasir, M., M.H. Nawaz, U. Latif, M. Yaqub, A. Hayat, and A. Rahim, *Microchim. Acta*, 2017. **184**(2): 323-342.

133. Hu, L., H. Liao, L. Feng, M. Wang, and W. Fu, *Anal. Chem.*, 2018. **90**(10): 6247-6252.

134. Lu, H.-F., J.-Y. Li, M.-M. Zhang, D. Wu, and Q.-L. Zhang, *Sens. Actuators, B*, 2017. **244**: 77-83.

135. Zohora, N., D. Kumar, M. Yazdani, V.M. Rotello, R. Ramanathan, and V. Bansal, *Colloids Surf. A.*, 2017. **532**: 451-457.

136. Villena Gonzales, W., A.T. Mobashsher, and A. Abbosh, *Sensors*, 2019. **19**(4): 800.

137. Fine, J., *Br. Med. J.*, 1965. **1**(5444): 1209-1214.

138. Weibel, M.K. and H.J. Bright, *J. Biol. Chem*, 1971. **246**(9): 2734-2744.

139. Wei, H. and E. Wang, *Anal. Chem.*, 2008. **80**(6): 2250-2254.

140. Shi, W., Q. Wang, Y. Long, Z. Cheng, S. Chen, H. Zheng, and Y. Huang, *Chem. Commun.*, 2011. **47**(23): 6695-6697.

141. Lin, T., L. Zhong, J. Wang, L. Guo, H. Wu, Q. Guo, F. Fu, and G. Chen, *Biosens. Bioelectron.*, 2014. **59**: 89-93.

142. Tian, J., Q. Liu, A.M. Asiri, A.H. Qusti, A.O. Al-Youbi, and X. Sun, *Nanoscale*, 2013. **5**(23): 11604-11609.

143. Li, R., M. Zhen, M. Guan, D. Chen, G. Zhang, J. Ge, P. Gong, C. Wang, and C. Shu, *Biosens. Bioelectron.*, 2013. **47**: 502-507.

144. Lin, L., X. Song, Y. Chen, M. Rong, T. Zhao, Y. Wang, Y. Jiang, and X. Chen, *Anal. Chim. Acta*, 2015. **869**: 89-95.

145. Jiang, H., Z. Chen, H. Cao, and Y. Huang, *Analyst*, 2012. **137**(23): 5560-5564.

146. Han, L., C. Li, T. Zhang, Q. Lang, and A. Liu, *ACS Appl. Mater. Interfaces*, 2015. **7**(26): 14463-14470.

147. Liu, J., X. Hu, S. Hou, T. Wen, W. Liu, X. Zhu, J.-J. Yin, and X. Wu, *Sens. Actuators, B*, 2012. **166**: 708-714.

148. Li, R., Y. Zhou, L. Zou, S. Li, J. Wang, C. Shu, C. Wang, J. Ge, and L. Ling, *Sens. Actuators, B*, 2017. **245**: 656-664.

149. Jiao, X., H. Song, H. Zhao, W. Bai, L. Zhang, and Y. Lv, *Anal. Methods*, 2012. **4**(10): 3261-3267.

150. Zhang, Y., J. Tian, S. Liu, L. Wang, X. Qin, W. Lu, G. Chang, Y. Luo, A.M. Asiri, and A.O. Al-Youbi, *Analyst*, 2012. **137**(6): 1325-1328.

151. Chen, W., J. Chen, Y.-B. Feng, L. Hong, Q.-Y. Chen, L.-F. Wu, X.-H. Lin, and X.-H. Xia, *Analyst*, 2012. **137**(7): 1706-1712.

152. Hu, L., Y. Yuan, L. Zhang, J. Zhao, S. Majeed, and G. Xu, *Anal. Chim. Acta*, 2013. **762**: 83-86.

153. Wang, N., B. Li, F. Qiao, J. Sun, H. Fan, and S. Ai, *J. Mater. Chem. B*, 2015. **3**(39): 7718-7723.

154. Dong, Y.-l., H.-g. Zhang, Z.U. Rahman, L. Su, X.-j. Chen, J. Hu, and X.-g. Chen, *Nanoscale*, 2012. **4**(13): 3969-3976.

155. Wang, Q., X. Zhang, L. Huang, Z. Zhang, and S. Dong, *ACS Appl. Mater. Interfaces*, 2017. **9**(8): 7465-7471.

156. Zheng, X., Q. Zhu, H. Song, X. Zhao, T. Yi, H. Chen, and X. Chen, *ACS Appl. Mater. Interfaces*, 2015. **7**(6): 3480-3491.

157. Su, L., W. Qin, H. Zhang, Z.U. Rahman, C. Ren, S. Ma, and X. Chen, *Biosens. Bioelectron.*, 2015. **63**: 384-391.

158. Zhan, T., J. Kang, X. Li, L. Pan, G. Li, and W. Hou, *Sens. Actuators, B*, 2018. **255**: 2635-2642.

159. Liu, Q., Y. Yang, H. Li, R. Zhu, Q. Shao, S. Yang, and J. Xu, *Biosens. Bioelectron.*, 2014. **64**: 147-153.

160. Wang, Q., L. Zhang, C. Shang, Z. Zhang, and S. Dong, *Chem. Commun.*, 2016. **52**(31): 5410-5413.

161. Jin, L., Z. Meng, Y. Zhang, S. Cai, Z. Zhang, C. Li, L. Shang, and Y. Shen, *ACS Appl. Mater. Interfaces*, 2017. **9**(11): 10027-10033.

162. Chen, X., X. Zhou, and J. Hu, *Anal. Methods*, 2012. **4**(7): 2183-2187.

163. Choleva, T.G., V.A. Gatselou, G.Z. Tsogas, and D.L. Giokas, *Microchim. Acta*, 2018. **185**(1): 22.

164. Su, L., J. Feng, X. Zhou, C. Ren, H. Li, and X. Chen, *Anal. Chem.*, 2012. **84**(13): 5753-5758.

165. Newman, J.D. and A.P. Turner, *Biosens. Bioelectron.*, 2005. **20**(12): 2435-2453.

CHAPTER 2

Characterization techniques

This chapter summarises the operating principles of the various characterization methods used during the course of the current work.

2.1 Introduction

In this chapter, the principle underlying the techniques used to characterize the nanomaterials synthesized in this study is described. The techniques include UV-visible Absorption Spectroscopy (UV-vis spectroscopy), Fluorescence Spectroscopy, Atomic Emission Spectroscopy (AES), Scanning Electron Microscopy (SEM), Energy Dispersive X-ray Spectroscopy (EDX), X-ray Diffraction (XRD), and X-ray Photoelectron Spectroscopy (XPS).

2.2 UV-visible Absorption Spectroscopy

The basis for UV-vis absorption spectroscopy is the interaction of light with materials. When a beam of light passes through a solution, the intensity of the emerging radiation is always lesser than the incident radiation. Reflection and scattering play a minor role in the loss of light through the solution. However, a majority of energy loss in the emerging radiation is due to absorption by the particulate matter in the solution. When a material absorbs energy, electrons in the material are excited to higher energy levels. Thus, a correlation between the absorbed energy by the matter and the energy of the incident light beam allows determining the energy required to make an electronic transition from the lower energy state to the excited state using the equation:

$$\Delta E = h\nu = \frac{hc}{\lambda} \qquad \textit{Equation 2.1}$$

where ΔE is the difference in energy between the two energy levels involved in the transition, h is the Planck's constant (6.626×10^{-34} J.s), c is the speed of light (2.997×10^{8} ms^{-1}) and, λ is the incident light wavelength. Beer-Lambert law relates single-photon absorption ie., attenuation of light, to the properties of the material through which it travels [1, 2]. The law

relates the intensity of the incident light to that of the transmitted light through the sample via the equation:

$$log_{10}\frac{I_0}{I} = \varepsilon cl = A \qquad \textit{Equation 2.2}$$

where I_0 is the intensity of incident light, I is the intensity of transmitted light, ε is the molar extinction coefficient of the sample, c is the molar concentration of the absorbing molecules in the sample and, l is the pathlength of light through the sample. A is the simplified form of $log_{10}\frac{I_0}{I}$ which is the absorbance or optical density of the material. A UV-vis spectrum provides an absorbance output (arbitrary unit) that is directly proportional to the concentration of the sample. Using a series of known sample concentrations, a standard curve (or calibration graph) of Absorbance vs. concentration is plotted. A linear curve is obtained if *Beer-Lambert* law is obeyed. This plot is then used to determine the unknown concentration in a test sample. Thus, UV-vis spectroscopy is a quantitative technique for studying reaction kinetics by measuring the rate of change in reactant or product concentration by measuring the change in absorbance of colored solutions over time.

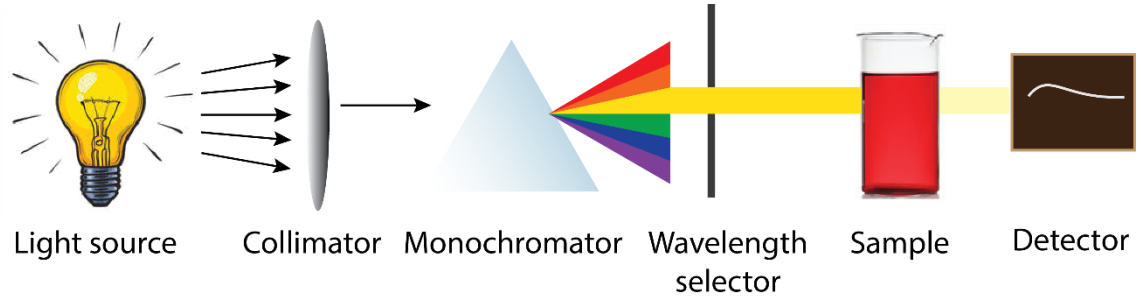

Figure 2.1 *Basic instrumentation of a UV-vis spectrophotometer.*

In this thesis, UV-vis spectroscopic measurements for NanoZyme activity and colorimetric biosensing were obtained on the CLARIOstar plate reader (BMG Labtech), operating at a resolution of 2 nm over a wavelength range of 220-1000 nm.

2.3 Fluorescence Spectroscopy

Fluorescence spectroscopy is based on the analysis of light emitted by a substance when it absorbs electromagnetic radiation. When a beam of light is incident on a fluorophore (fluorescent capable molecule), the π electrons of this molecule are excited to one of the vibrational levels in the excited electronic state by absorbing a photon. Collisions in the excited electronic state cause the molecule to lose vibrational energy and drop to the ground electronic state, emitting a photon in the process [3]. In a typical fluorescence emission measurement, the fixed wavelength of light illuminates the fluorophore and the emission is detected over a range of wavelength. This technique can be used both for qualitative and quantitative analysis. The shape and intensity of the fluorescence spectra are influenced by the excitation wavelength, concentration of the analyte solvent, incident light absorption by the sample and path length of light.

In this work, fluorescence spectroscopic measurement for the generation of hydroxyl radicals (˙OH radicals) was carried out on the CLARIOstar plate reader (BMG Labtech). The fluorescence spectra were recorded between 325 and 550 nm using terephthalic acid as a fluorescent probe that was excited at 315 nm.

2.4 Atomic Emission Spectroscopy (AES)

Atomic emission spectroscopy is a chemical analysis technique where the light emitted from a flame, arc, plasma or spark is used to identify the element as well as its quantity in the sample. The analyte is first aerosolized using an atomizer. This sample is then exposed to a flame to supply energy to the atoms in the form of heat. Depending on the type of atom, they each take up different amounts of energy and thereby jump to their corresponding higher energy levels. When the atoms fall back to their original energy level, they give out energy in

the form of photons (light). Each element has a unique wavelength of emission [4]. The emission wavelength can be measured to determine the type of element present in the sample, and the intensity of emission is proportional to the concentration of the element. AES allows for both qualitative and quantitative analysis.

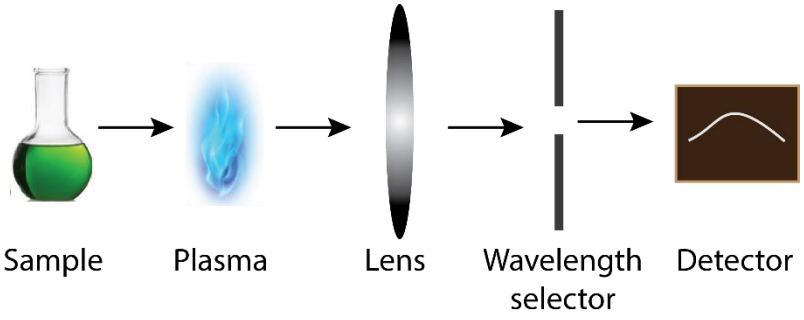

Figure 2.2 *Schematic representation of AES.*

In the current work, the metal ion content in the synthesized nanomaterials was measured on the Agilent 4100 Microwave Plasma-Atomic Emission Spectrometer (MP-AES).

2.5 Scanning Electron Microscopy (SEM)

Morphological characterization of nanomaterials is typically done on electron microscopes. The working principle of electron microscopes is based on conventional optical microscopes. In the case of electron microscopes, the sample illumination source is electron beam instead of light, electromagnets focus the beam in place of glass lens and the detector is an electron detector. Image resolution in electron microscopes is much higher as the wavelength of an electron beam is in the Angstrom order. Scanning electron microscopy is a type of electron microscopic technique that creates a magnified image of a sample surface by focusing a beam of electrons on the sample followed by creating an image using the electrons that come out of the sample [5]. In SEM, an electron gun generates a high energy electron beam, which is then focussed onto the specimen surface by electromagnets. The electron beams systematically

rasters across the sample surface. Electron beam interaction with the sample results in the generation of low-energy secondary electrons, backscattered electrons, X-ray emission, Auger electrons, and photons. Secondary electrons are ejected from the sample surface when the incident electron beam knocks into atoms and displaces electrons. They possess low energy and are ideal for topographical analysis. Backscattered electrons are the elastically scattered electrons from the incident beam. The trajectory of these electrons within the sample changes but its energy and velocity essentially remains constant. They are generated from deeper within the sample and thus give information on the physical and chemical characteristics of the sample. Characteristic X-rays are emitted when an electron in a higher energy shell transitions to a lower energy shell to take the place of an electron-hole that was created by the incident electron beam exciting an electron in the inner shell. These X-rays are analyzed using an energy dispersive X-ray spectrometry (EDX). Backscattered electrons and secondary electrons together contribute to the development of a pseudo three dimensional SEM image. The electron detector collects the signal generated from the sample. Secondary electrons are usually used to image sample surface. Sample shape majorly influences the signal generated with brighter spots at the edges and pointy ends.

The SEM imaging of all nanomaterials used in this study was done on the FEI Verios XHR-SEM.

2.6 Energy Dispersive X-ray Spectroscopy (EDX)

Energy dispersive X-ray spectroscopy is a characterization technique for qualitative and quantitative analysis of the elemental composition of a sample. The basic principle for this method is that each element exhibits a unique electromagnetic emission spectrum because of its atomic structure [6]. The sample is excited by focussing an electron beam in either a scanning electron or transmission electron microscope. The beam electrons interact with the

atoms that make up the sample by exciting an electron in an inner shell. This creates an electron-hole which is then filled by another electron from the outer, higher-energy shell. The difference in energy between the higher energy and lower energy shell triggers the emission of energy in the form of X-rays. Two types of X-ray emission is observed: Bremsstrahlung X-rays and Characteristic X-rays. The Energy Dispersive detector detects the X-rays and displays the output as the intensity or number of X-rays versus the X-ray energy. The energy associated with each characteristic X-ray corresponds to a specific element, while the intensity of this X-ray quantifies the concentration of the element in the sample. The incident beam penetrates the sample in a tear-drop like shape and the X-rays emitted reach the detector from further inside the sample. Thus, estimation of relative abundance of elements in a sample is possible along with measurement of layer thickness in multi-layer metallic samples and analysis of alloys. An EDX map shows the distribution of elements on the surface of the sample by rastering the electron beam across the surface followed by correlating the X-rays detected with the position of the beam.

In this thesis, EDX analysis was performed on the FEI Verios XHR-SEM fitted with Oxford X-Max 20 Silicon Drift Detector.

2.7 X-ray Diffraction (XRD)

Characterization of nanomaterials by X-ray diffraction provides information on the composition and crystal structure of the material. This technique is based on the diffraction of incident monochromatic X-rays when it hits a crystalline structure [7]. When a material is bombarded with a beam of X-ray (generated using a cathode ray tube), the crystal structure that makes up the material diffracts the beam in specific directions. The angle of diffraction depends on the unit cell dimensions and lattice structure of the crystal while the geometrical dependence of the component atoms on the lattice points influences the diffracted beam

intensity. X-rays scattered by atoms at different positions are collected by the detector with a relative phase shift. The intensity of X-rays scattered from the crystal is then measured. An interference pattern that corresponds to the diffraction angle and relative atomic position is generated. The crystal structure is then determined by applying Bragg's law to the interference pattern. Bragg's equation describes the principle of X-ray diffraction as:

$$n\lambda = 2d \sin\theta \qquad \textit{Equation 2.3}$$

where n is the positive integer representing the order of diffraction, λ is the wavelength of the incident X-ray, d is the interplanar distance of the atoms in the material and, θ is the angle of diffraction. When the diffraction angle and the wavelength of incident X-ray are known, the Bragg equation can be rearranged to calculate the interplanar spacing.

$$d = \frac{n\lambda}{2 \sin\theta} \qquad \textit{Equation 2.4}$$

Thus, structural details of the nanomaterial such as the crystal planes can be determined by a non-destructive method.

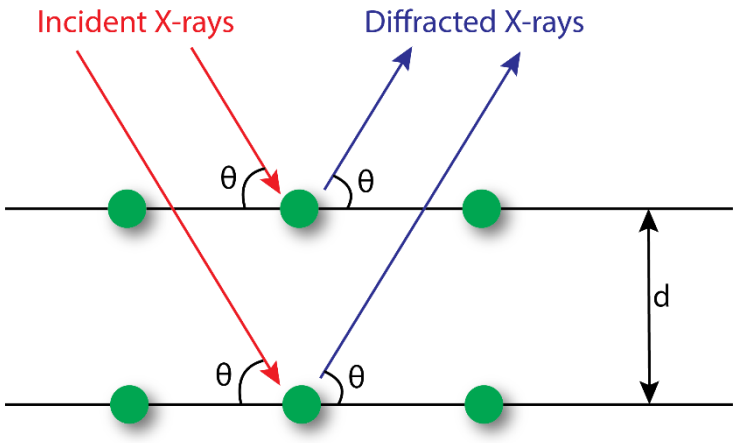

Figure 2.3 *Schematic of Bragg's diffraction law.*

The XRD patterns presented in this work were obtained using Bruker D4 Endeavour operated at a voltage of 40 kV and 40 mA current with Cu Kα radiation source.

2.8 X-ray Photoelectron Spectroscopy (XPS)

X-ray photoelectron spectroscopy is a surface-sensitive technique that provides information on the composition and electronic transitional state of the elements on the surface of the material. The technique is based on the Photoelectric Effect which is the emission of electrons or other free carriers when illuminated by light [8]. In XPS, a sample is irradiated by a beam of X-ray under ultra-high vacuum (UHV) of 10^{-9} – 10^{-10} Torr. X-ray interaction with the sample causes ionization of surface atoms leading to the emission of core electrons (photoelectrons). The binding energy of the electrons that are emitted can be determined by using the equation developed with the efforts of Ernest Rutherford:

$$KE = h\nu - BE - \Phi \qquad \textit{Equation 2.5}$$

where *KE* is the kinetic energy of the photoelectron, *hν* is the energy of the incident X-ray photon, *BE* is the binding energy of the electron to its associated orbital, Φ is the work function that is dependent on the spectrophotometer and the material. The kinetic energy of the emitted electron is measured and using the other known parameters, the binding energy of the electron is calculated. The binding energy of each element's orbitals is unique and thus characteristic peaks appear in the spectra corresponding to the electron configuration within the atoms. The intensity of each peak is directly proportional to the amount of that element in the sample. Thus using XPS we can determine the elements that make up the sample along with their oxidation states and the other elements they are bonded to.

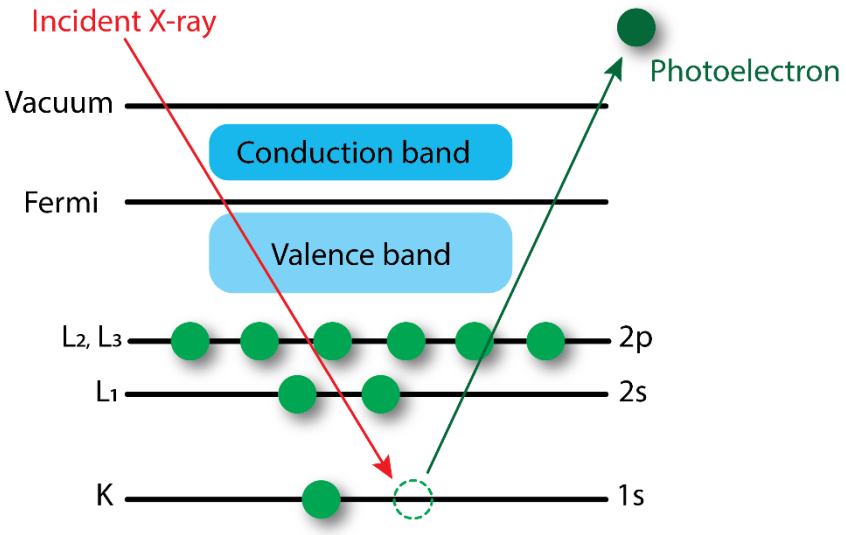

Figure 2.4 *Schematic representation of the principle of XPS.*

In this work, XPS measurements were recorded on the Thermo K-Alpha XPS instrument with Al Kα radiation and 1486.6 eV photon energy. Shirley algorithm was used for background correction of core-level spectra and chemically distinct species were resolved using non-linear least-squares fitting procedure. Core level binding energies were charge corrected with adventitious carbon binding energy (285 eV).

2.9 References

1. Fleming, I. and D.H. Williams, *Spectroscopic methods in organic chemistry*. 1966: McGraw-Hill New York.
2. Pungor, E. and G. Horvai, *A practical guide to instrumental analysis*. 1994: CRC press.
3. Schulman, S.G., *Fluorescence and phosphorescence spectroscopy: physicochemical principles and practice*. 2017: Elsevier.
4. Skoog, D.A., F.J. Holler, and S.R. Crouch, *Principles of instrumental analysis*. 2017: Cengage learning.
5. Zhou, W. and Z.L. Wang, *Scanning microscopy for nanotechnology: techniques and applications*. 2007: Springer science & business media.
6. Goldstein, J.I., D.E. Newbury, J.R. Michael, N.W. Ritchie, J.H.J. Scott, and D.C. Joy, *Scanning electron microscopy and X-ray microanalysis*. 2017: Springer.

7. Waseda, Y., E. Matsubara, and K. Shinoda, *X-ray diffraction crystallography: introduction, examples and solved problems*. 2011: Springer Science & Business Media.

8. Hofmann, S., *Auger-and X-ray photoelectron spectroscopy in materials science: a user-oriented guide*. Vol. 49. 2012: Springer Science & Business Media.

CHAPTER 3

Copper nanoparticles embedded within a matrix of cotton fabric as recoverable NanoZyme catalyst for the colorimetric detection of glucose in urine

Long-term effects of *Diabetes mellitus* include renal complications where glucose is eliminated in the urine. Therefore, it is important to detect glucose in both blood and urine. While commercial urine strips are user-friendly, they have limitations in terms of sensitivity and are typically time-sensitive. As an alternative, enzyme-mimicking catalytic behaviour of nanoparticles (NanoZymes) have been exploited to develop glucose sensors. While solution-based NanoZymes look promising, they are limited to detecting low concentrations of glucose. Given that the concentration of glucose in urine is typically high, NanoZyme loading on absorbent templates is a simple strategy to increase the concentration of the NanoZyme catalyst. In this chapter, the ability of copper nanoparticles to promote the catalytic oxidation of peroxidase substrate TMB to its second oxidation product (yellow) is shown. The high catalytic efficiency allowed the sensor to push the linear operational dynamic range for glucose sensing from 0.5 mM – 15 mM. The robustness of the sensing platform was established by evaluating its ability to detect urine glucose in diabetic urine samples without any need for sample dilution.

3.1 Introduction

Glucose is a molecule of significant interest as it is regarded as the central source of energy. Its homeostasis is critical to human health. Glucose at abnormal levels in the blood is the primary symptom of *Diabetes mellitus* [1]. WHO reports that its prevalence is rapid in low and middle-income countries and estimates that one in two adults has undiagnosed diabetes [1]. The key to diabetes management is to monitor and control the level of glucose in the body frequently. Current glucose monitors use invasive methods for blood extraction that serves as the source of sample [2, 3]. A new technology – continuous glucose monitoring (CGM) is well recognized but the costs associated with this technology limits its application to high-income populations. In addition to blood, urine glucose is also important as it allows to monitor renal functions [2, 3]. This is due to the fact that high glucose levels or extended periods of high glucose as observed in Type I juvenile diabetes can lead to renal glycosuria. In this case, urine glucose levels can be significantly high even if the blood glucose levels are normal [4]. Therefore, it is essential to develop analytical tools that will accurately monitor urine glucose levels. Additionally, using urine as a sample for detection is non-invasive, can reduce patient discomfort and has high usefulness in low resource settings to screen for undiagnosed diabetes with minimal infrastructure where blood-based tests are not a viable option [5].

Glucose monitoring tools typically use a combination of glucose oxidase (GOx) – Horseradish Peroxidase (HRP) enzyme for detection. In this reaction, GOx oxidises glucose to produce gluconic acid and H_2O_2 as a by-product. The H_2O_2 then serves as a substrate for HRP to catalyse the conversion of a non-colored substrate to a colored product [6, 7]. A potential issue with this system is that peroxidases, ubiquitous enzymes that catalyse a variety of oxygen-transfer reaction, are unstable and can be inactivated by their substrate, hydrogen

peroxide (H_2O_2) [8, 9]. Therefore, new strategies are being developed to either improve the stability of HRP [6, 10] or explore artificial enzymes as a potential alternative [11-15]. One such artificial enzyme technology is '*NanoZymes*' where it was shown that nanoparticles possess intrinsic enzyme-mimic activity. NanoZymes are inorganic by nature and are a subset of inorganic catalysts [11-15]. The enzyme-mimicking activity is dominated by the composition, size, shape, surface characteristics of the nanoparticles and the catalytic activity can be fine-tuned by optimizing the reaction conditions [11-22] and in some cases, can be regulated by external stimuli such as light or molecular imprinting [16, 23-25]. Given that inorganic nanoparticles have high ambient stability than organic enzymes and have enzyme-mimic activity at physiological conditions, NanoZymes have been recognized as a potential alternative to natural enzymes [11-15, 26-35]. Additionally, the use of nanoparticles will also allow easy surface modification to attach recognition moieties that can aid in the detection of specific molecules [11, 12, 17, 18, 36]. Therefore, it is unsurprising to see that NanoZymes have been explored in sensing, antibacterial, pro-drug therapy, and environmental clean-up applications [11-13, 15-18, 21, 22, 36, 37].

In the context of sensing applications, NanoZyme-based sensors provide a colorimetric response *i.e.* change in the color of the solution, allowing for visual eye detection [11-13, 15, 17-20, 38] in comparison to other sensing platforms [39-45]. Particularly, water-dispersible colloidal NanoZymes have been at the forefront of developing sensors for glucose detection [46-51]. However, when using colloidal NanoZymes, due to the high concentrations of glucose in urine, the NanoZyme activity will rapidly saturate and limit the dynamic operating range of the sensor [46]. It is possible to increase the concentration of the NanoZyme to improve the dynamic range [18]. But the potential interference of colloidal nanoparticles in visual detection either due to SPR (metal nanoparticles) and/or scattering can lead to inaccurate sensor response [52-54]. One simple strategy to increase the NanoZyme

concentration without potential interference is to immobilize nanoparticles on three-dimensional (3D) templates. Recent works have shown the potential of using cotton textile/buds as a template due to its porosity, absorbency, and hierarchical structuring [19, 41, 44, 55-57] allowing easy access to a large number of catalytically active sites to promote heterogeneous catalysis reactions [55, 56] and develop gas sensors and flexible electronic devices [41, 44, 58]. By increasing the nanoparticle loading on cotton textiles, the ability of Ag@Fabric to detect mM level of glucose in urine samples with high accuracy was recently shown [19].

In the current chapter, the ability of copper to promote catalytic reactions with high efficiency is exploited to develop a glucose monitoring system. For this, catalytically active copper nanoparticles were first embedded within the 3D matrix of cotton fabrics. The high catalytic efficiency of the Cu@Fabric NanoZyme was evident from its ability to promote the oxidation of TMB to its second oxidation product (yellow) rather than the relatively stable charge-transfer complex product (blue). This is the first time the ability of a NanoZyme to form the yellow product without the addition of sulfuric acid is shown. Further, due to the high catalytic efficiency, the linear operational dynamic range for glucose sensing was pushed from 0.5 mM – 15 mM. The practical applicability of the sensing system was established by accurately quantifying glucose concentrations in urine samples obtained from a healthy and diabetic volunteer. The high recovery obtained outlines the robustness of the Cu@Fabric NanoZyme system.

3.2 Materials and methods

3.2.1 Materials and reagents

Tin(II) chloride ($SnCl_2$), palladium(II) nitrate ($Pd(NO_3)_2$), sodium hydroxide (NaOH), potassium sodium tartrate tetrahydrate ($C_4H_4KNaO_6 \cdot 4H_2O$), copper sulfate pentahydrate

($CuSO_4 \cdot 5H_2O$), formaldehyde (CH_2O, 36.5-38% in H_2O), 3,3′,5,5′-tetramethylbenzidine (TMB), 2,2′-azino-bis(3-ethylbenzothiazoline-6-sulphonic acid) (ABTS), o-phenylenediamine dihydrochloride (OPD), sodium acetate anhydrous ($C_2H_3NaO_2$), acetic acid (CH_3COOH), terephthalic acid (TA), glucose ($C_6H_{12}O_6$), glucose oxidase (GOx from *Aspergillus niger*), horseradish peroxidase (HRP), sucrose ($C_{12}H_{22}O_{11}$), fructose ($C_6H_{12}O_6$), lactose ($C_{12}H_{22}O_{11}$), maltose ($C_{12}H_{22}O_{11}$) were purchased from Sigma-Aldrich, Australia. Hydrogen peroxide (H_2O_2, 30% w/w) was purchased from Chem-Supply Pty Ltd. Cotton fabric was bought from the local market. Milli-Q water (18.2 MΩ cm) was obtained from a Millipore Milli-Q water purification system.

3.2.2 Synthesis of Cu@Fabric

The Cu@Fabric was fabricated according to previous reports [55, 56]. The individual fibers of a cotton fabric were coated with copper nanoparticles through an electroless deposition technique. 20 pieces of 1 cm × 1 cm cotton fabric were first sensitized in an acidic $SnCl_2$ solution (3.0 mM) for 1 hour. Followed by a quick wash with deionized water, the sensitized fabrics were exposed to aqueous $Pd(NO_3)_2$ (3.0 mM) for 30 minutes. A simple galvanic replacement reaction results in the formation of Pd^0 nuclei that act as seeds for copper deposition [55, 56]. The Pd^0 fabrics were exposed to a solution containing NaOH (1 M), potassium sodium tartrate (0.3 M), copper(II) sulfate (0.1 M) and formaldehyde (0.5 M) for 5 hours at 55°C.

3.2.3 Characterisation

The Cu@Fabric was immobilized on an aluminum stub for imaging by Scanning Electron Microscopy (SEM) using a FEI Verios SEM instrument operating at an accelerating voltage of 30 kV. EDX analysis was performed on the FEI Verios SEM fitted with an Oxford X-Max 20 Silicon Drift Detector. X-ray diffraction measurements were performed on Bruker D8

Advance XRD instrument operated at 40 kV and 40 mA with Cu Kα radiation. X-ray photoelectron spectroscopy (XPS) analysis was carried out using a Thermo K-Alpha XPS instrument (Al Kα radiation, photon energy of 1486.6 eV) with Cu 2p core level binding energy recorded at the pass energy of 20 eV. The spectrum was background corrected using a Shirley background algorithm and chemically distinct species were resolved using a nonlinear least squares fitting procedure [59] and the core level binding energy (BE) was charge corrected with adventitious carbon (285 eV).

3.2.4 Peroxidase-mimic NanoZyme activity of Cu@Fabric

The peroxidase-mimic activity of the Cu@Fabric (0.5 cm × 0.5 cm) NanoZyme was first confirmed by its ability to promote the oxidation of colorless peroxidase substrate – TMB to its colored product in the presence of H_2O_2 with λ_{max} at 652 nm (blue for one-electron oxidation) or 450 nm (yellow for two-electron oxidation). The reaction was carried out in 50 mM NaAc buffer (pH 5) containing 0.2 mM TMB and 10 mM H_2O_2 at 37 °C. Post-reaction, the Cu@Fabric was extracted from the reaction for spectroscopic measurements. The reaction was monitored as a function of time using CLARIOstar plate reader (BMG Labtech). The ability of the NanoZyme to oxidise other peroxidase substrates were also tested using OPD and ABTS and the oxidation product was assessed at λ_{max} 417 nm and 420 nm, respectively. The intrinsic peroxidase-mimic activity of the Cu@Fabric NanoZyme was confirmed by assessing the activity of potentially leached Cu ions. For this, the Cu@Fabric was incubated in 50 mM NaAc buffer (pH 5) for 30 min. The potential leached ions were then used as catalyst using similar conditions as used previously. The reaction conditions were optimized by varying the NanoZyme concentration (149 – 1430 ppm equivalent of Cu ions), pH (2 – 10) and temperature (25 – 60 °C), where all reaction conditions were kept consistent. Steady-state kinetic analysis was performed at a fixed concentration of Cu and independently varying the concentration of H_2O_2 (5 – 40mM) and TMB (0.05 – 0.8 mM). The colorimetric response

was fitted to Michaelis-Menten plot using OriginPro 2016. Important enzyme-kinetic parameters such as Michaelis-Menten constant (K_m) and maximum reaction velocity (V_{max}) were calculated using equation 1.

$$\frac{1}{V_0} = \frac{K_m}{V_{max}}\left(\frac{1}{[S]} + \frac{1}{K_m}\right) \qquad \textit{Equation 3.1}$$

where V_0 corresponds to the initial reaction velocity, V_{max} denotes the maximum reaction velocity, [S] is the substrate concentration, and K_m represents the Michaelis-Menten constant.

3.2.5 Mechanism of peroxidase-mimic activity

The catalytic mechanism of H_2O_2 degradation to form hydroxyl radicals by the Cu@Fabric NanoZyme was established using a fluorescence assay where terephthalic acid (TA) was used as a capture probe for ˙OH radicals. TA captures ˙OH radicals to form a fluorescent 2-hydroxyterephthalic acid and can be measured between 325 and 550 nm (excitation wavelength of 315 nm) using a CLARIOstar plate reader (BMG Labtech). The reaction includes 10 mM H_2O_2 and 1 mM TA with Cu@Fabric (0.5 cm × 0.5 cm containing 540 ppm equivalent of Cu ions) in 50 mM NaAc buffer (pH 5) at 37°C.

3.2.6 Colorimetric detection of glucose

In contrast to the previous work with Ag@Fabric where a two-step process was carried out, glucose detection was carried out in a single step. The reaction containing a mixture of 2 mg mL^{-1} glucose oxidase (50 µL), glucose (5-200 mM stock, 50 µL), 12.5 mM TMB (20 µL) and 50 mM NaAc buffer at pH 5 (380 µL) – Total reaction volume of 500 µL was incubated at 37 °C for 20 min for the GOx to react with glucose. To this mixture, a piece of the Cu@Fabric NanoZyme (0.5 cm × 0.5 cm containing 540 ppm equivalent of Cu ions) was added and incubated for 10 min at 37 °C. The Cu@Fabric NanoZyme was extracted after 10 min to stop the reaction and the oxidation product was recorded at 652 nm. The dynamic linear range was

calculated by plotting the Absorbance λ_{max} against glucose concentration. The line of best fit was determined using OriginPro2016 using a direct weighting method. Important sensor parameters such as the limit of detection (LoD), accuracy and precision were calculated. LoD was calculated using the formula 3.3*(SD of the Y-intercept/slope). Accuracy and precision were calculated by considering the colorimetric response obtained from 15 independent experiments. The accuracy was determined by using (n/N) × 100 formula at 10% confidence interval where n represents the sensing events that fall within the target glucose responses and N is the total number of test events. The % precision was calculated by the coefficient of variation (CoV) method using the formula % Precision = 100 − %CoV. Specificity was assessed by measuring the sensor response in the presence of 10 mM glucose analogues *viz.* lactose, sucrose, fructose, and maltose independently. The response was also measured when using a combination of glucose analogues (10 mM) and glucose (5 mM).

Glucose detection in urine was carried out in urine samples obtained from a healthy and diabetic volunteer (samples stored at 4 °C until used). Before using the sample, the urine was centrifuged at 14,500 RPM for 15 min to remove any cells and other debris. The glucose concentration was determined by three methods.

Method 1: GOx-HRP – 50 µL of 2 mg mL^{-1} GOx, 50 µL urine sample and 20 µL of TMB (12.5 mM) were incubated at 37 °C for 20 min in 360 µL of 50 mM NaAc buffer at pH 5. 20 µL HRP (40 ng mL^{-1}) was then added to the above solution and a further incubated of 10 min at 37 °C. The TMB oxidised product was recorded at 652 nm.

Method 2: Cu@Fabric NanoZyme – The process is similar to that described for Method 1 except that the Cu@Fabric (0.5 cm × 0.5 cm containing 540 ppm equivalent of Cu ions) was added in place of HRP. A point to highlight is the fact that the buffer condition was not changed as shown in previous reports of using NanoZymes [19].

Method 3: Urine glucose dipstick – the commercial test strip by Bayer, Diastix was exposed to urine samples for 30 sec. Following which the color developed on the test pad was matched against the reference color chart to determine the approximate amount of glucose in the sample.

3.3 Results and discussion

3.3.1 Fabrication and characterization of Cu@Fabric

The deposition of copper nanoparticles on individual threads of a cotton fabric occurs via an electroless process. During this, the cotton fabric is first sensitized using acidic tin chloride solution where Sn^{2+} ions bind to the fabric. The Sn^{2+} ions facilitate the galvanic replacement reaction in the second step where the favorable potentials between $Sn^{2+/4+}$ (+0.15 V *vs* SHE - standard hydrogen electrode) and $Pd^{2+/0}$ (+0.99 V *vs* SHE) allow the Pd^{0} nanoparticles to be formed on the surface of the fabric with concomitant release of Sn^{4+} ions into the solution [55, 56]. Although this step is not essential, it was previously reported that the Pd^{0} increases the rate of Cu deposition [55]. In the last step of copper nanoparticle deposition, copper sulfate which is complexed with sodium potassium tartrate is reduced by formaldehyde under alkaline conditions. The complexation of copper to sodium potassium tartrate is essential as it regulates the concentration of metal ions during the deposition process and allows for the reaction to proceed at higher pH [60]. The amount of Cu deposited was calculated using atomic emission spectroscopy (AES). For this, a standard curve with known concentrations of Cu was used. The amount of Cu deposited on the fabric was determined by measuring the unreacted Cu in the solution post-reaction. A total of 540 ± 30 ppm of Cu was deposited on 0.5 cm × 0.5 cm fabric.

The deposition of copper on cotton fabric results in the formation of sub-100 nm quasi-spherical copper nanostructures as observed in the SEM image (**Figure 3.1**a). The

deposition resulted in a reddish-brown fabric color which is due to the collective localized surface plasmon resonance (LSPR) of the sub-100 nm copper nanoparticles [55, 56, 59]. The EDX elemental map further shows the uniform distribution of copper nanoparticles across the fabric surface (**Figure 3.1**b). Characteristic energy lines of C Kα (0.277 keV), O Kα (0.524 keV), Cu Lα (0.929 keV), Cu Kα (8.04 keV) and Cu Kβ (8.89 keV) were observed in the EDX spectrum (**Figure 3.1**c). The energy lines of C Kα and O Kα is predominately from the underlying cotton fabric [55], while the Cu energy lines arise from the copper nanoparticles.

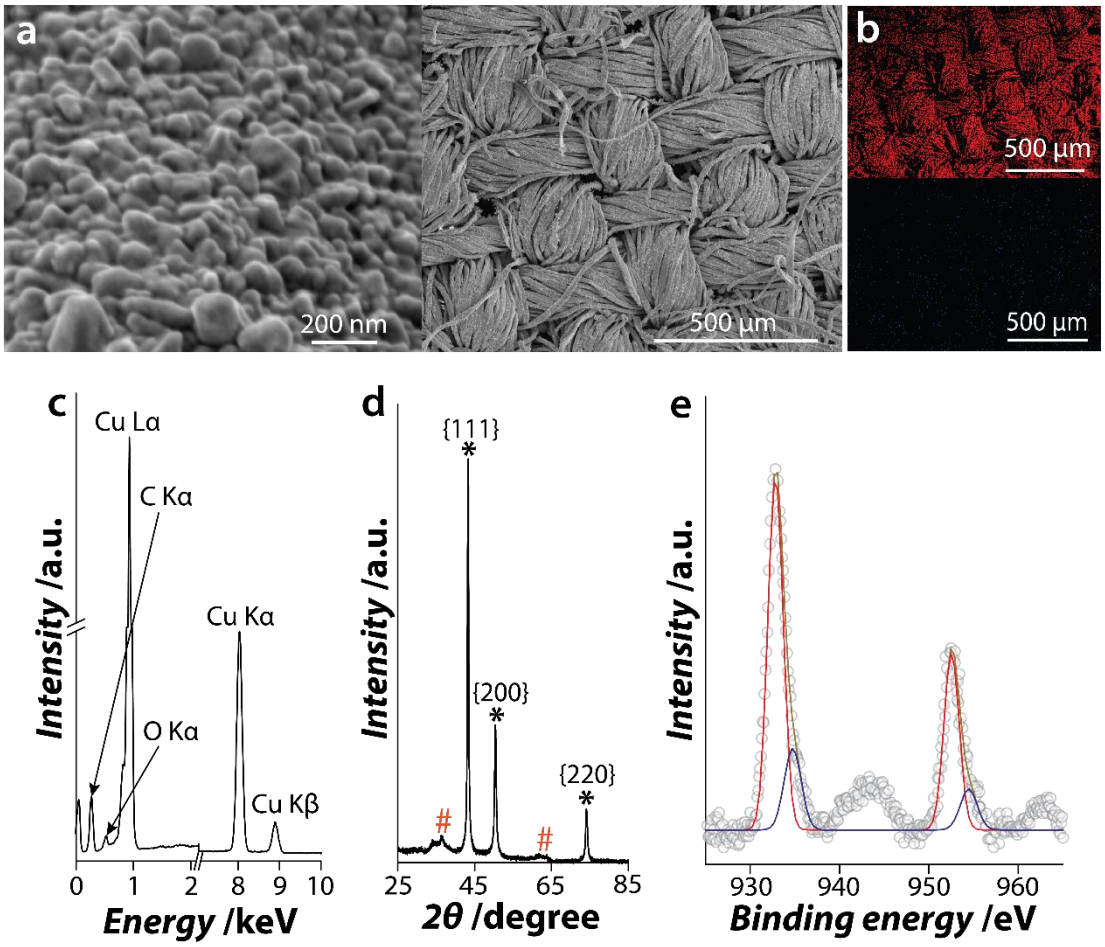

Figure 3.1 *Materials characterization of Cu@Fabric.* ***(a)*** *high and low magnification SEM image of the Cu@Fabric;* ***(b)*** *EDX layered map containing the elemental distribution of Cu and O (in red and green respectively);* ***(c)*** *EDX spectrum obtained from scanning an area of the Cu@Fabric;* ***(d)*** *XRD pattern obtained from Cu@Fabric where * symbol represents Cu (JCPDS 85-1326) and the # symbol represents CuO (JCPDS 78-0428); and* ***(e)*** *XPS core level spectrum of Cu 2p obtained from Cu@Fabric.*

The crystalline nature of the copper nanoparticles was determined using XRD (**Figure 3.1**d) where typical Bragg reflections corresponding to metallic Cu nanoparticles were observed (JCPDS 85-1326). Bragg reflections corresponding to cupric oxide (CuO marked by #) were also observed. This is due to the high propensity of copper to oxidise in air [59]. XPS analysis was also performed to understand the oxidation states of the copper nanoparticles (**Figure 3.1**e). The Cu 2p core level shows characteristic $2p_{3/2}$ and $2p_{1/2}$ splitting components (spin-orbit splitting ≈19.7 eV) and could be deconvoluted into two discrete $2p_{3/2}$ components at binding energies (BE) of *ca*. 932.8 and 934.7 eV. These correspond to copper in the zerovalent (Cu^0) and Cu^{2+} oxidation states, respectively [59]. The shake-up satellites at *ca*. 943.5 and 964 eV also corroborates the formation of the CuO or Cu in the +2 oxidation state as observed in the XRD [59].

3.3.2 Enzyme-like activity of free-standing Cu@Fabric NanoZyme

The peroxidase-mimic activity of Cu@Fabric was evaluated using a chromogenic peroxidase substrate – TMB. In the presence of H_2O_2 and the Cu@Fabric, a blue-colored product was observed within 5 min of the reaction (**Figure 3.2**a). This product is due to the loss of a single electron from TMB resulting in a charge-transfer complex [61, 62]. This complex is reported to be quite stable where a rapid equilibrium is achieved between the parent diamine TMB, cation radical (TMB_{ox} – λ_{max} = 652 nm) and the diimine derivative (double oxidised product) [62] (**Figure 3.2**b). The blue-colored charge-transfer complex is the most commonly reported product when peroxidase-mimic NanoZymes are used as a catalyst [19, 46, 51]. In this case, when the reaction was monitored as a function of time, the blue colored charge transfer product is further oxidised (loss of another single electron) to the yellow-colored diimine derivative (λ_{max} = 450 nm) forming a blue-green/yellow-green colored solution after 15 min of the reaction (green color arises due to the mixture of yellow and blue). Typically, the

double oxidised diimine derivative from the charge transfer complex is formed only after the addition of a strong acid such as sulfuric acid (stop reagent) and drops the pH to 1 [63, 64].

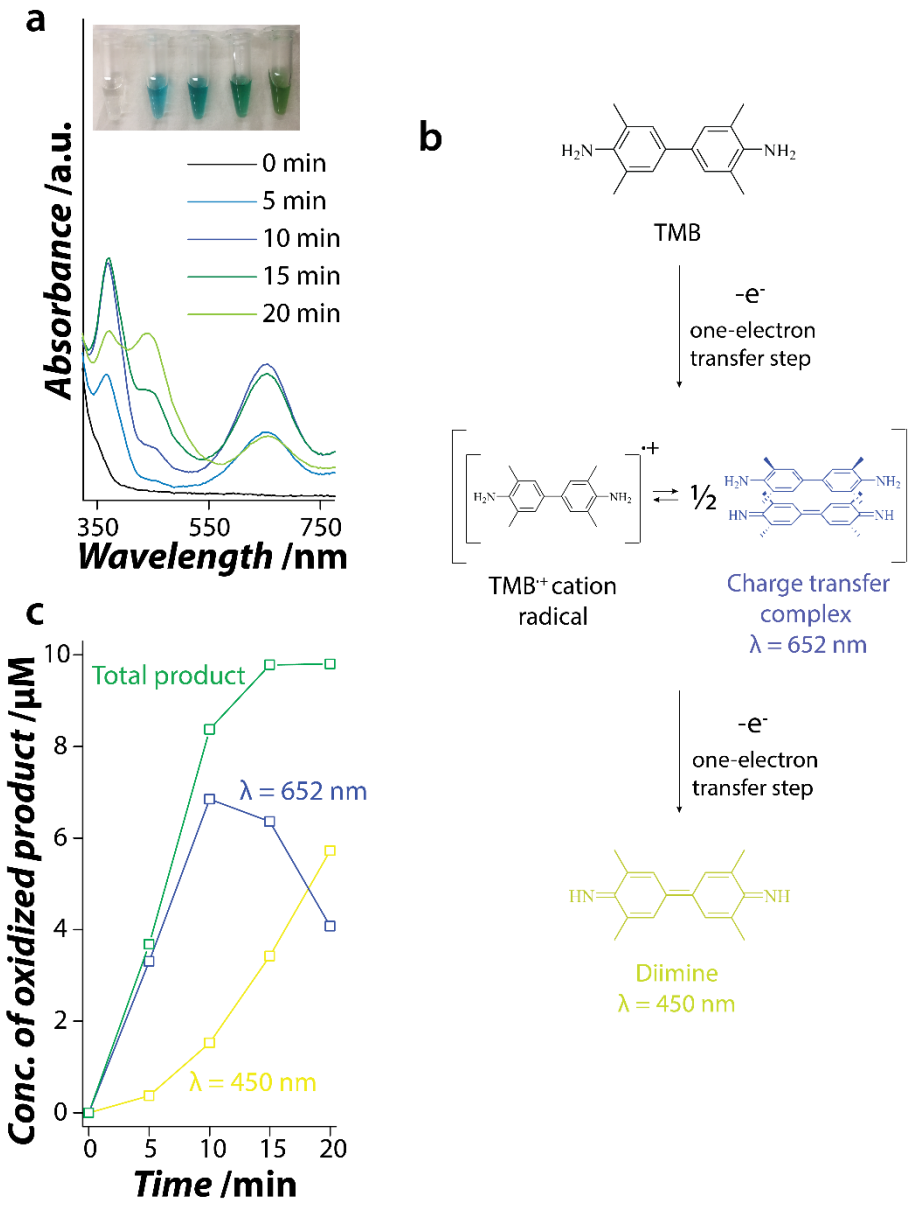

Figure 3.2 *NanoZyme performance of Cu@Fabric (0.5 cm × 0.5 cm containing 540 ppm equivalent of Cu ions).* ***(a)*** *UV-vis absorbance spectra of TMB oxidation recorded as a function of time. Inset shows the optical image of the corresponding oxidised TMB product;* ***(b)*** *Mechanism of the TMB oxidation pathway;* ***(c)*** *the concentration of the charge transfer complex and diimine derivative and the total concentration of the oxidised products.*

In the current case, the ability of the Cu-based NanoZyme system to push the reaction to the second oxidised diimine derivative at mildly acidic conditions outlines the high catalytic efficiency of copper nanoparticles. To further understand the formation of each of the products, the absorbance values were converted to the corresponding concentrations using Beer-Lambert law [65]. **Figure 3.2**c shows the concentration of each product formed during the reaction. At initial time points, the high catalytic ability of copper nanoparticles results in the rapid production of the blue colored charge transfer complex, while only a small proportion of the complex is converted to its diimine derivative. With time, a decrease in the concentration of the blue product with a concomitant increase in the double oxidised diimine derivative is observed.

To confirm that the oxidation of TMB was due to the inherent peroxidase-mimic activity of the Cu@Fabric, control experiments were performed where the reaction either did not contain H_2O_2 or Cu@Fabric. TMB oxidation was not observed, in either case, ascertaining the inherent peroxidase-mimic catalytic behavior of the Cu@Fabric NanoZyme (**Figure 3.3**a). The inability of the Cu@Fabric to oxidise TMB in the absence of H_2O_2 further suggests that the NanoZyme does not posses any oxidase-mimic activity. The peroxidase-mimic activity of the Cu@Fabric was also validated using other commonly used peroxidase substrates such as OPD and ABTS (**Figure 3.3**b). It was found that the Cu@Fabric had the ability to promote the oxidation of OPD, albeit two times lower than that observed for TMB. However, the oxidised ABTS was ~10 times lower than the oxidised TMB product. This suggests that the Cu@Fabric had higher potential to oxidise positively charged substrates (TMB, OPD) in comparison to negatively charged substrates (ABTS) [20]. Given the high propensity of the Cu@Fabric NanoZyme to oxidise TMB, subsequent studies were performed using TMB as the preferred substrate.

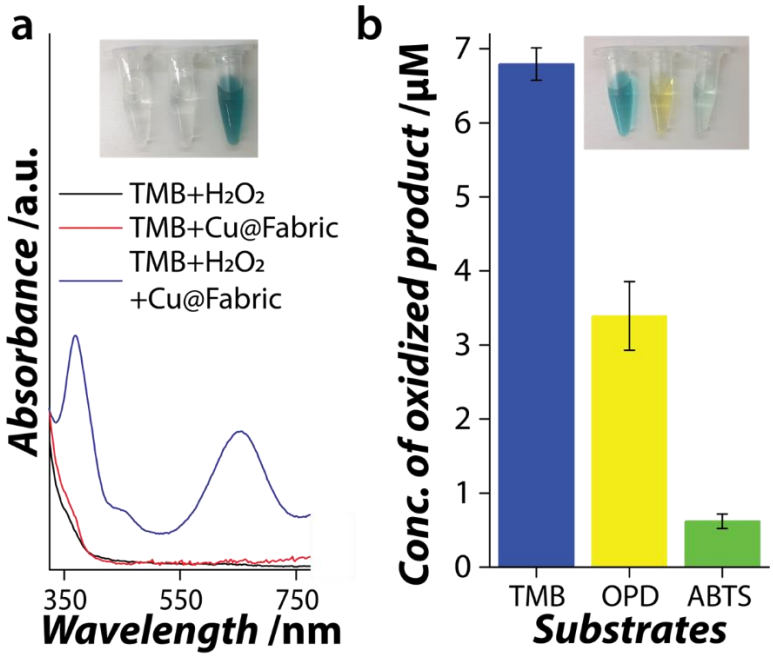

Figure 3.3 *(a) UV-vis absorbance spectra of oxidised TMB catalysed by Cu@Fabric after 10 minutes of reaction under different reaction conditions: (i) TMB + H_2O_2, (ii) Cu@Fabric + TMB, (iii) Cu@Fabric + TMB + H_2O_2; inset are the corresponding optical images post-reaction. (b) Total concentration of oxidised product of TMB, ABTS and OPD after their reaction with Cu@Fabric NanoZyme catalyst. Reaction conditions: Cu@Fabric (0.5 cm × 0.5 cm containing 540 ppm equivalent of Cu ions), 0.2 mM TMB, OPD and ABTS, 10 mM H_2O_2 in 50 mM NaAc buffer (pH 5) at 37 °C.*

To assess if the potential leaching of Cu ions participated in driving the oxidation of TMB, the Cu@Fabric was first incubated in NaAc buffer (pH 5) for 30 min. Following the incubation, the solution containing the potential leached ions were used as a catalyst. Minimal catalytic activity was observed in the case of potential leached ions as catalyst in comparison to the Cu@Fabric NanoZyme catalyst ascertaining that the NanoZyme activity was not due to the potentially leached Cu ions (**Figure 3.4**).

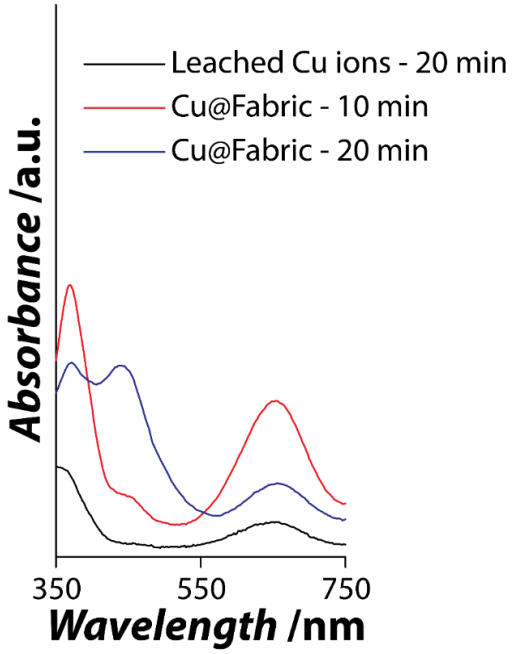

Figure 3.4 *Absorbance spectra of peroxidase-mimic reaction catalysed by the leached Cu ions in solution in comparison to that of Cu@Fabric. Reaction conditions: Cu@Fabric (0.5 cm × 0.5 cm containing 540 ppm equivalent of Cu ions), 0.2 mM TMB and, 10 mM H_2O_2 in 50 mM NaAc buffer (pH 5) at 37 °C.*

Similar to other NanoZymes [11, 12, 14, 16-18, 21, 22, 36, 46], the catalytic activity of the Cu@Fabric showed a NanoZyme-concentration, pH- and temperature-dependent trend. An increase in the catalytic activity was observed as a function of Cu concentration (**Figure 3.5**a). The concentration of Cu was modulated by changing the size of the fabric. The catalytic activity was found to increase as a function of Cu concentration. In fact, the concentration of the diimine derivative significantly improves with increase in the Cu concentration. For instance, when the Cu concentration changed from 540 ppm (0.5 cm × 0.5 cm) to 1430 ppm (0.5 cm × 1 cm) a ~10 times increase in the signature for the diimine derivative was observed. The pH-dependent activity profile showed that the Cu@Fabric was typically active in slightly acidic pH (4 and 5) with maximum activity at pH 5.0 (**Figure 3.5**b). Following pH 5.0, the activity decreases significantly, as is the case with several other NanoZymes [11-15]. Similar to the concentration-dependent trend, increasing the reaction

temperature resulted in faster catalytic activity (**Figure 3.5**c) where the concentration of the diimine derivative was the highest at 60 °C. Considering these observations, it is clear that the Cu@Fabric possess outstanding catalytic activity, while the ability to easily extract the NanoZyme post-reaction or as and when needed provides the capacity to attain superior control over the reaction kinetics. Such templated NanoZymes can therefore be termed as '*free-standing*' catalysts.

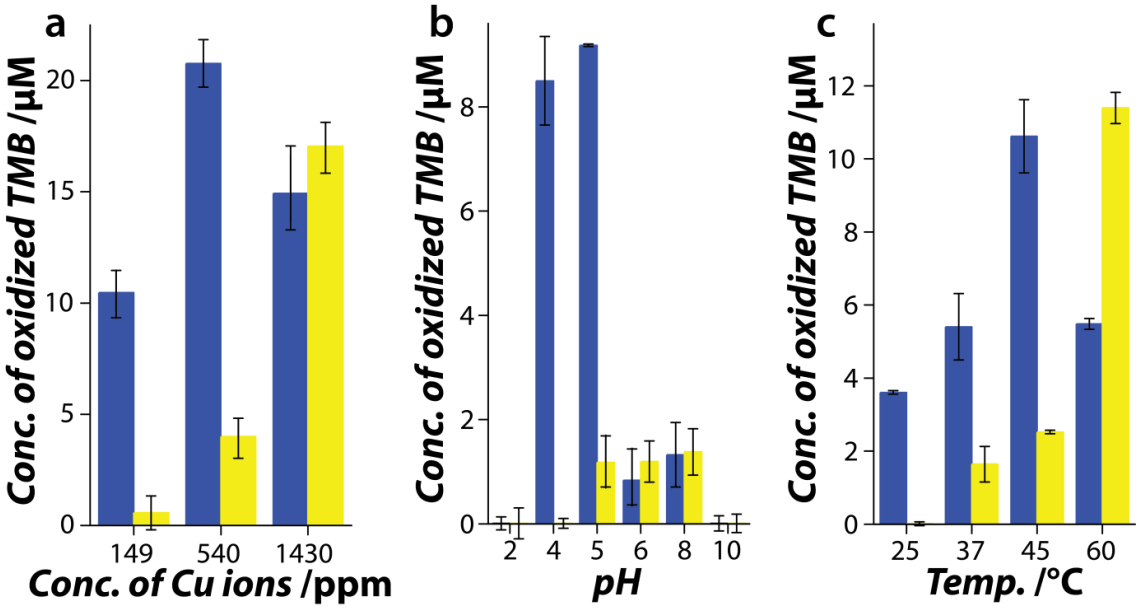

Figure 3.5 *Effect of* ***(a)*** *Cu nanoparticle concentration (Cu ions equivalent);* ***(b)*** *pH; and* ***(c)*** *temperature on the peroxidase-mimic activity of Cu@Fabric. The different colored bars represent the oxidised TMB products (blue bars indicate the charge transfer complex measured at* λ_{max} *= 652 nm, and the yellow bars indicate the diimine derivative measured at* λ_{max} *= 450 nm).*

3.3.3 Mechanism of peroxidase-like activity of free-standing Cu@Fabric NanoZyme

While NanoZymes show enzyme-mimicking behavior, the underlying mechanism through which NanoZymes oxidise colorless peroxidase substrates to their corresponding colored product can be attributed to the formation of hydroxyl radical (•OH) generation [16, 19]. The

earlier work on Ag@Fabric as NanoZyme showed that the mechanism of the catalytic oxidation involves the generation of •OH radicals [19]. In order to understand if a similar mechanism occurs in the current case, terephthalic acid (TA) was used as a capture probe for •OH radicals that will be generated during the decomposition of H_2O_2 by the Cu@Fabric. TA, a non-fluorescent molecule, reacts with •OH radicals to generate 2-hydroxyterephthalic acid, which is a fluorescent molecule [20]. Based on the intensity of the fluorescence signal at 435 nm (excitation = 315 nm), the amount of •OH radicals generated by the Cu@Fabric can be determined.

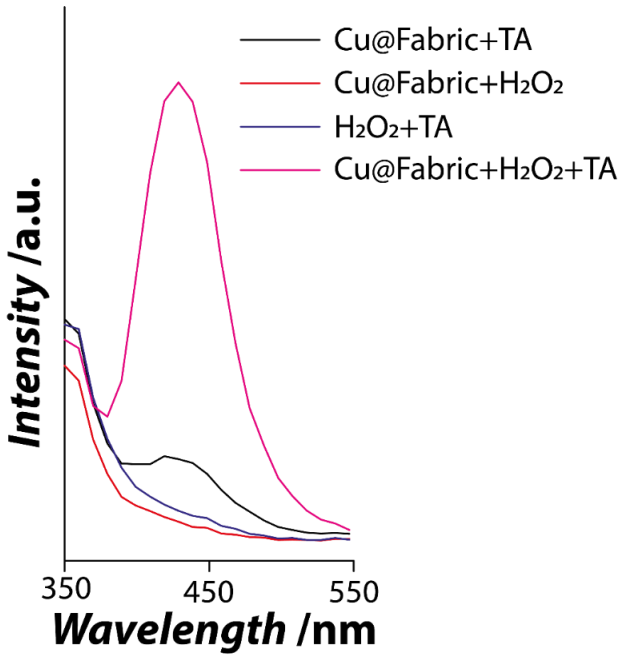

Figure 3.6 *Fluorescence emission spectra of terephthalic acid under different reaction conditions recorded at an excitation wavelength of 315 nm. Reaction conditions: Cu@Fabric (0.5 cm × 0.5 cm containing 540 ppm equivalent of Cu ions), 1 mM TA and, 10 mM H_2O_2 in 50 mM NaAc buffer (pH 5) at 37 °C.*

As shown in **Figure 3.6**, the fluorescence intensity was significantly higher when the reaction contained the Cu@Fabric and H_2O_2, while minimal fluorescence response was observed in all other control experiments. This suggests that the catalytic activity of the Cu@Fabric results in the breaking of O-O bond in H_2O_2 generating the •OH radicals [66].

3.3.4 Steady-state kinetic parameters for the Cu@Fabric NanoZyme

Based on the high catalytic ability of the Cu@Fabric and for its applicability in developing a colorimetric sensor for glucose, it was important to determine the apparent steady-state kinetic parameters such as Michaelis-Menten constant (K_m) and maximum initial velocity of the reaction (V_{max}). For this, the activity of the Cu@Fabric was investigated by varying the concentration of the substrates TMB and H_2O_2, independently. In both cases, typical Michaelis-Menten curves were observed (**Figure 3.7**) which allowed to calculate the K_m and V_{max}.

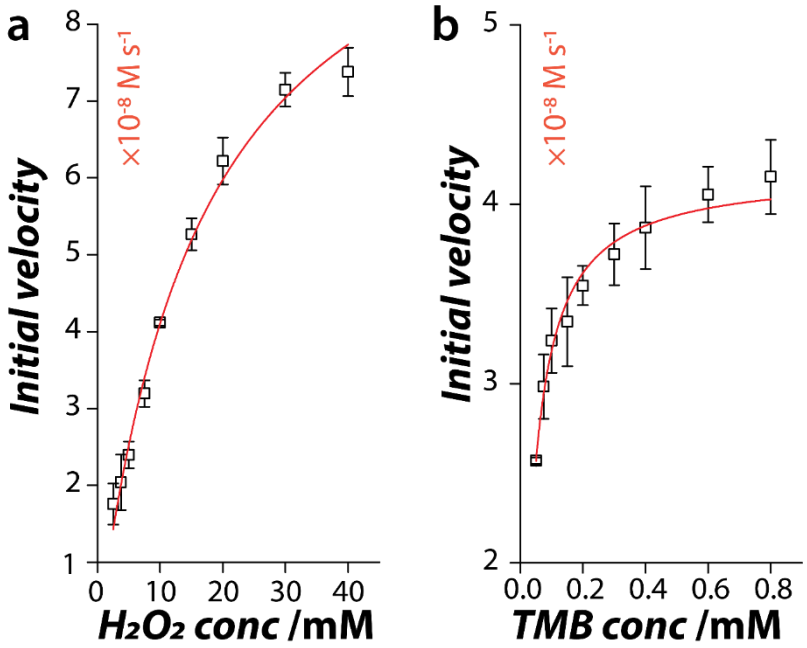

Figure 3.7 *Steady-state kinetic analysis using Michaelis-Menten fit of the colorimetric response for Cu@Fabric NanoZyme by varying* ***(a)*** *H_2O_2 concentration at constant TMB concentration (0.2 mM), and* ***(b)*** *TMB concentration at a constant H_2O_2 concentration (10 mM).*

In NanoZymes, K_m is the measure of the affinity of the NanoZyme to the substrate, while V_{max} provides information on the catalytic rate [65]. As shown in **Table 3.1**, the K_m for H_2O_2 was significantly higher than that obtained for TMB suggesting that the affinity of the

Cu@Fabric to H_2O_2 is a limiting factor. On the other hand, the high V_{max} for both TMB and H_2O_2 meant that the reaction can proceed rapidly.

Table 3.1 *Comparison of the apparent Michaelis-Menten constant (K_m) and maximum rate of reaction (V_{max}) for metal NanoZymes, natural peroxidase enzyme, and free-standing Cu@Fabric NanoZyme.*

Catalyst	**TMB**		**H_2O_2**	
	K_m / mM	**V_{max} / 10^{-8} Ms^{-1}**	**K_m / mM**	**V_{max} / 10^{-8} Ms^{-1}**
Free-standing Ag@Fabric [19]	0.19	15.10	7.61	14.40
Au NCs [30]	3.59	0.86	16.71	1.3
Au NPs [31]	0.011	8.3	33	6.1
Cu NCs [32]	0.648	5.96	29.16	4.22
Cu NPs [33]	1.047	3.97	31.26	26.4
CuO NRs [16]	0.06 (ABTS)	4.1 (ABTS)	14.8	0.6
Ir NPs [34]	0.03	1.7	18.02	8.1
$Gd(OH)_3$ [20]	3.28 (ABTS)	2.5 (ABTS)	16.11	9.1
Pd NPs [35]	0.109	5.82	4.39	6.51
Pt NCs [29]	0.096	14.14	3.07	18.17
Pt NPs [26]	0.12	126	769	185
Rh NPs [27]	0.198	6.78	0.38	24.1
Ru NPs [28]	0.234	8.25	2.206	58.26
Horseradish peroxidase [38]	0.43	10.0	3.70	8.71
Free-standing Cu@Fabric	0.03	4.19	16.65	10.95

This further outlines the importance of using cotton fabric as a template where due to the high wettability and absorbency of the cotton fabric [55], it allows the reactants to come in close vicinity of the active catalyst thereby promoting higher catalytic efficiency.

3.3.5 Glucose sensing in urine using free-standing Cu@Fabric NanoZyme to generate a colorimetric response

Glucose oxidase (GOx) catalyses the oxidation of its substrate glucose to gluconolactone and hydrogen peroxide [51]. Therefore H_2O_2, the intermediate product, can be used to quantify glucose using a peroxidase assay – where HRP enzyme is used for the generation of sensor response [3]. Given the unstable nature of HRP to H_2O_2 (inactivation of enzyme), the cost associated with its synthesis and purification and, poor stability in harsh conditions, NanoZymes have been proposed as a viable alternative in place of HRP for detection [14]. Another challenge in detecting glucose in urine is that the concentration of glucose in urine is typically much higher than in blood [4]. When using NanoZymes to detect glucose in urine, the sample needs to be diluted to bring the glucose concentration within the linear dynamic range (typically µM) of the sensor operation [13, 46]. One strategy to circumvent this issue is to increase the concentration of the NanoZyme to push the operating range to the high µM level [19]. While this may be successful, there are a few concerns *viz*. (i) high concentration of nanoparticles will result in scattering or surface plasmon resonance (SPR) effect – lead to high background signal compromising sensitivity or interference with color generated due to substrate oxidation (red color of the gold nanoparticles can interfere with the blue colored product of TMB oxidation); (ii) aggregation of nanoparticles in complex sample such as urine – NanoZyme activity is not influenced by aggregation and (iii) formation of biological corona on the nanoparticle surface. In a previous work, by incorporating Ag nanoparticles on cotton fabric, the linear dynamic range was pushed to the low mM level (due to increased concentration of Ag NanoZyme), while using cotton fabric as a template increased the kinetics of the reaction (absorbent property brings target in close vicinity of NanoZyme) to negate the formation of biological corona within the timeframe of the sensing event [19, 67]. In the current case, the outstanding catalytic ability of copper nanoparticles should, in

principle, allows to significantly extend the linear operating dynamic range of the sensor, while the high loading of the active catalyst will improve reaction velocity.

First the ability of peroxidase-mimic Cu@Fabric NanoZyme (in conjunction with GOx) to quantify glucose was established by exposing the sensor to a series of glucose concentrations ranging from 0 to 20 mM. A key difference in this system in comparison to other NanoZyme systems is that, typically, glucose incubation with GOx is carried out at neutral pH followed by changing the reaction to acidic conditions (pH 5 or lower) for optimum NanoZyme activity [19, 46, 47]. In the current case, both the incubation of glucose with GOx and NanoZyme activity was carried out at pH 5. This is because, the optimal condition for the catalytic activity of GOx (from *Aspergillus niger*) is pH 5 [68], while the same pH is the optimal condition to achieve high NanoZyme activity.

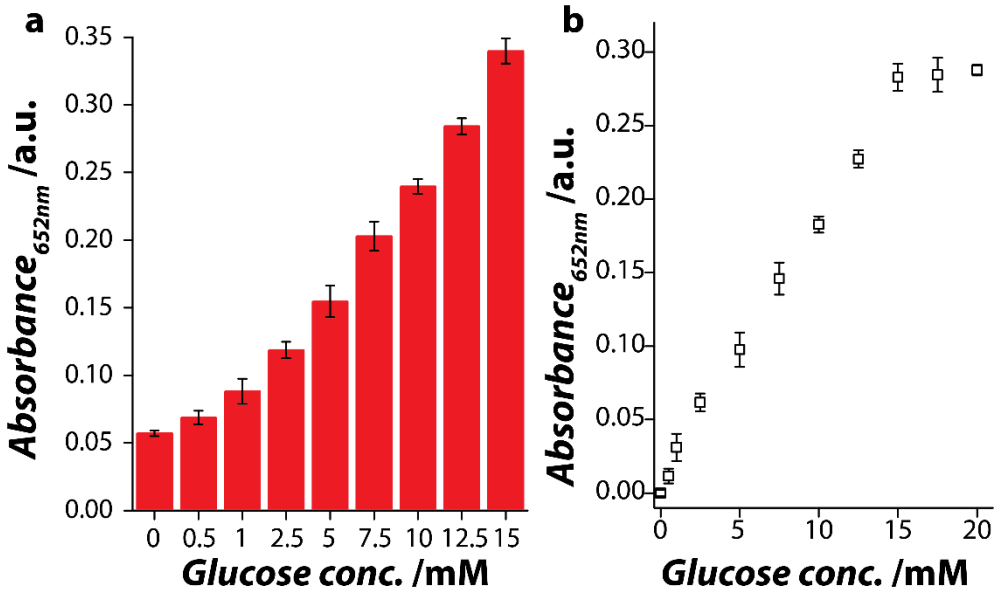

Figure 3.8 (a) *Raw absorbance values obtained as a result of TMB oxidation by Cu@Fabric when exposed to different concentrations of glucose that were used for the linear calibration plot shown in Figure 3.9(a).* ***(b)*** *Colorimetric response of TMB oxidised by Cu@Fabric NanoZyme when exposed to different concentrations of glucose (0.5 mM – 20 mM) where the response saturates when exposed to higher glucose concentrations.*

The sensor response showed a linear relationship for glucose concentrations ranging from 0.5 to 15 mM (**Figure 3.9**a and **Figure 3.8**a showing the response before normalization), beyond which the sensor response saturated (**Figure 3.8**b). Such a broad linear dynamic range will allow glucose detection in urine samples with minimal or no dilution. The limit of detection (LoD) was calculated to be 0.45 mM. The precision and accuracy of the sensor were determined by exposing the sensor to 1 mM glucose concentration 15 times independently leading to a precision of 96.8% and an accuracy of 100% at 10% confidence (93.3% at 5% confidence).

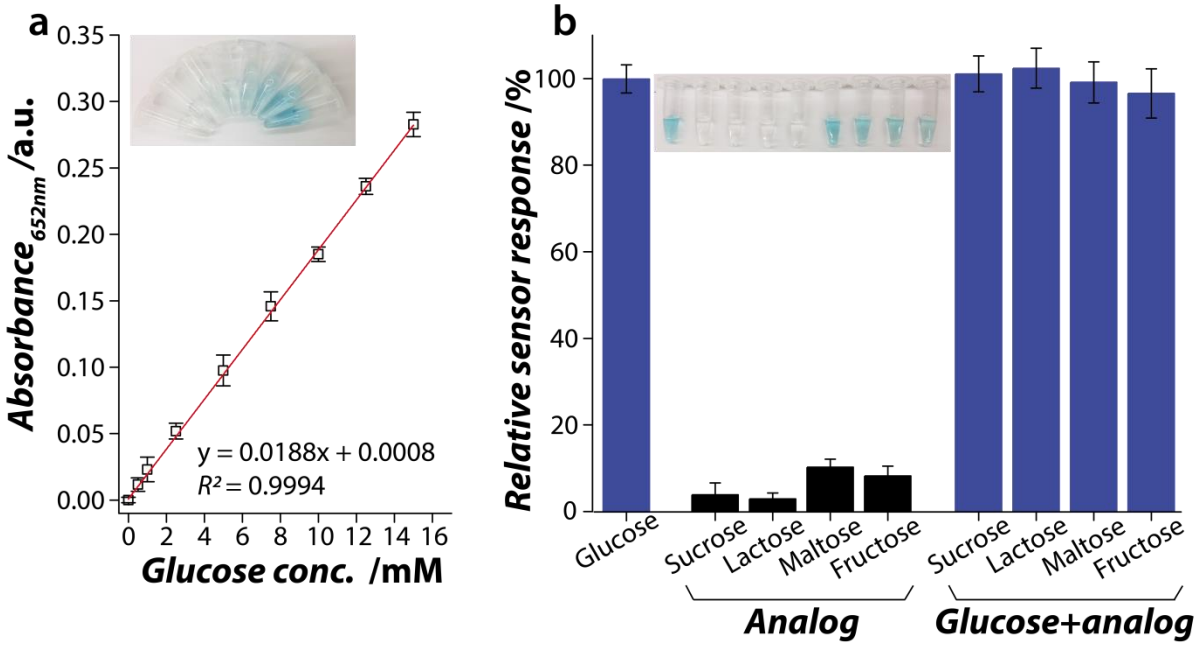

Figure 3.9 *Sensor performance to detect glucose.* ***(a)*** *Linear calibration plot obtained using Cu@Fabric NanoZyme system for a range of glucose concentrations. Inset shows the corresponding optical image;* ***(b)*** *Selectivity of the sensor to detect glucose either in the presence of glucose analogues independently or in combination with glucose. Inset shows the corresponding optical image.*

Specificity was established by monitoring the ability of the sensor to generate a colorimetric response after exposing the sensor to glucose analogues sucrose, lactose, maltose and fructose. Under the same experimental conditions, the sensor only generates a

colorimetric response in the presence of glucose while showing basal level activity (<10%) when exposed to glucose analogues at 10 mM concentration (**Figure 3.9**b). Further, the sensor was exposed to glucose analogues that contained a fixed concentration of glucose (5 mM). There was no significant variability (< 4% variation) in the color generation even in the presence of analogue molecules outlining the robustness of the newly developed colorimetric NanoZyme sensor for glucose sensing.

Having established the working of the sensor, the practical feasibility of the sensor performance was further validated for the detection of glucose in human urine samples. Monitoring of glucose in urine is specially important in patients with poor glucose control that can lead to hyperglucuria where glucose is present in high concentrations in the urine as glucose reaches above the renal threshold of kidneys (0 and 0.8 mM concentration in healthy patients) and in patients with renal complications such as Fanconi syndrome [4]. Glucose concentrations in the urine sample was quantified using three independent approaches *viz*. (i) laboratory gold standard – GOx-HRP system; (ii) a commercial urine sugar test strip (Diastix by Bayer) and (iii) the Cu@Fabric NanoZyme sensing system. The glucose concentration in the urine sample obtained from a healthy volunteer was first quantified using the GOx-HRP system. Given that the gold standard did not result in an oxidised product, it was assumed that the healthy volunteer had 0 mM concentration of glucose. The effectiveness of the developed NanoZyme platform was then established by spiking known concentrations (1, 2.5, 5, 7.5 and 10 mM) of glucose in the urine obtained from the healthy volunteer. **Table 3.2** shows the expected and the estimated glucose concentration obtained using the GOx-HRP system and the Cu@Fabric NanoZyme sensing system. It is important to note that the commercial urine sugar test strip was not used for this assay as it provides an indication of glucose when the concentration is either 0, 5.5, 14, 28 mM or above. A recovery of 97-102% with a low standard deviation (SD) was obtained for the tested concentrations both in the case of GOx-

HRP and the NanoZyme system showing that the current platform is as robust as the gold standard.

Table 3.2 *Comparison of the results from glucose analysis in urine sample obtained from a healthy volunteer after spiking known concentrations of glucose using glucose oxidase-horseradish peroxidase (GOx-HRP) method and Cu@Fabric NanoZyme method. The values in brackets are the corresponding standard deviation.*

Original amount (mM)[a]	**Glucose spiked (mM)**	**Expected (mM)**	**GOx-HRP approach**		**Cu@Fabric NanoZyme approach**	
			Est. glucose conc. /mM[b]	**Recovery (%)**[c]	**Est. glucose conc. /mM**[b]	**Recovery (%)**[c]
Undetectable (0 mM)[a]	0	0.0	0.00 (0.00)	100	0.00 (0.00)	100
	1	1.0	1.01 (0.04)	97-105	0.97 (0.06)	91-103
	2.5	2.5	2.49 (0.06)	97-102	2.47 (0.1)	95-102
	5	5.0	5.04 (0.19)	97-104	5.21 (0.14)	101-107
	7.5	7.5	7.49 (0.20)	97-102	7.4 (0.11)	97-100
	10	10.0	10.04 (0.22)	98-102	9.93 (0.18)	97-101

[a] Original amount of glucose calculated from GOx-HRP gold standard method.
[b] Standard deviation calculated from 5 independent experiments.
[c] Recovery calculated using (Measured value / Expected value) × 100.

To further assess the practical applicability, urine samples from a diabetic volunteer (Type II diabetes) was also collected and analyzed using all three sensing approaches (**Table 3.3**). A glucose concentration of 15.1 ± 0.01 mM was estimated using the gold standard GOx-HRP system. In contrast, the commercial urine sticks showed a significantly high degree of variability with an estimate of 28 (185% recovery) when compared with the GOx-HRP approach. One possible reason for this high variability is that these strips are highly time-sensitive and can overestimate the amount of glucose even if the measurement is off by 10-15 seconds. Additionally, the strip only offers colors based on specific concentrations of glucose *i.e.* between 5.5 and 14 mM glucose the change in color cannot be quantified confidently. In contrast, the Cu@Fabric NanoZyme system estimated the glucose concentration to be 14.9 ± 0.16 mM with a recovery of 97.6-99.7% (when compared with GOx-HRP approach).

Table 3.3 *Comparison of glucose estimation in urine samples obtained from a healthy and diabetic volunteer using glucose oxidase-horseradish peroxidase (GOx-HRP), Cu@Fabric NanoZyme and commercially available Diastix urine sugar test strip method. The values in brackets are the corresponding standard deviation.*

Method	**GOx-HRP approach**	**Cu@Fabric NanoZyme approach**		**Diastix urine sugar test strips**	
	Est. glucose conc. /mM[a]	**Est. glucose conc. /mM**[a]	**Recovery (%)**[b]	**Est. glucose conc. /mM**[a]	**Recovery (%)**[b]
Healthy volunteer	0.00 (0.00)	0.00 (0.00)	100	0	100
Diabetic volunteer	15.1 (0.01)	14.9 (0.16)	97.6-99.7	28	185

[a] Standard deviation calculated from 5 independent experiments.
[b] Recovery calculated using (Measured value / GOx-HRP method value) × 100.

This shows that the newly developed NanoZyme system is on-par with the current gold standard. However, a particular advantage of this system was that the urine sample was not diluted to bring the concentration into the operating linear dynamic range.

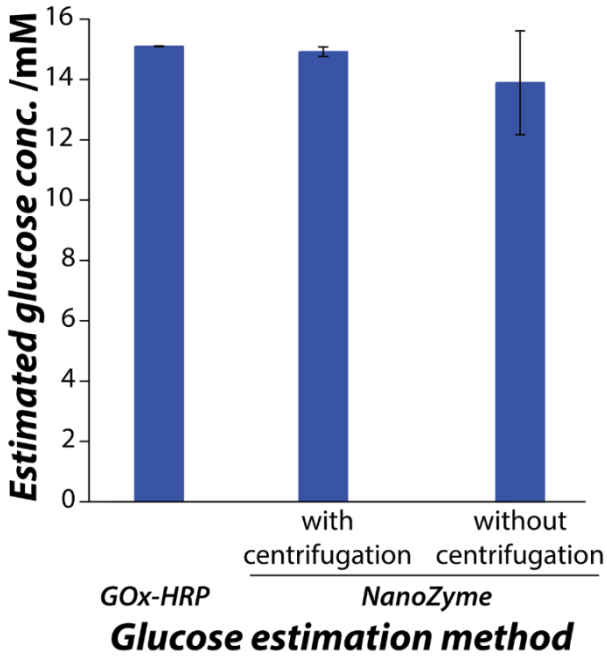

Figure 3.10 *Comparison of estimated glucose concentration in diabetic volunteer urine sample by different methods.*

To understand the influence of the biological matrix on the sensor performance, the urine sample was used with and without centrifugation to remove cells and other materials that may be present during collection. It is clear from **Figure 3.10** that when the urine sample was used without centrifugation, it results in a higher standard deviation. However, the estimation of glucose concentration was only 6-7% lower than that obtained from the sample that was centrifuged. This shows the outstanding robustness of the newly developed NanoZyme platform.

3.4 Conclusions

In this study, the outstanding ability of free-standing Cu@Fabric as a NanoZyme catalyst is established. The high catalytic activity can be attributed to the copper nanoparticles themselves, while high loading of nanoparticles on the fabric surface improves catalytic efficiency due to the highly porous and absorbent nature of the underlying cotton fabric and access to a large number of catalytic sites. The high catalytic efficiency was established by measuring the oxidation of TMB substrate where for the first time the formation of diimine derivative (yellow-colored product) at mildly acidic conditions was observed. This is unique as typically NanoZymes only promote TMB oxidation to form a blue colored charge-transfer complex. This catalytic NanoZyme activity was dependent on reaction conditions such as pH, temperature, substrate concentration, and NanoZyme concentration. This activity was then exploited to quantify glucose where the sensor showed an operating linear dynamic range of 0.5 – 15 mM, which is close to the biologically relevant concentrations. Further, the practical applicability of the NanoZyme sensor to quantify glucose in urine from healthy and diabetic volunteers is shown. The ability to accurately quantify glucose (recovery of >98%) in comparison to industry gold standard glucose oxidase/horseradish peroxidase system further outlines the robustness of the newly developed NanoZyme platform.

3.5 References

1. Narayan, K.V. and F. Fleck, *Bull World Health Organ*, 2016. **94**: 233-308.
2. Newman, J.D. and A.P. Turner, *Biosens. Bioelectron.*, 2005. **20**(12): 2435-2453.
3. Oliver, N., C. Toumazou, A. Cass, and D. Johnston, *Diabet. Med.*, 2009. **26**(3): 197-210.
4. Fine, J., *Br. Med. J.*, 1965. **1**(5444): 1209-1214.
5. Helen, L.S., M.H. van Pelt, S. Bun, F. Daily, T. Neogi, M. Thompson, H. McGuire, and B.H. Weigl, *BMJ open*, 2018. **8**(3): e019924.
6. Garcia, J., Y. Zhang, H. Taylor, O. Cespedes, M.E. Webb, and D. Zhou, *Nanoscale*, 2011. **3**(9): 3721-3730.
7. Sun, J., J. Ge, W. Liu, M. Lan, H. Zhang, P. Wang, Y. Wang, and Z. Niu, *Nanoscale*, 2014. **6**(1): 255-262.
8. Valderrama, B., M. Ayala, and R. Vazquez-Duhalt, *Chem. Biol.*, 2002. **9**(5): 555-565.
9. Nicell, J.A. and H. Wright, *Enzyme Microb. Technol.*, 1997. **21**(4): 302-310.
10. Kafi, A.K.M., G. Wu, and A. Chen, *Biosens. Bioelectron.*, 2008. **24**(4): 566-571.
11. Wei, H. and E. Wang, *Chem. Soc. Rev.*, 2013. **42**(14): 6060-6093.
12. Wu, J., X. Wang, Q. Wang, Z. Lou, S. Li, Y. Zhu, L. Qin, and H. Wei, *Chem. Soc. Rev.*, 2019. **48**(4): 1004-1076.
13. Wang, X., Y. Hu, and H. Wei, *Inorg. Chem. Front.*, 2016. **3**(1): 41-60.
14. Wang, Q., H. Wei, Z. Zhang, E. Wang, and S. Dong, *TrAC, Trends Anal. Chem.*, 2018. **105**: 218-224.
15. Lin, Y., J. Ren, and X. Qu, *Acc. Chem. Res.*, 2014. **47**(4): 1097-1105.
16. Karim, M.N., M. Singh, P. Weerathunge, P. Bian, R. Zheng, C. Dekiwadia, T. Ahmed, S. Walia, E. Della Gaspera, S. Singh, R. Ramanathan, and V. Bansal, *ACS Appl. Nano Mater.*, 2018. **1**(4): 1694-1704.
17. Weerathunge, P., R. Ramanathan, R. Shukla, T.K. Sharma, and V. Bansal, *Anal. Chem.*, 2014. **86**(24): 11937-11941.
18. Weerathunge, P., R. Ramanathan, V.A. Torok, K. Hodgson, Y. Xu, R. Goodacre, B.K. Behera, and V. Bansal, *Anal. Chem.*, 2019. **91**(5): 3270-3276.
19. Karim, M.N., S.R. Anderson, S. Singh, R. Ramanathan, and V. Bansal, *Biosens. Bioelectron.*, 2018. **110**: 8-15.
20. Singh, M., P. Weerathunge, P.D. Liyanage, E. Mayes, R. Ramanathan, and V. Bansal, *Langmuir*, 2017. **33**(38): 10006-10015.
21. Weerathunge, P., D. Pooja, M. Singh, H. Kulhari, E.L. Mayes, V. Bansal, and R. Ramanathan, *Sens. Actuators, B*, 2019: 126737.
22. Walther, R., A.K. Winther, A.S. Fruergaard, W. van den Akker, L. Sørensen, S.M. Nielsen, M.T. Jarlstad Olesen, Y. Dai, H.S. Jeppesen, P. Lamagni, A. Savateev, S.L. Pedersen, C.K. Frich, C. Vigier-Carrière, N. Lock, M. Singh, V. Bansal, R.L. Meyer, and A.N. Zelikin, *Angew. Chem. Int. Ed.*, 2019. **58**(1): 278-282.

23. Neri, S., S.G. Martin, C. Pezzato, and L.J. Prins, *J. Am. Chem. Soc.*, 2017. **139**(5): 1794-1997.

24. Zhang, Z., X. Zhang, B. Liu, and J. Liu, *J. Am. Chem. Soc.*, 2017. **139**(15): 5412-5419.

25. Wang, F., E. Ju, Y. Guan, J. Ren, and X. Qu, *Small*, 2017. **13**(25).

26. Gao, Z., M. Xu, L. Hou, G. Chen, and D. Tang, *Anal. Chim. Acta*, 2013. **776**: 79-86.

27. Choleva, T.G., V.A. Gatselou, G.Z. Tsogas, and D.L. Giokas, *Microchim. Acta*, 2018. **185**(1): 22.

28. Cao, G.-J., X. Jiang, H. Zhang, T.R. Croley, and J.-J. Yin, *RSC Adv.*, 2017. **7**(82): 52210-52217.

29. Jin, L., Z. Meng, Y. Zhang, S. Cai, Z. Zhang, C. Li, L. Shang, and Y. Shen, *ACS Appl. Mater. Interfaces*, 2017. **9**(11): 10027-10033.

30. Hu, L., H. Liao, L. Feng, M. Wang, and W. Fu, *Anal. Chem.*, 2018. **90**(10): 6247-6252.

31. Liu, Y., C. Wang, N. Cai, S. Long, and F. Yu, *J. Mater. Sci.*, 2014. **49**(20): 7143-7150.

32. Hu, L., Y. Yuan, L. Zhang, J. Zhao, S. Majeed, and G. Xu, *Anal. Chim. Acta*, 2013. **762**: 83-86.

33. Wang, N., B. Li, F. Qiao, J. Sun, H. Fan, and S. Ai, *J. Mater. Chem. B*, 2015. **3**(39): 7718-7723.

34. Cui, M., J. Zhou, Y. Zhao, and Q. Song, *Sens. Actuators, B*, 2017. **243**: 203-210.

35. Wei, J., X. Chen, S. Shi, S. Mo, and N. Zheng, *Nanoscale*, 2015. **7**(45): 19018-19026.

36. Kumar Sharma, T., R. Ramanathan, P. Weerathunge, M. Mohammadtaheri, H. Kumar Daima, R. Shukla, and V. Bansal, *Chem. Commun.*, 2014. **50**(100): 15856-15859.

37. Weerathunge, P., T.K. Sharma, R. Ramanathan, and V. Bansal, *CHAPTER 23 Nanozyme-Based Environmental Monitoring*, in *Advanced Environmental Analysis: Applications of Nanomaterials, Volume 2*. 2017, The Royal Society of Chemistry. 108-132.

38. Gao, L., J. Zhuang, L. Nie, J. Zhang, Y. Zhang, N. Gu, T. Wang, J. Feng, D. Yang, and S. Perrett, *Nat. Nanotechnol.*, 2007. **2**(9): 577.

39. Le, N.D.B., G. Yesilbag Tonga, R. Mout, S.T. Kim, M.E. Wille, S. Rana, K.A. Dunphy, D.J. Jerry, M. Yazdani, R. Ramanathan, C.M. Rotello, and V.M. Rotello, *J. Am. Chem. Soc.*, 2017. **139**(23): 8008-8012.

40. Kandjani, A.E., M. Mohammadtaheri, A. Thakkar, S.K. Bhargava, and V. Bansal, *J. Colloid Interface Sci.*, 2014. **436**: 251-257.

41. Ramanathan, R., S. Walia, A.E. Kandjani, S. Balendran, M. Mohammadtaheri, S.K. Bhargava, K. Kalantar-Zadeh, and V. Bansal, *Langmuir*, 2015. **31**(4): 1581-1587.

42. Sabri, Y.M., S.J. Ippolito, A.P. O'Mullane, J. Tardio, V. Bansal, and S.K. Bhargava, *Nanotechnology*, 2011. **22**(30): 305501.

43. Selvakannan, P., R. Ramanathan, B.J. Plowman, Y.M. Sabri, H.K. Daima, A.P. O'Mullane, V. Bansal, and S.K. Bhargava, *Phys. Chem. Chem. Phys.*, 2013. **15**(31): 12920-12929.

44. Ramanathan, R., A.E. Kandjani, S. Walia, S. Balendhran, S.K. Bhargava, K. Kalantar-zadeh, and V. Bansal, *RSC Adv.*, 2013. **3**(39): 17654-17658.

45. Sabri, Y.M., S.J. Ippolito, J. Tardio, V. Bansal, A.P. O'mullane, and S.K. Bhargava, *Sci. Rep.*, 2014. **4**: 6741.

46. Su, L., J. Feng, X. Zhou, C. Ren, H. Li, and X. Chen, *Anal. Chem.*, 2012. **84**(13): 5753-5758.

47. Su, L., W. Qin, H. Zhang, Z.U. Rahman, C. Ren, S. Ma, and X. Chen, *Biosens. Bioelectron.*, 2015. **63**: 384-391.

48. Liu, B., Z. Sun, P.J.J. Huang, and J. Liu, *J. Am. Chem. Soc.*, 2015. **137**(3): 1290-1295.

49. Wang, Q., X. Zhang, L. Huang, Z. Zhang, and S. Dong, *ACS Appl. Mater. Interfaces*, 2017. **9**(8): 7465-7471.

50. Han, L., C. Li, T. Zhang, Q. Lang, and A. Liu, *ACS Appl. Mater. Interfaces*, 2015. **7**(26): 14463-14470.

51. Wei, H. and E. Wang, *Anal. Chem.*, 2008. **80**(6): 2250-2254.

52. Agasti, S.S., S. Rana, M.H. Park, C.K. Kim, C.C. You, and V.M. Rotello, *Adv. Drug Deliv. Rev.*, 2010. **62**(3): 316-328.

53. Hu, M., J. Chen, Z.Y. Li, L. Au, G.V. Hartland, X. Li, M. Marquez, and Y. Xia, *Chem. Soc. Rev.*, 2006. **35**(11): 1084-1094.

54. Sepúlveda, B., P.C. Angelomé, L.M. Lechuga, and L.M. Liz-Marzán, *Nano Today*, 2009. **4**(3): 244-251.

55. Anderson, S.R., M. Mohammadtaheri, D. Kumar, A.P. O'Mullane, M.R. Field, R. Ramanathan, and V. Bansal, *Adv. Mater. Interfaces*, 2016. **3**(6): 1500632.

56. Anderson, S.R., A.P. O'Mullane, E. Della Gaspera, R. Ramanathan, and V. Bansal, *Adv. Mater. Interfaces*, 2019. **6**(16): 1900516.

57. Mohammadtaheri, M., R. Ramanathan, S. Walia, T. Ahmed, P. Weerathunge, S.R. Anderson, M.R. Field, C.D. Dekiwadia, A.P. O'Mullane, and E. Della Gaspera, *Appl. Mater. Today*, 2018. **13**: 107-115.

58. Mohammadtaheri, M., R. Ramanathan, and V. Bansal, *Catal. Today*, 2016. **278**: 319-329.

59. Ramanathan, R., M.R. Field, A.P. O'Mullane, P.M. Smooker, S.K. Bhargava, and V. Bansal, *Nanoscale*, 2013. **5**(6): 2300-2306.

60. Bindra, P. and J.R. White, *Fundamental aspects of electroless copper plating*, in *Electroless Plating Fundamentals & Applications*. 1990. 289-375.

61. Bally, R.a. and T. Gribnau, *Clin. Chem. Lab. Med.*, 1989. **27**(10): 791-796.

62. Josephy, P.D., T. Eling, and R.P. Mason, *J. Biol. Chem*, 1982. **257**(7): 3669-3675.

63. Jia, C.-P., X.-Q. Zhong, B. Hua, M.-Y. Liu, F.-X. Jing, X.-H. Lou, S.-H. Yao, J.-Q. Xiang, Q.-H. Jin, and J.-L. Zhao, *Biosens. Bioelectron.*, 2009. **24**(9): 2836-2841.

64. Singh, S., P. Tripathi, N. Kumar, and S. Nara, *Biosens. Bioelectron.*, 2017. **92**: 280-286.

65. Jiang, B., D. Duan, L. Gao, M. Zhou, K. Fan, Y. Tang, J. Xi, Y. Bi, Z. Tong, and G.F. Gao, *Nat. Protoc.*, 2018. **13**(7): 1506.

66. Plauck, A., E.E. Stangland, J.A. Dumesic, and M. Mavrikakis. Active sites and mechanisms for H2O2 decomposition over Pd catalysts. in *Proc. Natl. Acad. Sci. USA*. 2016.

67. Carnovale, C., G. Bryant, R. Shukla, and V. Bansal, *Prog. Mater. Sci.*, 2016. **83**: 152-190.

68. Weibel, M.K. and H.J. Bright, *J. Biol. Chem*, 1971. **246**(9): 2734-2744.

CHAPTER 4

Galvanic replacement mediated synthesis of peroxidase-mimicking bimetallic nanoparticles as free-standing NanoZyme catalysts for the colorimetric detection of glucose in urine

In this chapter, a simple method of galvanic replacement reaction for the synthesis of bimetallic nanoparticles on a 3D matrix of cotton fabric is described. Cu nanoparticles deposited on cotton fabric act as a sacrificial template. When the Cu@Fabric is exposed to metal ions of gold, silver, platinum, and palladium, it undergoes spontaneous electroless galvanic replacement reaction to form bimetallic Cu-M@Fabrics (M = Au, Ag, Pt or Pd). The evaluation of their intrinsic peroxidase-mimicking catalytic activity (NanoZyme) revealed that the bimetallic systems possessed higher catalytic activity in comparison to Cu@Fabric as a catalyst. In all cases, the free-standing NanoZyme oxidises the peroxidase substrate TMB to its second oxidation product, a phenomenon not observed in reported NanoZymes. Comparing the NanoZyme activity of the different Cu-M@Fabrics showed that the Cu-Pt@Fabric possessed the highest catalytic efficiency. The high catalytic activity allowed the Cu-Pt@Fabric to produce an intense colorimetric response to detect glucose in urine samples, while also improving the stability of the catalyst.

4.1 Introduction

Given the fact that natural enzymes have poor ambient stability and have a high cost for production, there is a need to discover alternatives to natural enzymes (or artificial enzymes) [1, 2]. With increasing interest in functional nanomaterials, a new class of materials that possess intrinsic enzyme-mimic activity called *NanoZymes* are of particular interest [3, 4]. The inorganic nature of such catalysts provides unique properties such as high stability, low production cost, and high catalytic activity [3]. The possibility to fine-tune the catalytic properties of NanoZymes by controlling their size [5, 6] shape and morphology [7-9], forming hybrids [10-12], attaching recognition moieties [13-15], or by using external stimuli such as light [16-18] and pH [19, 20] make them excellent candidates to act as a viable alternative to natural enzymes. NanoZymes have wide range of applicability including biosensing [1-4, 21-23], antibacterial [16, 24, 25], pro-drug therapy [26], and environmental applications [13-15, 27, 28].

Much of the research in the field of NanoZymes has focused on metal nanoparticles. In contrast, bimetallic structures and their composites have received significant interest as the properties of the metal nanoparticle may be altered or improved by the addition of another due to the synergistic effect of the two metals [29]. In particular, such bimetallic structures have shown high potential in catalysis and sensing applications. Such bimetallic nanostructures can be realized by a number of approaches such as microwave [30, 31], thermal decomposition [29], co-reduction [29, 32], seeded growth [33, 34], and galvanic replacement [35-39]. Among them, a galvanic replacement reaction is a simple approach for the fabrication of bimetallic nanostructures where the composition of the final material can be easily controlled by moderating the concentration of the metal ions. A typical galvanic replacement reaction involves an atomic exchange between a sacrificial metal template and

metal ions in solution. This reaction does not involve any external potential to be applied but is rather sustained by the difference in the standard reduction potential between the sacrificial metal and the metal ions [39, 40]. As one metal gets deposited (reduced), there is a concomitant dissolution of the less noble metal (oxidises) during the reaction [41]. Bimetallic surfaces of choice such as dendritic, hollow, porous, *etc*., can be created by controlling the reaction parameters such as reaction medium, template morphology, the oxidation state of metal ions, *etc*., [35, 38, 42, 43]. Therefore, there is a strong focus on using this facile electroless approach for bimetallic nanostructure fabrication.

Copper nanoparticles are promising NanoZymes due to their high catalytic activity and economic viability [16, 44-46]. However, it is susceptible to surface oxidation in air, which could, in turn, affect catalyst activity and reuse [47, 48]. On the other hand, noble metals such as silver, gold, platinum, and palladium have long been known for their excellent enzyme-mimicking activity [3, 4, 49]. Fabrication of bimetallic nanostructures with copper as the sacrificial template is of significant interest as this could not only prevent the oxidation of copper but may also improve the overall catalytic activity due to a synergistic effect [36]. The fact that the reduction potential of $Cu^{2+/0}$ couple is lower when compared to noble metals such as Ag, Au, Pt, and Pd makes them excellent candidates to participate in galvanic replacement reactions for the fabrication of Cu-Ag, Cu-Au, Cu-Pt, and Cu-Pd hybrids [50]. To this end, several enzyme-mimicking bimetallic nanostructures have been reported [10, 12, 51-53]. For example, Han *et al* reported that Au@Ag nanorods exhibit high peroxidase-mimicking activity at near-neutral pH as opposed to commonly reported NanoZymes are effective in acidic pH [53]. Wu *et al* rationally tuned the concentration of Pt in Au@Pt nanoparticles to simultaneously exhibit plasmonic and enzyme-mimicking activities [54]. However, in most cases, due to the use of colloidal NanoZymes, the recovery post-reaction and the detection of a high concentration of the analyte remains a challenge [21]. This issue

can be overcome by depositing the catalyst on three-dimensional (3D) templates. One such template that has shown promise is cotton textiles/buds. It has been shown that cotton templates provide hierarchical structuring, absorbency, and porosity [21, 36, 47, 55-57] that can lead to enhanced catalytic properties [58, 59] or better sensing ability [55, 56].

In the current work, to improve the catalytic properties of Cu@Fabric (outlined in Chapter 3), a range of bimetallic Cu-Au@Fabric, Cu-Ag@Fabric, Cu-Pt@Fabric, and Cu-Pd@Fabric (referred to as Cu-M@Fabric where M is Au, Ag, Pt, or Pd metal) was fabricated by reacting the Cu@Fabric with metal ions of Au, Ag, Pt, and Pt. The peroxidase-mimicking catalytic activity of these Cu-M@Fabrics was established where Cu-Pt@Fabric showed superior catalytic efficiency. Combining the highly catalytic Cu with Pt, which is also known to possess high catalytic activity improved the detection of glucose in urine samples.

4.2 Materials and methods

4.2.1 Materials and reagents

Tin(II) chloride ($SnCl_2$), palladium(II) nitrate ($Pd(NO_3)_2$), sodium hydroxide (NaOH), potassium sodium tartrate tetrahydrate ($C_4H_4KNaO_6.4H_2O$), copper sulfate pentahydrate ($CuSO_4.5H_2O$), formaldehyde (CH_2O, 36.5-38% in H_2O), gold(III) chloride ($HAuCl_4$), silver nitrate ($AgNO_3$), chloroplatinic acid (H_2Cl_6Pt), palladium(II) chloride (Cl_2Pd), 3,3′,5,5′-tetramethylbenzidine (TMB), 2,2′-azino-bis(3-ethylbenzothiazoline-6-sulphonic acid) (ABTS), o-phenylenediamine dihydrochloride (OPD), sodium acetate anhydrous ($C_2H_3NaO_2$), acetic acid (CH_3COOH), terephthalic acid (TA), glucose ($C_6H_{12}O_6$), glucose oxidase (GOx from *Aspergillus niger*), horseradish peroxidase (HRP), sucrose ($C_{12}H_{22}O_{11}$), fructose ($C_6H_{12}O_6$), lactose ($C_{12}H_{22}O_{11}$), maltose ($C_{12}H_{22}O_{11}$) were purchased from Sigma-Aldrich, Australia. Hydrogen peroxide (H_2O_2, 30% w/w) was purchased from Chem-Supply

Pty Ltd. Cotton fabric was bought from the local market. Milli-Q water (18.2 MΩ cm) was obtained from a Millipore Milli-Q water purification system.

4.2.2 Synthesis of Cu-M@Fabrics (M = Au, Ag, Pt, or Pd)

The Cu@Fabric was synthesized as detailed in Chapter 3 [47]. In brief, 80 pieces of 0.5 cm × 0.5 cm cotton fabric were first sensitized in an acidic $SnCl_2$ solution (3.0 mM) for 1 hour; followed by exposure to aqueous $Pd(NO_3)_2$ (3.0 mM) for 30 minutes for the formation of Pd^0 nuclei that act as seeds for copper deposition [36, 47]. The Pd^0 coated fabrics were then exposed to a solution mixture containing NaOH (1 M), potassium sodium tartrate (0.3 M), copper(II) sulfate (0.1 M) and formaldehyde (0.5 M) for 5 hours at 55°C resulting in the formation of Cu nanoparticles on cotton fabric. The resulting Cu@Fabrics were washed with Milli-Q water to remove any free metal ions. The Cu-M@Fabrics were synthesized as outlined in the previous chapter [36]. 20 pc of 0.5 cm × 0.5 cm Cu@Fabrics were exposed to 50 mL aqueous solution of 1 mM $HAuCl_4$, $AgNO_3$, H_2PtCl_6, or $PdCl_2$ for 1 hour at room temperature. Followed by washing the material three times with Milli-Q water to remove excess metal ions.

4.2.3 Characterization of Cu-M@Fabrics

The Cu-M@Fabrics were imaged using scanning electron microscopy (SEM) by first attaching the sample on an aluminum stub followed by analysis using the FEI Verios SEM instrument (operated at an accelerating voltage of 30 kV). Energy dispersive X-ray (EDX) spectroscopic analysis and mapping were performed on the same instrument with an additional fitting of the Oxford X-Max 20 Silicon Drift Detector. X-ray photoelectron spectroscopy (XPS) measurements were performed on the Thermo K-Alpha XPS instrument (Al Kα radiation, photon energy of 1486.6 eV) [48]. The C 1s, O 1s, Cu 2p, Au 4f, Ag 3d, Pd 3d, and Pt 4f core level spectra for the samples were collected followed by background

correction using Shirley algorithm. Chemically distinct species were resolved using a nonlinear least squares fitting procedure and aligned with adventitious carbon binding energy of 285 eV. The concentration of the total metal deposited on the fabric surface was determined by quantifying the metal ion concentration using atomic emission spectroscopy using an Agilent Technologies 4200 Microwave Plasma AES instrument.

4.2.4 Peroxidase-mimicking NanoZyme activity of Cu-M@Fabrics

The peroxidase-mimicking activity of the Cu-M@Fabrics was assessed by testing its ability to oxidise peroxidase substrate – TMB to its colored product in the presence of H_2O_2. The reaction system involved 50 mM NaAc buffer (pH 5), 0.2 mM TMB, 10 mM H_2O_2 and Cu-M@Fabric (0.5 cm × 0.5 cm) incubated at 37 °C. The reaction was monitored as a function of time and the fabrics were extracted from the reaction before every UV-vis spectroscopic measurements on the CLARIOstar plate reader (BMG Labtech). A similar reaction with Cu@Fabric was carried out to compare the enhancement or detraction in the enzyme-mimicking activity of the bimetallic systems (Cu-M@Fabric).

4.2.5 Standardization of peroxidase-mimicking assay parameters for Cu-Pt@Fabrics

Among the four synthesized bimetallic nanoparticles, one of them ie., Cu-Pt@Fabric was chosen for further studies leading to the development of a glucose sensor. The substrate specificity of Cu-Pt@Fabric NanoZyme was assessed by exposing the NanoZyme to OPD or ABTS in place of TMB. The reaction involved 50 mM NaAc buffer (pH 5), 0.2 mM OPD or ABTS, 10 mM H_2O_2 and Cu-Pt@Fabric (0.5 cm × 0.5 cm). Their oxidation products were quantified using spectroscopic measurements done on the CLARIOstar plate reader (BMG Labtech). The intrinsic peroxidase-mimic activity of the Cu-Pt@Fabric was determined by testing the activity of potentially leached metal ions in solution. Cu-Pt@Fabric was incubated

in 50 mM NaAc buffer (pH 5) for 20 min at 37 °C. The buffer solution containing the potential leached ions was then used as catalyst to oxidise 0.2 mM TMB in the presence of 10 mM H_2O_2. Further, reaction conditions in terms of the Cu-Pt@Fabric NanoZyme concentration, buffer pH, and reaction temperature were optimized. The total weight of the Cu-Pt@Fabric NanoZyme that catalyses the peroxidase-mimicking reaction was varied from 0.8 mg to 3 mg while other reaction conditions were kept constant. The pH and temperature conditions of the reaction were varied from pH 2 – 10 and 25 – 60 °C, respectively; where other reaction parameters were kept consistent. Steady-state kinetic parameters were determined by maintaining a fixed concentration of Cu/Pt while independently varying H_2O_2 and TMB concentration between 2.5 – 40 mM and 0.05 – 0.8 mM, respectively. The colorimetric response was fitted to Lineweaver-Burk plot using OriginPro 2016 and enzyme-kinetic parameters – Michaelis-Menten constant (K_m) and maximum reaction velocity (V_{max}) were calculated using **Equation 4.1**.

$$\frac{1}{V_0} = \frac{K_m}{V_{max}}\left(\frac{1}{[S]} + \frac{1}{K_m}\right) \qquad \textit{Equation 4.1}$$

V_0 corresponds to the initial reaction velocity, K_m is the Michaelis-Menten constant, V_{max} denotes the maximum reaction velocity, and [S] is the substrate concentration.

4.2.6 Mechanism of peroxidase-mimicking activity of Cu-Pt@Fabrics

The mechanism of enzyme-mimicking catalytic activity of the Cu-Pt@Fabric NanoZyme was established by using a fluorescence assay that captures the hydroxyl radicals formed as a result of H_2O_2 degradation by Cu-Pt@Fabric. The assay involves terephthalic acid (TA) which forms a fluorescent 2-hydroxyterephthalic acid upon ·OH radical capture. This fluorescent product can be excited at 315 nm followed by measuring the emission between 325 and 550 nm on the CLARIOstar plate reader (BMG Labtech). The reaction system

involves 1 mM TA, 10 mM H_2O_2, and Cu-Pt@Fabric (0.5 cm × 0.5 cm) in 50 mM NaAc buffer (pH 5) at 37°C.

4.2.7 Colorimetric detection of glucose using Cu-Pt@Fabric

On the basis of the intrinsic peroxidase-mimic activity of the Cu-Pt@Fabric, a colorimetric glucose detection system was developed with the aid of glucose oxidase. The reaction system involved glucose (5-200 mM stock, 50 µL), 2 mg mL^{-1} glucose oxidase (50 µL), and 12.5 mM TMB (20 µL) in 50 mM NaAc buffer at pH 5 (380 µL). This reaction mixture was incubated for 20 min at 37 °C for the GOx to react with glucose. After 20 min, a piece of Cu-Pt@Fabric (0.5 cm × 0.5 cm) was added to the reaction mixture and further incubated for 30 minutes at 37 °C. The blue-colored oxidation product of TMB was measured at 652 nm. The linear dynamic range of the sensor system was determined by plotting the absorbance $\lambda_{652\ nm}$ against glucose concentration, which was then used to calculate the line of best fit using OriginPro 2016. Sensor parameters such as the limit of detection (LoD), precision, and accuracy were calculated. LoD was calculated using the formula 3.3*(SD of Y-intercept/slope). Accuracy was determined using the formula (n/N) × 100 at 10% confidence interval where n is the number of events that fall within the target response and N is the total number of test events. The sensor precision was determined using formula % Precision = 100 − %CoV where CoV is the coefficient of variation. The sensor specificity to detect glucose was assessed by exposing the system to glucose analogues such as maltose, lactose, sucrose, fructose, and galactose both independently and in combination. In each of these cases, the concentration of the analogue was twice (10 mM) that of glucose (5 mM).

Further, sensor capability to detect glucose in real samples such as urine was assessed by first collecting urine samples from a healthy and diabetic volunteer. The samples were

then centrifuged for 15 min at 14,500 RPM to remove any debris and then stored at 4 °C until used. Glucose detection was carried out by three methods.

Method 1: GOx-HRP: 50 µL urine sample, 50 µL of 2 mg mL^{-1} GOx and 20 uL of 12.5 mM TMB were incubated in 360 µL of 50 mM NaAc buffer at pH 5 for 20 min at 37 °C. To this reaction mixture, 20 µL HRP (40 ng mL^{-1}) was added and further incubated for 10 min at 37 °C. The oxidised product of TMB was measured at 652 nm.

Method 2: Cu-Pt@Fabric NanoZyme: the detection method is similar to what is described in method 1, except that the Cu-Pt@Fabric NanoZyme (0.5 cm × 0.5 cm) is added to the reaction mixture instead of HRP.

Method 3: Urine glucose dipstick: commercial test strips by Bayer – Diastix was exposed to urine samples for 30 sec followed by matching the color developed on the test pad with the reference color chart.

4.3 Results and discussion

4.3.1 Fabrication of Cu-M@Fabrics (M = Au, Ag, Pt, or Pd)

The Cu@Fabric was fabricated by synthesizing copper nanoparticles on individual threads of cotton fabric by an electroless deposition method as detailed in Chapter 3 [47]. In brief, the process involves the sensitization of the fabric with Sn^{2+} ions followed by the formation of Pd^0 nuclei through a galvanic replacement reaction between Sn^{2+} and Pd^{2+}. The Pd^0 nuclei increase the rate of copper deposition in the subsequent step by acting as a catalyst. Copper nanoparticles are formed on the fabric as a result of copper sulfate reduction in the presence of formaldehyde [60, 61]. The resulting Cu@Fabric was found to contain 615 ± 14 ppm equivalent of Cu ions on a 0.5 × 0.5 cm^2 cotton fabric. It is important to note that the amount of copper deposited in this case was higher than what was observed in Chapter 3. This is

because the size of the fabric used during the fabrication in the current chapter was smaller resulting in the deposition of copper nanoparticles on the edges of the fabric. The Cu@Fabric was then independently exposed to Au^{3+}, Ag^{+}, Pt^{4+}, or Pd^{2+} ions to synthesize bimetallic Cu-M@Fabrics (M = Au, Ag, Pt, or Pd) (**Figure 4.1**). The favourable reduction potentials between Cu^{2+}/Cu^{0} (0.342 V *vs* SHE), Cu^{+}/Cu^{0} (0.521 V *vs* SHE) and $AuCl_4^{-}/Au^{0}$ (0.85 V *vs* SHE) [62], Ag^{+}/Ag^{0} (0.799 V *vs* SHE) [35], $PtCl_6^{2-}/Pt$ (0.742 V *vs* SHE) [63] or $PdCl_4^{2-}/Pd^{0}$ (0.62 V *vs* SHE) [63] results in a spontaneous galvanic replacement reaction without any externally applied potential.

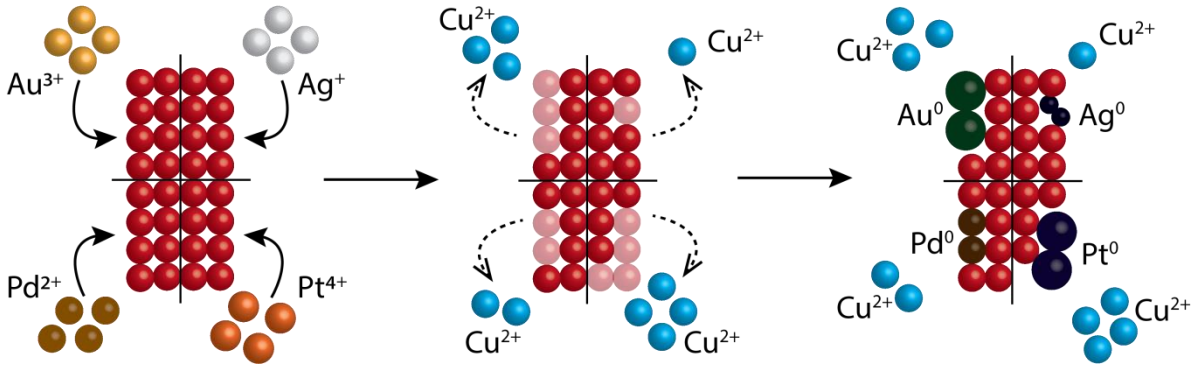

Figure 4.1 *A schematic representation of the galvanic replacement process on the surface of Cu@Fabric with either Au^{3+}, Ag^{+}, Pt^{4+} or Pd^{2+} to create bimetallic nanoparticles.*

It has been reported that galvanic replacement initiates at sites possessing high surface energy such as stacking faults, defects or steps [35]. When the Cu@Fabric is exposed to $AuCl_4^{-}$, Ag^{+}, $PtCl_6^{2-}$ or $PdCl_4^{2-}$, the Cu^{0} first oxidises to Cu^{2+} ions and dissolves into the solution thereby creating atomic vacancies on the Cu surface. The electrons thus generated then reduces $AuCl_4^{-}$, Ag^{+}, $PtCl_6^{2-}$ or $PdCl_4^{2-}$ to Au^{0}, Ag^{0}, Pt^{0}, or Pd^{0} seeds. The seeds then deposit epitaxially on the surface of copper nanoparticles due to the crystalline match between Cu and Au, Ag, Pt, or Pd (face-centered cubic structures). Such a deposition leads to the formation of Au, Ag, Pt or Pd nanoparticles on the surface of Cu obstructing the availability of underlying Cu^{0} atoms from reacting with further $AuCl_4^{-}$, Ag^{+}, $PtCl_6^{2-}$ or

$PdCl_4^{2-}$. However, the galvanic replacement reaction of the underlying Cu^0 continues *via* electron transfer through the exposed top layer. This leads to the formation of distinct clusters of Au, Ag, Pt or Pd on the surface of the Cu@Fabric [35]. It is important to note that the oxidation state of the metal ion that takes part in the galvanic replacement reaction determines the amount of Cu^{2+} ions that will be leached from the surface of the Cu@Fabric. In the case of Cu-Au, the oxidation state of Au is +3. Hence, three Cu ions are leached while simultaneously depositing two Au atoms. Similarly, for the Cu-Ag reaction, two Ag atoms deposit for every Cu ion leached. In the Cu-Pt reaction, for every four Cu ions leached, two Pt atoms deposit; while during the Cu-Pd reaction, for two Cu ions leached, two Pd atoms deposit on the Cu@Fabric.

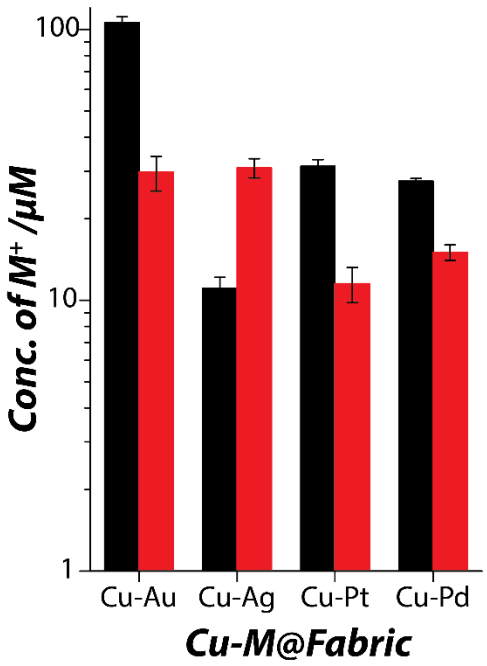

Figure 4.2 *Concentration of metal ions leached (Cu – Black) and metal deposited (M – red) on the Cu-M@Fabrics.*

The concentration of the Cu on the fabric post-galvanic replacement and the amount of deposited Au, Ag, Pt or Pd were quantified using AES (**Figure 4.2**). It was interesting to observe that the amount of copper leaching in each case varied depending on the noble metal

used in the reaction. However, it is important to note that in comparison to the theoretically expected Cu ion leaching, a higher concentration of Cu ion leaching during these experiments was observed. This suggests that the reaction between these metal ions and Cu facilitate additional leaching of Cu ions beyond that through the galvanic replacement reaction [36]. Therefore, one can assume that there is a complex interplay between the leaching of Cu ions and the concomitant deposition of noble metals on the surface of the Cu@Fabric.

4.3.2 Characterization of Cu-M@Fabrics

In agreement with the previous chapter and other reports [36, 47], the Cu@Fabric showed uniform deposition of quasi-spherical Cu nanoparticles of sub-100 nm diameter across the surface of the fabric (**Figure 4.3**a). Post galvanic replacement, the SEM images of the Cu-M@Fabrics containing the bimetallic nanoparticles showed increased surface roughness due to the deposition of quasi-spherical noble metal nanoparticles. In the case of Au, the nanoparticles showed a diameter of *ca*. 80-100 nm (**Figure 4.3**b), while in the case of Ag, the particle size was *ca*. 60-90 nm (**Figure 4.3**c). Similarly, Pd nanoparticles were of *ca.* 90-100 nm in diameter (**Figure 4.3**d) while Pt nanoparticles were *ca.* 60-70 nm (**Figure 4.3**e). These observations are similar to that observed in previous studies where a galvanic replacement reaction between Cu@Fabric and Au or Ag ions was used [36].

The deposition of the additional metal following the galvanic replacement reaction could also be observed visually. The fabrication of the Cu@Fabric results in a reddish colored fabric. Post galvanic replacement reaction, the fabric changed color from red to bluish-black after the deposition of Au nanoparticles, while a silvery-black color fabric was obtained after the deposition of Ag nanoparticles. These colors arise due to the collective surface plasmon resonance (SPR) absorption of Cu, Au, Ag nanoparticles and the

combinations of these [36]. The deposition of Pd nanoparticles imparts a dark brown color to the fabric while Pt nanoparticles changed the fabric to a greyish-black color.

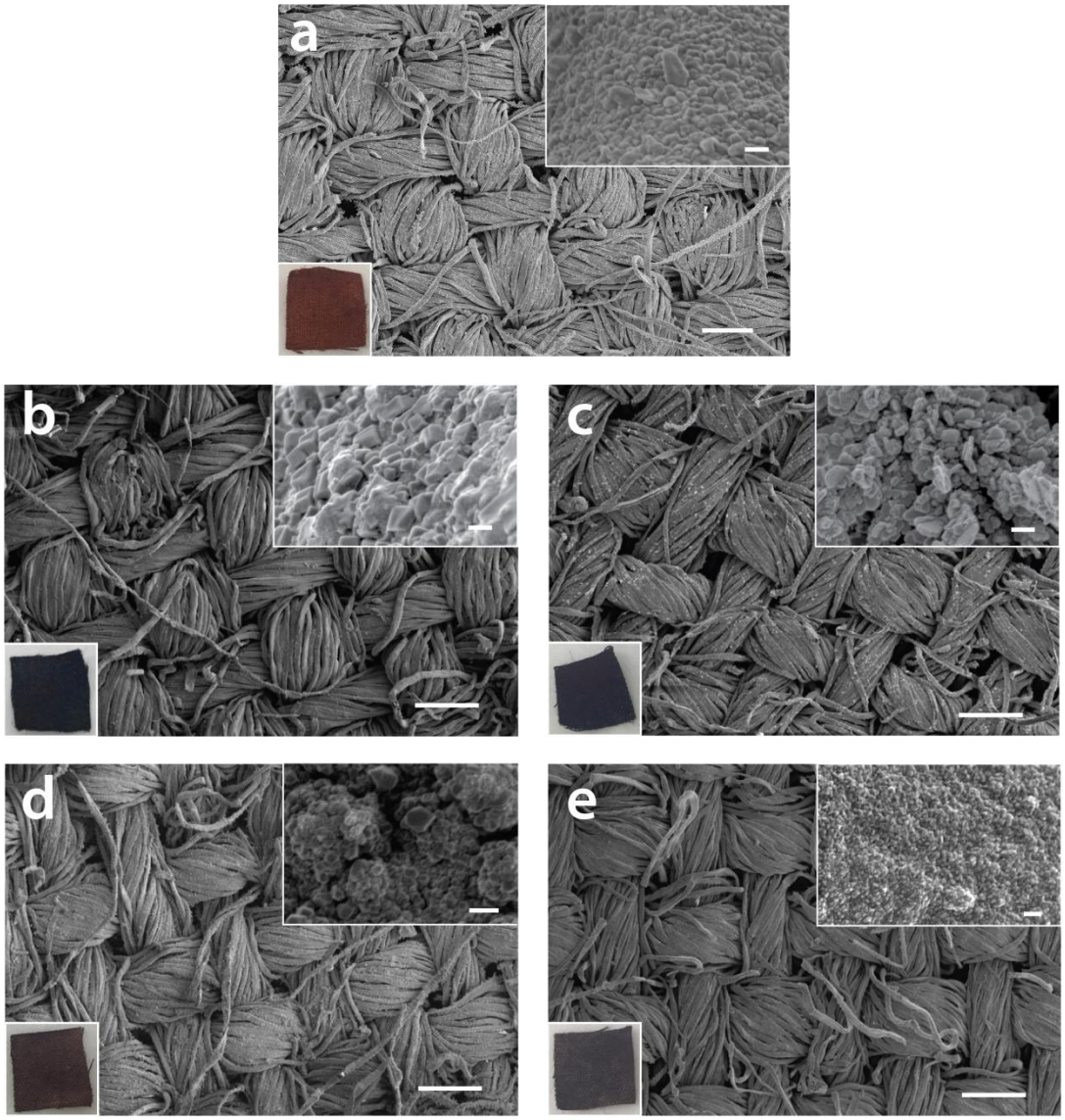

Figure 4.3 *SEM and optical images obtained for* ***(a)*** *Cu@Fabric,* ***(b)*** *Cu-Au@Fabric,* ***(c)*** *Cu-Ag@Fabric,* ***(d)*** *Cu-Pd@Fabric and* ***(e)*** *Cu-Pt@Fabric. Scale bars correspond to 200 µm for the main figure and 200 nm for the inset.*

EDX spectral analysis of the Cu-M@Fabric revealed characteristic energy lines of Cu Lα (0.93 keV) along with additional energy lines corresponding to the metal that makes up the bimetallic nanostructures (**Figure 4.4**). The Cu-Au@Fabric showed energy lines corresponding to Au M (2.123 keV and 1.64 keV) (**Figure 4.4**a) while Cu-Ag@Fabric

showed energy lines corresponding to Ag Lα (2.984 keV and 3.15 keV) (**Figure 4.4**b). The Cu-Pt@Fabric and Cu-Pd@Fabric showed characteristic energy lines arising from the Pd Lα (2.84 keV and 2.99 keV) (**Figure 4.4**c) and Pt M (2.07 keV and 2.33 keV) (**Figure 4.4**d), respectively. The EDX elemental mapping of the Cu-M@Fabrics showed that the bimetallic nanostructures were distributed evenly across the surface of the cotton fabric.

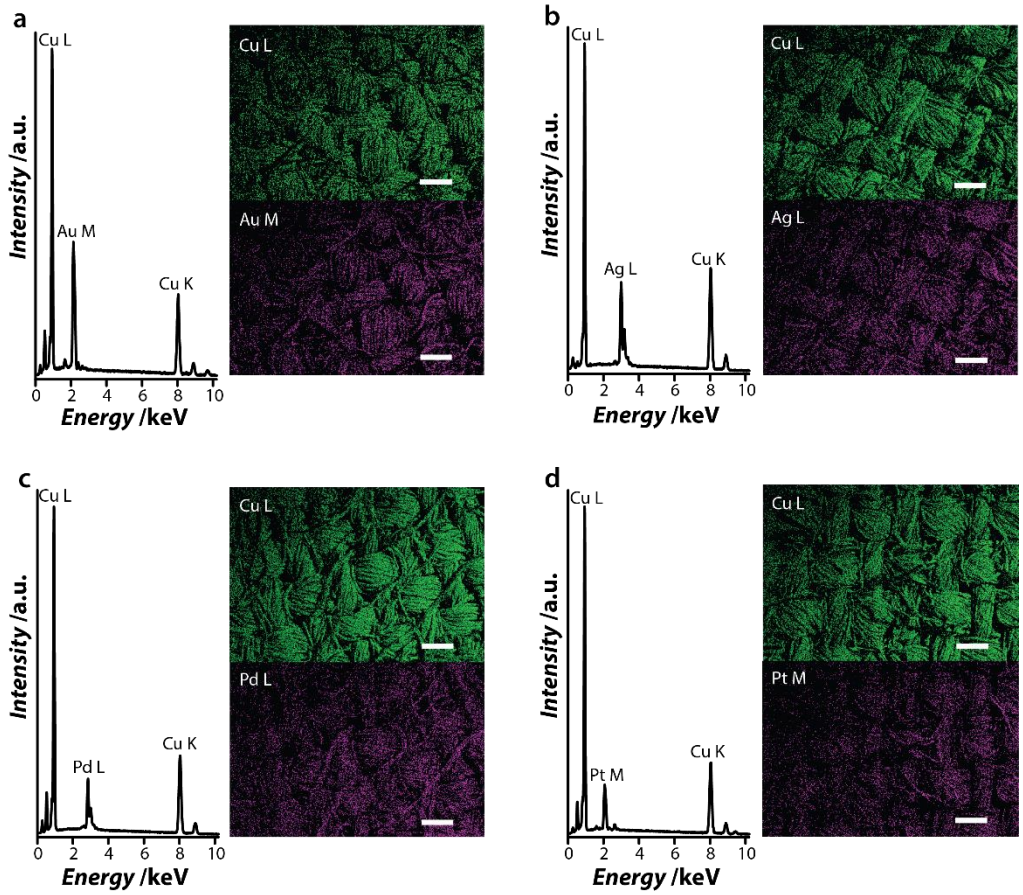

Figure 4.4 *EDX maps and spectra showing the elemental distribution of metal on* ***(a)*** *Cu-Au@Fabric,* ***(b)*** *Cu-Ag@Fabric,* ***(c)*** *Cu-Pd@Fabric and* ***(d)*** *Cu-Pt@Fabric. Scale bars correspond to 200 µm.*

The oxidation states of the Cu, Au, Ag, Pt, and Pd in cotton fabrics were confirmed using XPS analysis (**Figure 4.5**). As shown in the previous chapter, the pristine Cu@Fabric shows characteristic 2p3/2 and 2p1/2 splitting components (spin-orbit splitting ~19.7 eV) for Cu 2p core levels corresponding to zerovalent and Cu^{2+} oxidation states. Additionally, weak

satellite peaks were also observed suggesting the presence of surface oxides due to the propensity of pristine Cu to rapidly oxidise in air [48]. Following the galvanic replacement reaction, the Cu 2p core levels from the Cu-M@Fabrics show that the galvanic replacement reaction stabilizes the surface of the Cu@Fabric against potential surface oxidation. This is evident from the absence of the weak satellite peaks corresponding to copper oxides in the Cu 2p core level spectra of the Cu-M@Fabric (**Figure 4.5**a). Following the reaction with gold ions, the Cu-Au@Fabric shows additional Au 3d core levels with characteristic $4f_{5/2}$ and $4f_{3/2}$ splitting components (spin-orbit splitting ~3.7 eV) at *ca*. 84.6 eV and 88.3 eV. These corroborate well with Au in the zerovalent oxidation state (**Figure 4.5**b) [64]. The Ag 3d core level spectrum from the Cu-Ag@Fabric shows characteristic $3d_{5/2}$ and $3d_{3/2}$ splitting components (spin-orbit splitting ~6 eV) at *ca*. 368.2 eV and 374.2 eV, which corresponds to zerovalent metallic Ag (**Figure 4.5**c) [65]. Similarly, the Pd 3d and Pt 4f core level spectrum obtained from the Cu-Pd@Fabric and Cu-Pt@Fabric shows binding energies corresponding to zerovalent Pd and Pt, respectively. For Cu-Pd@Fabric, the spectrum shows $3d_{5/2}$ and $3d_{3/2}$ splitting components (spin-orbit splitting ~5.3 eV) at *ca*. 335.4 eV and 340.7 eV and , which corresponds to zerovalent metallic Pd (**Figure 4.5**d) [30], while for Cu-Pt@Fabric, the spectrum shows $4f_{5/2}$ and $4f_{3/2}$ splitting components (spin-orbit splitting ~3.4 eV) at *ca*. 71 eV and 74.4 eV and , which corresponds to zerovalent metallic Pt (**Figure 4.5**e) [66]. It is also important to note that the XPS analysis suggests that the galvanic replacement reaction, in fact, helps in stabilizing the surface of the Cu@Fabric against oxidation. This may have important implications in enhancing the stability of the Cu-M@Fabric during NanoZyme catalysis reactions.

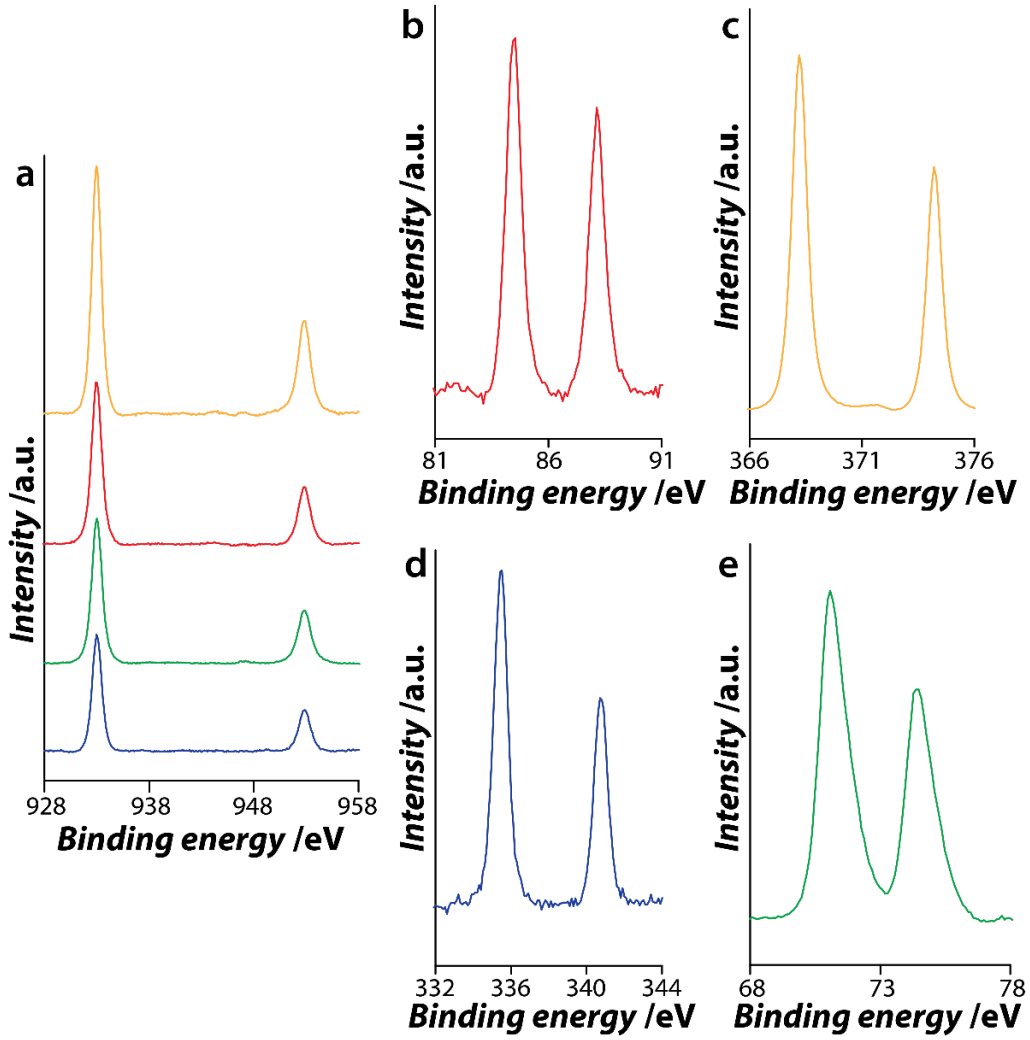

Figure 4.5 (a) *Cu 2p,* ***(b)*** *Au 4f,* ***(c)*** *Ag 3d,* ***(d)*** *Pd 3d, and* ***(e)*** *Pt 4f core levels obtained from the Cu-M@Fabrics (Cu-Au@Fabric – red, Cu-Ag@Fabric – yellow, Cu-Pd@Fabric – blue, and Cu-Pt@Fabric – green).*

4.3.3 Peroxidase-mimicking NanoZyme activity of Cu-M@Fabrics

The peroxidase-mimicking NanoZyme activity of the four Cu-M@Fabrics was assessed in comparison to that of Cu@Fabric using the colorless peroxidase substrate, TMB. Typically, the oxidation of TMB in the presence of an oxidising agent such as H_2O_2 results in a blue-colored product (λ_{max} = 652 nm) [67]. This charge-transfer complex is formed by the loss of a single electron and is the most commonly reported product when peroxidase-mimicking NanoZymes are used as the catalyst [4, 21]. In the current case, the Cu@Fabric, as well as the

other Cu-M@Fabrics were found to be capable of generating a blue-colored product within 5 minutes of the reaction specifically in the presence of H_2O_2 (**Figure 4.6**).

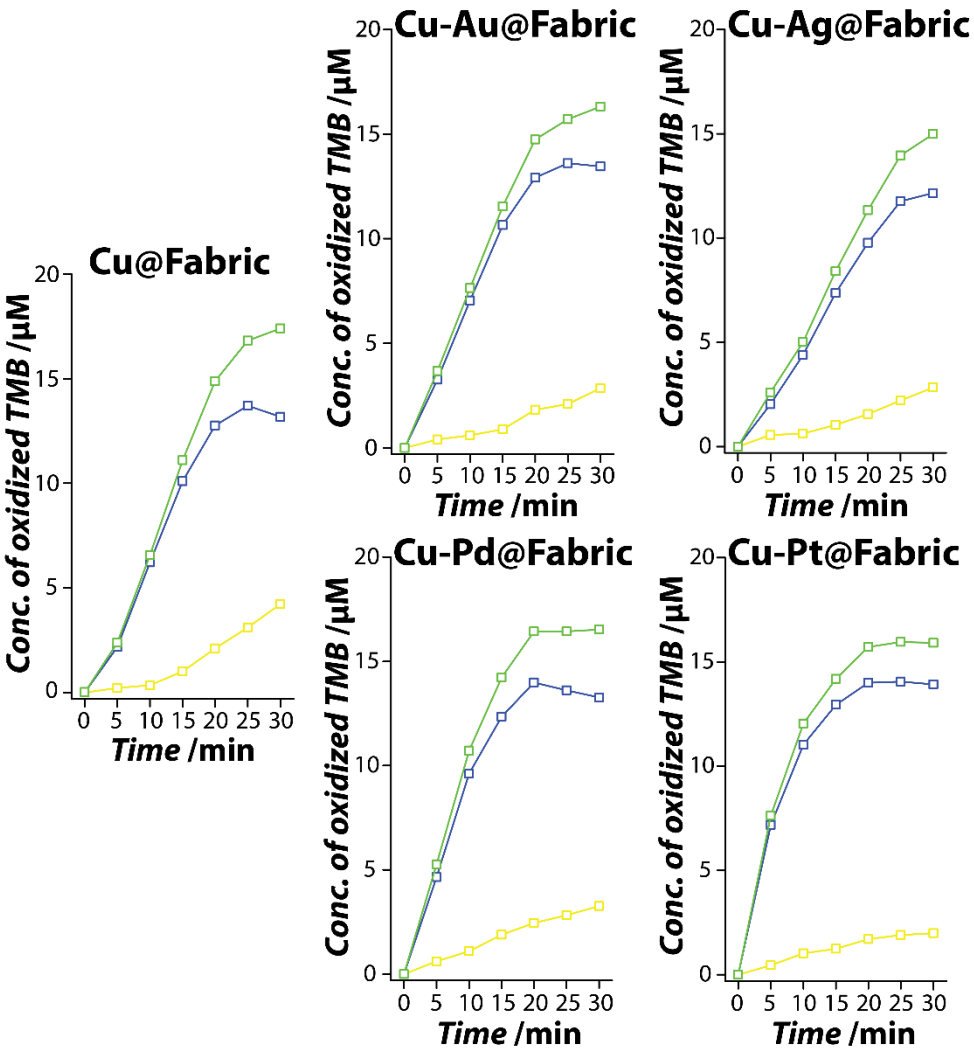

Figure 4.6 *NanoZyme performance of the Cu@Fabric (0.5 cm × 0.5 cm containing 615 ppm equivalent of Cu ions) and Cu-M@Fabrics. The concentration of charge transfer complex (blue) and diimine derivative (yellow) was calculated using absorbance values at* λ_{652nm} *and* λ_{450nm} *respectively. The total oxidised TMB product (green) is a sum of the two products.*

Given that the amount of copper nanoparticles on the fabric was higher than the Cu@Fabric in Chapter 3, a significant difference in the catalytic activity was observed when the Cu@Fabric was employed as a catalyst. For instance, the concentration of the diimine product was higher in the previous case. This suggests that the amount of copper

nanoparticles on the surface of the cotton textile plays an important role in promoting the catalytic reaction. This also provides some insights into the mechanism of catalysis. Copper nanoparticles have higher propensity to convert colourless TMB to its first oxidised product. There also exists an equilibrium state between the charge transfer complex and diimine derivative where at a particular point the copper nanoparticles tend to drive the reaction of the blue colored charge transfer complex to the yellow colored diimine derivative. Additionally, in the current case, the total concentration of oxidised product was approximately 1.5 times of that observed in the previous chapter further confirming that the amount of NanoZyme present on the surface of the fabric is an important aspect when employing these materials for promoting catalytic reactions.

In all cases, it can be observed that the Cu-M@Fabrics promote the oxidation of TMB, albeit with different efficiencies. For instance, comparing the activity between Cu-Au and Cu-Ag fabrics, the Cu-Ag@Fabric showed lower catalytic efficiency. In fact, among all the tested catalysts, the Cu-Ag@Fabric had the lowest catalytic efficiency. This is because Ag nanoparticles typically show lower catalytic performance in comparison with Cu nanoparticles (as outlined in Chapter 3 and in recent reports [21, 36, 47]). In all cases, the formation of the blue colored charge transfer complex product saturates within the first 15 min of the reaction with a total concentration of ~ 15 μM. While the conversion of this product to the yellow diimine derivative is dominant in the case of pristine Cu@Fabric, the galvanically replaced samples showed lower propensity to drive the second reaction. This may be due to the fact that following galvanic replacement reaction, the availability of catalytically active copper nanoparticles reduces. Among the bimetallic systems, the Cu-Pd@Fabric generated a significant amount of the diimine yellow product. It was also interesting to see that the Cu-Pt@Fabric showed higher catalytic activity than other systems having generated a product three times higher than that of Cu@Fabric within the first 5

minutes of reaction. The high catalytic activity of the Cu-Pt system could be associated with the additive effect of both the nanoparticles independently displaying excellent catalytic efficiency [10, 34]. Given that the Cu-Pt@Fabric has the highest initial rate of reaction, this NanoZyme system was chosen to further develop a urine glucose sensor system.

4.3.4 Standardization of peroxidase-mimicking assay parameters for Cu-Pt@Fabrics

For the efficient working of a sensor, it is important to standardize the optimum reaction parameters. To ensure that the oxidation of TMB is due to the intrinsic peroxidase-mimicking activity of Cu-Pt@Fabric, control experiments where the reaction mixture excluded either H_2O_2 or Cu-Pt@Fabric was performed. No color was generated in the absence of H_2O_2 indicating that Cu-Pt@Fabric could not catalyse the reaction. This suggests that the Cu-Pt@Fabric does not show oxidase-mimic reaction (**Figure 4.7**a). The peroxidase-mimicking activity of Cu-Pt@Fabric was further validated against other peroxidase substrates such as OPD (λ_{max} = 417 nm) and ABTS (λ_{max} = 420 nm). The Cu-Pt@Fabric NanoZyme was found to oxidise both substrates although the concentration of oxidised product was significantly lower than that of TMB (**Figure 4.7**b). The oxidised product of OPD was ~three times lower while the oxidation product was ~28 times lower than that of TMB in the case of ABTS suggesting that the Cu-Pt@Fabric NanoZyme favors positively charged substrates (TMB and OPD). The potential of leached metal (Cu and Pt) ions to catalyse the oxidation of TMB was assessed by incubating the Cu-Pt@Fabric in buffer solution followed by using this solution as a catalyst. Minimal catalytic activity was detected in comparison to the reaction catalysed by Cu-Pt@Fabric establishing that the NanoZyme activity is not the result of leached metal ions (**Figure 4.7**c). It is also important to note that in comparison to pristine Cu@Fabric, the Cu-

Pt@Fabric showed lower leaching confirming the high stability of the catalyst. This also suggests that the galvanic replacement reaction reduces the amount of copper leaching.

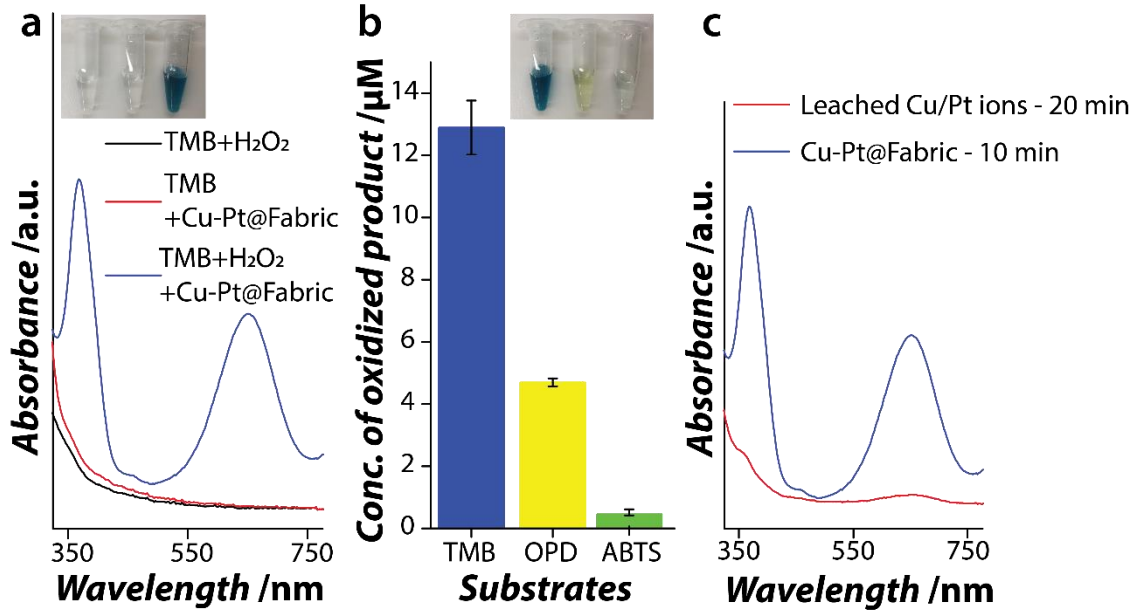

Figure 4.7 (a) *Absorbance spectra of Cu-Pt@Fabric catalysed oxidation product of TMB under different reaction condition (Inset is the optical image post-reaction);* ***(b)*** *Concentration of Cu-Pt@Fabric catalysed TMB, OPD, and ABTS oxidation products (Inset is the optical image post-reaction); and* ***(c)*** *Absorbance spectra of leached metal ions catalysed TMB oxidation product in comparison to that of Cu-Pt@Fabric.*

The catalytic activity of the Cu-Pt@Fabric NanoZyme was found to be dependent on the NanoZyme concentration, reaction pH and temperature. The concentration of the NanoZyme was varied by changing the weight of the Cu-Pt@Fabric. The amount of Cu and Pt in the reaction was varied from 220 – 870 ppm equivalent of Cu ions and 17 – 40 ppm equivalent of Pt ions. The catalytic activity was found to increase as the concentration of metal ions increased (**Figure 4.8**a). It was also interesting to see that the reaction favored the formation of the first oxidation product. The catalytic activity of Cu-Pt@Fabric NanoZyme was also found to be dependent on the reaction pH where the reaction was favorable at slightly acidic pH (4 and 5). Minimal activity was observed in basic and neutral conditions

(**Figure 4.8**b). This is in line with several other NanoZyme reports [3, 21]. The temperature at which the reaction proceeds also plays a major role in the rate of catalytic activity. This is unsurprising as inorganic catalysts are known to show higher catalytic activity with increasing the temperature of the reaction. For instance, at 60 °C, the concentration of the diimine derivative was almost equal to the concentration of the charge transfer complex; indicating a significant enhancement in catalytic efficiency with increasing temperature (**Figure 4.8**c). These observations suggest that the Cu-Pt@Fabric has excellent catalytic activity. Furthermore, as the nanoparticles are immobilized on a template, the reaction can be controlled by simply removing the piece of fabric from the reaction. Therefore, such a system can be called as 'free-standing'.

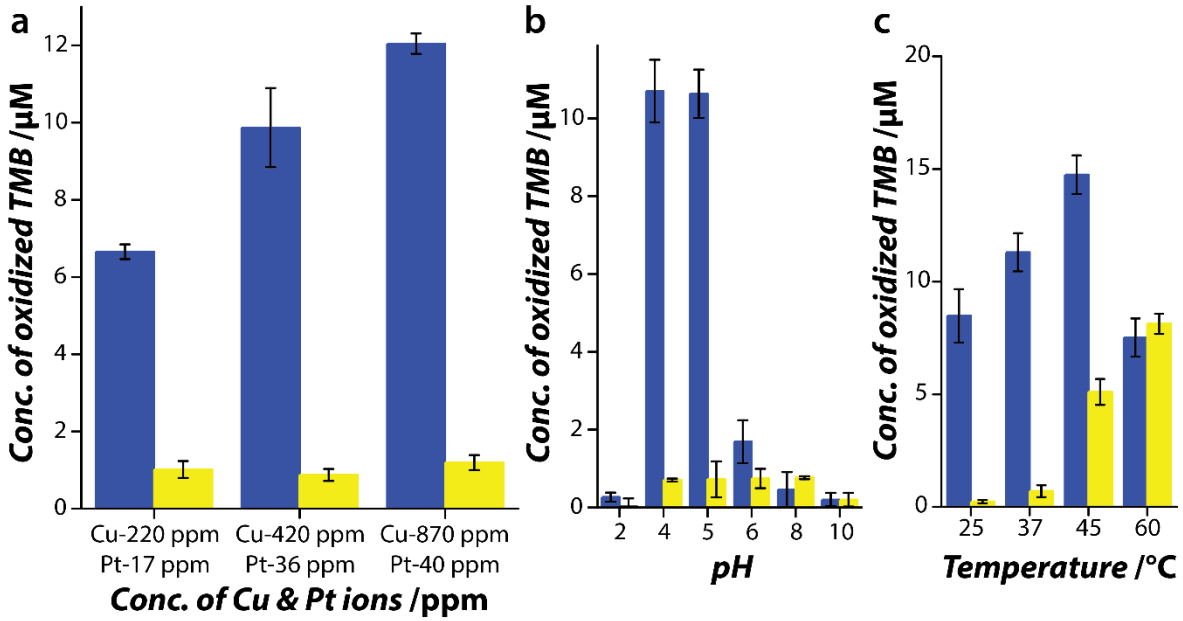

Figure 4.8 *Effect of* ***(a)*** *NanoZyme concentration represented as equivalent metal ion concentration (in ppm);* ***(b)*** *pH; and* ***(c)*** *temperature on the peroxidase-mimic activity of Cu-Pt@Fabric. The two oxidised products of TMB are represented as blue bars for charge transfer complex and yellow bars for diimine derivative.*

4.3.5 Steady-state kinetic parameters of Cu-Pt@Fabric NanoZyme

It is important to determine the steady-state kinetic parameters of the Cu-Pt@Fabric NanoZyme to understand how the sensing system will perform potentially. The Michaelis-Menten constant (K_m) and the maximum initial velocity of the reaction (V_{max}) were determined by evaluating the catalytic activity as a function of the substrate concentration (H_2O_2 and TMB). Lineweaver-Burk plot of the colorimetric responses allowed the calculation of the steady-state kinetic parameters such as K_m and V_{max} (**Figure 4.9**). As suggested in the previous chapter, K_m shows the affinity of the NanoZyme to the substrate while the V_{max} shows the maximum velocity i.e. how fast the reaction proceeds to generate colour [68].

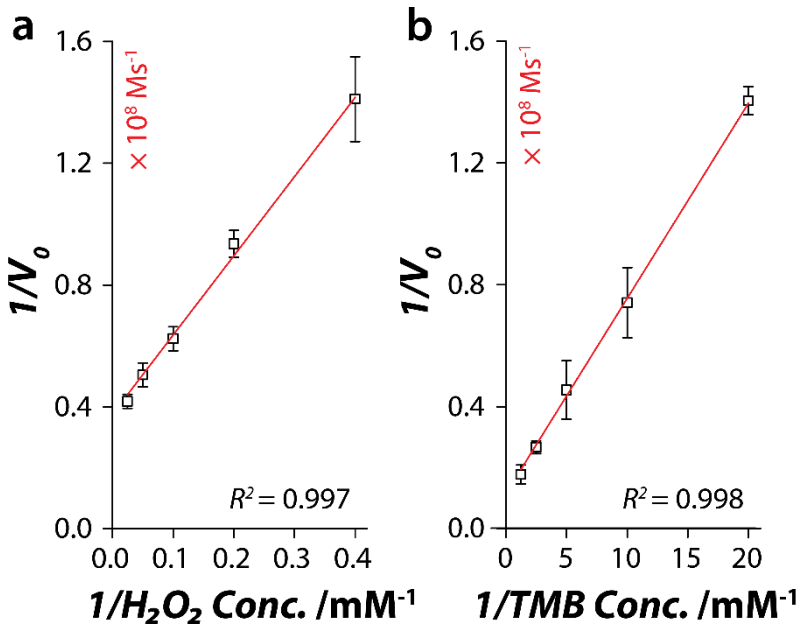

Figure 4.9 *Steady-state kinetic analysis using Lineweaver-Burk fit for the colorimetric response obtained by varying the concentration of* ***(a)*** *H_2O_2 and* ***(b)*** *TMB while keeping the other substrate concentration constant.*

Based on the fitting of the Lineweaver-Burk plots, the calculated *Km* of the Cu-Pt@Fabric for TMB increased in comparison to the Cu@Fabric (**Table 4.1**). However, the V_{max} for the reaction improved. This suggests that pristine copper nanoparticles have a higher

affinity to TMB substrate. This also corroborates well with the time-dependent kinetic study shown in **Figure 4.6** where the initial rate of reaction for the single-electron oxidation of TMB was favored. On the other hand, the affinity of the Cu-Pt@Fabric for H_2O_2 reduced significantly. This is critical for a sensor system as H_2O_2 is the rate-limiting factor for this reaction. This suggests that the sensor would, in fact, generate a more intense color when exposed to lower concentrations of H_2O_2 in comparison to pristine Cu nanoparticles. Additionally, the high surface area of cotton fabric leading to exposure of catalytic active sites and the high wettability and absorbency of the cotton fabric will enable the reactants to come in close contact with these catalytically active sites to improve the catalytic efficiency [36].

Table 4.1 *Comparison of the apparent K_m and V_{max}.*

Catalyst	TMB		H_2O_2	
	K_m / mM	V_{max} / 10^{-8} Ms^{-1}	K_m / mM	V_{max} / 10^{-8} Ms^{-1}
Free-standing Cu@Fabric	0.03	4.19	16.65	10.95
Free-standing Cu-Pt@Fabric	0.56	8.84	6.9	2.70

4.3.6 Mechanism of the peroxidase-mimicking activity of Cu-Pt@Fabric NanoZyme

In previously reported work involving Ag@Fabric NanoZyme [21] and in the previous chapter with Cu@Fabric as the NanoZyme, it was found that the degradation of H_2O_2 into hydroxyl radicals (·OH) was the main reason for the oxidation of the colorless peroxidase substrate to form the coloured product. To test if a similar reaction occurs in the case of Cu-Pt@Fabric, terephthalic acid as a fluorescent probe was used. The non-fluorescent TA reacted with the generated ·OH radicals to form a fluorescent 2-hydroxyterephthalic acid. This fluorescent product generated a signal at 435 nm when excited at 315 nm (**Figure 4.10**).

The intensity of fluorescence is a measure of the amount of ·OH radicals that will be generated in the reaction. The fluorescent signal was found to be significantly higher when the reaction consisted of both H_2O_2 and Cu-Pt@Fabric NanoZyme. Minimal response was observed in all other cases suggesting that the catalytic activity was due to the breakage of O-O bond in H_2O_2 by the Cu-Pt@Fabric generating the ·OH radicals [69].

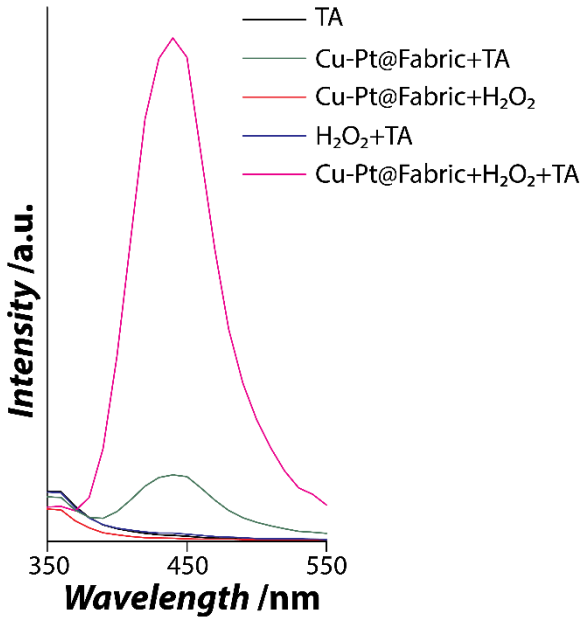

Figure 4.10 *Fluorescence emission spectra of terephthalic acid post-reaction under different reaction conditions recorded at an excitation wavelength of 315 nm.*

4.3.7 Colorimetric detection of glucose using Cu-Pt@Fabrics

Having established the important parameters that govern the catalytic activity of the Cu-Pt@Fabric NanoZyme, its ability to function as a glucose sensor was assessed. Glucose oxidase (GOx), a natural enzyme that catalyses the oxidation of glucose to gluconic acid while generating hydrogen peroxide [70], can be used to specifically detect glucose in a complex sample. The by-product of this reaction (H_2O_2) can then be used to indirectly quantify the concentration of glucose using a peroxidase-mimicking Cu-Pt@Fabric NanoZyme. Typically, in previous reports, glucose is first incubated with the GOx enzyme in

a neutral buffer to promote the oxidation of glucose. This is followed by the addition of an acidic buffer during the sensing event as NanoZymes are known to be highly active in acidic pH. The GOx used in the current case is obtained from *Aspergillus niger* and is known to have optimal catalytic activity at pH 5 [71]. Given that the optimum conditions for Cu-Pt@Fabric NanoZyme activity is also at pH 5, both these steps can be achieved in a single buffer system.

For the development of the sensor, the NanoZyme system was first exposed to a range of known glucose concentrations from 0 to 20 mM. The response was found to be linear between 1 and 12.5 mM glucose concentrations (**Figure 4.11**a). Although the lower limit of detection for the current sensor only starts at 1 mM in comparison to 0.5 mM obtained in the Cu@Fabric NanoZyme system, the color generated was significantly intense. This could be due to the fact that the Cu-Pt@Fabric favours the production of charge transfer complex (blue product) rather than double oxidising the substrate. This intense colour is convenient for naked-eye detection. The calculated limit of detection (LoD) was found to be 0.84 mM. Important sensor parameters such as accuracy and precision were determined by exposing the system to a glucose concentration of 5 mM, 15 times independently. The accuracy was found to be 100% at 10% contingency while the precision was 97.1%.

Further, the specificity of the sensor to detect glucose was assessed by exposing the sensor to glucose analogous independently as well as in combination with glucose. In all cases, the sensor showed high specificity towards detecting glucose with minimal response observed when exposed to glucose analogues such as maltose, lactose, sucrose, fructose, and galactose. Similarly, when the sensor was exposed to glucose in the presence of an analogue, the sensor response was found to be close to 100% indicating the high specificity of the system (**Figure 4.11**b). This is because the glucose oxidase enzyme is highly specific to oxidise glucose even in the presence of glucose epimer – galactose.

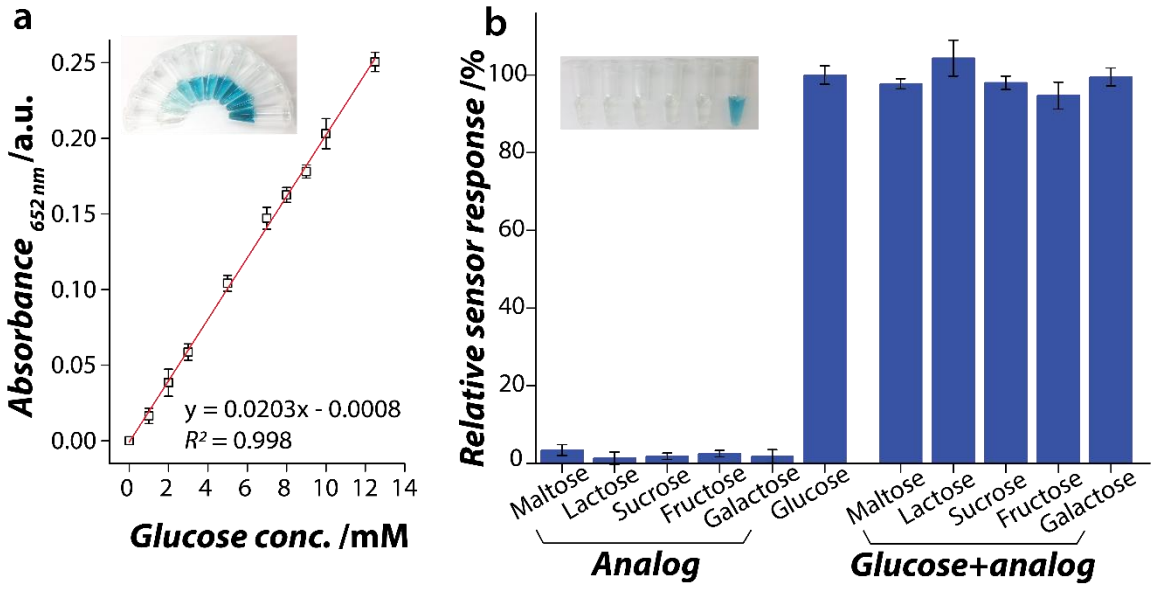

Figure 4.11 *Performance of Cu-Pt@Fabric as a glucose sensor.* ***(a)*** *Linear calibration plot obtained by exposing Cu-Pt@Fabric NanoZyme system to a series of glucose concentrations (Inset is the corresponding optical image).* ***(b)*** *The specificity of Cu-Pt@Fabric to detect glucose in the presence of glucose analogues independently and in combination with glucose. Inset is the optical image of glucose analogues and glucose post-reaction.*

The practical feasibility of the sensor was validated by using the sensor for the detection of glucose in human urine samples. Urine glucose monitoring is of significance in diabetic patients who have renal complications where glucose is eliminated in the urine [72]. To understand the performance of the NanoZyme system to detect glucose in urine samples, three approaches were used including GOx-HRP method and the newly developed NanoZyme method. Urine samples were collected from a healthy and diabetic patient. The glucose concentration in the urine of the healthy volunteer was first quantified by the gold standard GOx-HRP method. Given that there was no colour generation using the GOx-HRP method, it was assumed that there was no glucose in urine. Therefore, for all calculations, the concentration of urine was taken as 0 mM. Once this was established, the urine sample was spiked with known concentrations of glucose ranging from 1 to 10 mM. Following this, the sensor was used to quantify the amount of glucose in the spiked urine sample. **Table 4.2**

shows the estimated and the expected glucose concentration obtained from the Cu-Pt@Fabric NanoZyme system. In all the cases, recovery of 97-104% was obtained for tested concentrations showing the robustness of the sensor.

Table 4.2 *Glucose analysis in healthy volunteer urine sample post-spiking with known concentrations of glucose. The values in brackets are the corresponding standard deviation.*

Original amount (mM)[a]	**Glucose spiked (mM)**	**Expected (mM)**	**GOx-HRP approach**		**Cu-Pt@Fabric NanoZyme approach**	
			Est. glucose conc. /mM[b]	**Recovery (%)**[c]	**Est. glucose conc. /mM**[b]	**Recovery (%)**[c]
Undetectable (0 mM)[a]	0	0.0	0.00 (0.00)	100	0.00 (0.00)	100
	1	1.0	1.00 (0.05)	95-105	1.01 (0.03)	98-104
	2.5	2.5	2.51 (0.04)	99-102	2.53 (0.08)	98-104
	5	5.0	5.02 (0.15)	97-103	4.95 (0.10)	97-101
	7.5	7.5	7.46 (0.21)	97-102	7.48 (0.11)	98-101
	10	10.0	10.01 (0.18)	98-102	10.00 (0.1)	99-101

[a] Original amount of glucose calculated from GOx-HRP gold standard method.
[b] Standard deviation calculated from 5 independent experiments.
[c] Recovery calculated using (Measured value / Expected value) × 100.

Having established the high robustness of the NanoZyme sensing system to detect glucose in spiked urine samples, the ability of the sensor to detect glucose in a real sample was also evaluated by exposing the system to urine sample from a healthy and a diabetic volunteer (Type II diabetes). In this case, three independent methods were used to determine the concentration of glucose in urine including the gold standard GOx-HRP method, the newly developed NanoZyme method and a commercial urine test strip. Independent of the method used for detection, the urine from the healthy volunteer did not show any colour generation. For the diabetic volunteer, the GOx-HRP method estimated the glucose concentration to be 15.3 ± 0.01 mM. For the commercial urine test strips by Diastix, given that the system can easily overestimate the concentration glucose, this method estimated the glucose concentration to be approximately 28 mM. In contrast, the Cu-Pt@Fabric NanoZyme approach estimated the glucose concentration to be 15.28 ± 0.05 mM with a high recovery of

99-100% (even when compared to the GOx-HRP method) (**Table 4.3**). It should be noted that for the GOx-HRP method, the urine sample was diluted significantly to ensure that the sensor response falls within the linear dynamic range. However, the urine sample was not diluted before it was used for detection using the newly developed NanoZyme approach. The high recovery, low margin of error and the ability to detect glucose without diluting the urine sample outlines the high robustness of the NanoZyme sensor system to not only detect a biologically relevant concentration of glucose but also be unaffected by the complex matrix.

Table 4.3 *Comparison of glucose estimation in healthy and diabetic volunteer urine sample using laboratory gold standard (Glucose oxidase-horseradish peroxidase) and NanoZyme approach (Cu-Pt@Fabric). The values in brackets are the corresponding standard deviation.*

Method	**GOx-HRP approach**	**Cu-Pt@Fabric NanoZyme approach**		**Diastix urine sugar test strips**	
	Est. glucose conc. /mM[a]	**Est. glucose conc. /mM**[a]	**Recovery (%)**[b]	**Est. glucose conc. /mM**[a]	**Recovery (%)**[b]
Healthy volunteer	0.00 (0.00)	0.00 (0.00)	100	0	100
Diabetic volunteer	15.3 (0.01)	15.28 (0.05)	99.5-100.2	28	185

[a] Standard deviation calculated from 5 independent experiments.
[b] Recovery calculated using (Measured value / GOx-HRP method value) × 100.

4.4 Conclusions

In this study, a simple galvanic replacement approach for the synthesis of bimetallic NanoZymes on individual cotton threads intervowen into a 3D matrix of a cotton fabric is described. For the creation of these bimetallic systems, a low-cost metal (Cu) decorated with small quantities of expensive metal (Au, Ag, Pt, and Pd) was used. This simple strategy allows for the direct fabrication of nanostructures on porous, hierarchical 3D matrix of cotton fabrics. Given the ability to extract the material from a reaction on-demand, these bimetallic fabrics were labelled as ‘free-standing’. These free-standing bimetallic fabrics were found to

possess intrinsic peroxidase-mimicking NanoZyme activity. The decoration of small quantities of expensive metals on the surface of Cu resulted in high catalytic activity to oxidise peroxidase-substrate TMB whereby the reaction is favoured towards the generation of the blue charge transfer product in comparison to the yellow diimine product observed in the case of pristine Cu@Fabric. Of the different Cu-M@Fabrics, the Cu-Pt@Fabric showed highest catalytic activity. Given this observation, the Cu-Pt@Fabric was further used to create a colorimetric glucose sensor. The sensor showed outstanding performance to detect glucose in biologically relevant concentrations with low margin of error. Additionally, the high loading of nanoparticles meant that glucose concentrations as high as 12.5 mM could be detected in urine samples without any need for dilutions.

4.5 References

1. Wang, Q., H. Wei, Z. Zhang, E. Wang, and S. Dong, *TrAC, Trends Anal. Chem.*, 2018. **105**: 218-224.
2. Wang, X., Y. Hu, and H. Wei, *Inorg. Chem. Front.*, 2016. **3**(1): 41-60.
3. Wei, H. and E. Wang, *Chem. Soc. Rev.*, 2013. **42**(14): 6060-6093.
4. Wu, J., X. Wang, Q. Wang, Z. Lou, S. Li, Y. Zhu, L. Qin, and H. Wei, *Chem. Soc. Rev.*, 2019. **48**(4): 1004-1076.
5. Ishida, T., N. Kinoshita, H. Okatsu, T. Akita, T. Takei, and M. Haruta, *Angew. Chem. Int. Ed.*, 2008. **47**(48): 9265-9268.
6. Carnovale, C., G. Bryant, R. Shukla, and V. Bansal, *Prog. Mater. Sci.*, 2016. **83**: 152-190.
7. Singh, N., M.A. Savanur, S. Srivastava, P. D'Silva, and G. Mugesh, *Angew. Chem. Int. Ed.*, 2017. **56**(45): 14267-14271.
8. Liu, S., F. Lu, R. Xing, and J.J. Zhu, *Chem.: Eur. J.*, 2011. **17**(2): 620-625.
9. Liu, B. and J. Liu, *Nano Res.*, 2017. **10**(4): 1125-1148.
10. Lu, Y., W. Ye, Q. Yang, J. Yu, Q. Wang, P. Zhou, C. Wang, D. Xue, and S. Zhao, *Sens. Actuators, B*, 2016. **230**: 721-730.
11. Zhang, Z., X. Zhang, B. Liu, and J. Liu, *J. Am. Chem. Soc.*, 2017. **139**(15): 5412-5419.
12. Zhang, S., H. Li, Z. Wang, J. Liu, H. Zhang, B. Wang, and Z. Yang, *Nanoscale*, 2015. **7**(18): 8495-8502.

13. Kumar Sharma, T., R. Ramanathan, P. Weerathunge, M. Mohammadtaheri, H. Kumar Daima, R. Shukla, and V. Bansal, *Chem. Commun.*, 2014. **50**(100): 15856-15859.

14. Weerathunge, P., R. Ramanathan, R. Shukla, T.K. Sharma, and V. Bansal, *Anal. Chem.*, 2014. **86**(24): 11937-11941.

15. Weerathunge, P., R. Ramanathan, V.A. Torok, K. Hodgson, Y. Xu, R. Goodacre, B.K. Behera, and V. Bansal, *Anal. Chem.*, 2019. **91**(5): 3270-3276.

16. Karim, M.N., M. Singh, P. Weerathunge, P. Bian, R. Zheng, C. Dekiwadia, T. Ahmed, S. Walia, E. Della Gaspera, S. Singh, R. Ramanathan, and V. Bansal, *ACS Appl. Nano Mater.*, 2018. **1**(4): 1694-1704.

17. Wang, F., E. Ju, Y. Guan, J. Ren, and X. Qu, *Small*, 2017. **13**(25).

18. Neri, S., S.G. Martin, C. Pezzato, and L.J. Prins, *J. Am. Chem. Soc.*, 2017. **139**(5): 1794-1997.

19. Asati, A., C. Kaittanis, S. Santra, and J.M. Perez, *Anal. Chem.*, 2011. **83**(7): 2547-2553.

20. Pautler, R., E.Y. Kelly, P.J.J. Huang, J. Cao, B. Liu, and J. Liu, *ACS Appl. Mater. Interfaces*, 2013. **5**(15): 6820-6825.

21. Karim, M.N., S.R. Anderson, S. Singh, R. Ramanathan, and V. Bansal, *Biosens. Bioelectron.*, 2018. **110**: 8-15.

22. Singh, M., P. Weerathunge, P.D. Liyanage, E. Mayes, R. Ramanathan, and V. Bansal, *Langmuir*, 2017. **33**(38): 10006-10015.

23. Weerathunge, P., D. Pooja, M. Singh, H. Kulhari, E.L. Mayes, V. Bansal, and R. Ramanathan, *Sens. Actuators, B*, 2019: 126737.

24. Gao, L., K.M. Giglio, J.L. Nelson, H. Sondermann, and A.J. Travis, *Nanoscale*, 2014. **6**(5): 2588-2593.

25. Natalio, F., R. André, A.F. Hartog, B. Stoll, K.P. Jochum, R. Wever, and W. Tremel, *Nat. Nanotechnol.*, 2012. **7**(8): 530.

26. Walther, R., A.K. Winther, A.S. Fruergaard, W. van den Akker, L. Sørensen, S.M. Nielsen, M.T. Jarlstad Olesen, Y. Dai, H.S. Jeppesen, P. Lamagni, A. Savateev, S.L. Pedersen, C.K. Frich, C. Vigier-Carrière, N. Lock, M. Singh, V. Bansal, R.L. Meyer, and A.N. Zelikin, *Angew. Chem. Int. Ed.*, 2019. **58**(1): 278-282.

27. Weerathunge, P., T.K. Sharma, R. Ramanathan, and V. Bansal, *CHAPTER 23 Nanozyme-Based Environmental Monitoring*, in *Advanced Environmental Analysis: Applications of Nanomaterials, Volume 2*. 2017, The Royal Society of Chemistry. 108-132.

28. Zohora, N., D. Kumar, M. Yazdani, V.M. Rotello, R. Ramanathan, and V. Bansal, *Colloids Surf. A.*, 2017. **532**: 451-457.

29. Toshima, N. and T. Yonezawa, *New J. Chem.*, 1998. **22**(11): 1179-1201.

30. Harpeness, R. and A. Gedanken, *Langmuir*, 2004. **20**(8): 3431-3434.

31. Zhang, H., Y. Yin, Y. Hu, C. Li, P. Wu, S. Wei, and C. Cai, *J. Phys. Chem. C*, 2010. **114**(27): 11861-11867.

32. DeSantis, C.J., A.C. Sue, M.M. Bower, and S.E. Skrabalak, *ACS nano*, 2012. **6**(3): 2617-2628.

33. Habas, S.E., H. Lee, V. Radmilovic, G.A. Somorjai, and P. Yang, *Nat. Mater.*, 2007. **6**(9): 692.

34. Chen, S., S.V. Jenkins, J. Tao, Y. Zhu, and J. Chen, *J. Phys. Chem. C*, 2013. **117**(17): 8924-8932.

35. Xia, X., Y. Wang, A. Ruditskiy, and Y. Xia, *Adv. Mater.*, 2013. **25**(44): 6313-6333.

36. Anderson, S.R., A.P. O'Mullane, E. Della Gaspera, R. Ramanathan, and V. Bansal, *Adv. Mater. Interfaces*, 2019. **6**(16): 1900516.

37. Sabri, Y.M., S.J. Ippolito, A.J. Atanacio, V. Bansal, and S.K. Bhargava, *J. Mater. Chem.*, 2012. **22**(40): 21395-21404.

38. Pearson, A., A.P. O'Mullane, V. Bansal, and S.K. Bhargava, *Chem. Commun.*, 2010. **46**(5): 731-733.

39. Pearson, A., A.P. O'Mullane, S.K. Bhargava, and V. Bansal, *Inorg. Chem.*, 2012. **51**(16): 8791-8801.

40. Pearson, A., A.P. O'Mullane, V. Bansal, and S.K. Bhargava, *Inorg. Chem.*, 2011. **50**(5): 1705-1712.

41. Moon, G.D., S. Ko, Y. Min, J. Zeng, Y. Xia, and U. Jeong, *Nano Today*, 2011. **6**(2): 186-203.

42. Bansal, V., H. Jani, J. Du Plessis, P.J. Coloe, and S.K. Bhargava, *Adv. Mater.*, 2008. **20**(4): 717-723.

43. Bansal, V., A.P. O'Mullane, and S.K. Bhargava, *Electrochem. Commun.*, 2009. **11**(8): 1639-1642.

44. Hu, L., Y. Yuan, L. Zhang, J. Zhao, S. Majeed, and G. Xu, *Anal. Chim. Acta*, 2013. **762**: 83-86.

45. Hong, L., A.-L. Liu, G.-W. Li, W. Chen, and X.-H. Lin, *Biosens. Bioelectron.*, 2013. **43**: 1-5.

46. Chen, W., J. Chen, A.L. Liu, L.M. Wang, G.W. Li, and X.H. Lin, *ChemCatChem*, 2011. **3**(7): 1151-1154.

47. Anderson, S.R., M. Mohammadtaheri, D. Kumar, A.P. O'Mullane, M.R. Field, R. Ramanathan, and V. Bansal, *Adv. Mater. Interfaces*, 2016. **3**(6): 1500632.

48. Ramanathan, R., M.R. Field, A.P. O'Mullane, P.M. Smooker, S.K. Bhargava, and V. Bansal, *Nanoscale*, 2013. **5**(6): 2300-2306.

49. Lin, Y., J. Ren, and X. Qu, *Acc. Chem. Res.*, 2014. **47**(4): 1097-1105.

50. Pearson, A., S. Bhosale, S.K. Bhargava, and V. Bansal, *ACS Appl. Mater. Interfaces*, 2013. **5**(15): 7007-7013.

51. Darabdhara, G., B. Sharma, M.R. Das, R. Boukherroub, and S. Szunerits, *Sens. Actuators, B*, 2017. **238**: 842-851.

52. Zheng, C., A.-X. Zheng, B. Liu, X.-L. Zhang, Y. He, J. Li, H.-H. Yang, and G. Chen, *Chem. Commun.*, 2014. **50**(86): 13103-13106.

53. Han, L., C. Li, T. Zhang, Q. Lang, and A. Liu, *ACS Appl. Mater. Interfaces*, 2015. **7**(26): 14463-14470.

54. Wu, J., K. Qin, D. Yuan, J. Tan, L. Qin, X. Zhang, and H. Wei, *ACS Appl. Mater. Interfaces*, 2018. **10**(15): 12954-12959.

55. Ramanathan, R., S. Walia, A.E. Kandjani, S. Balendran, M. Mohammadtaheri, S.K. Bhargava, K. Kalantar-Zadeh, and V. Bansal, *Langmuir*, 2015. **31**(4): 1581-1587.

56. Ramanathan, R., A.E. Kandjani, S. Walia, S. Balendhran, S.K. Bhargava, K. Kalantar-zadeh, and V. Bansal, *RSC Adv.*, 2013. **3**(39): 17654-17658.

57. Mohammadtaheri, M., R. Ramanathan, S. Walia, T. Ahmed, P. Weerathunge, S.R. Anderson, M.R. Field, C.D. Dekiwadia, A.P. O'Mullane, and E. Della Gaspera, *Appl. Mater. Today*, 2018. **13**: 107-115.

58. Polavarapu, L. and L.M. Liz-Marzán, *Phys. Chem. Chem. Phys.*, 2013. **15**(15): 5288-5300.

59. Zheng, G., L. Polavarapu, L.M. Liz-Marzán, I. Pastoriza-Santos, and J. Pérez-Juste, *Chem. Commun.*, 2015. **51**(22): 4572-4575.

60. Mallory, G.O. and J.B. Hajdu, *Electroless plating: fundamentals and applications*. 1990: William Andrew.

61. Bindra, P. and J.R. White, *Fundamental aspects of electroless copper plating*, in *Electroless Plating Fundamentals & Applications*. 1990. 289-375.

62. Gao, C., Q. Zhang, Z. Lu, and Y. Yin, *J. Am. Chem. Soc.*, 2011. **133**(49): 19706-19709.

63. Zhang, H., M. Jin, J. Wang, W. Li, P.H. Camargo, M.J. Kim, D. Yang, Z. Xie, and Y. Xia, *J. Am. Chem. Soc.*, 2011. **133**(15): 6078-6089.

64. Guzman, J. and B.C. Gates, *J. Am. Chem. Soc.*, 2004. **126**(9): 2672-2673.

65. Gondikas, A.P., A. Morris, B.C. Reinsch, S.M. Marinakos, G.V. Lowry, and H. Hsu-Kim, *Environ. Sci. Technol.*, 2012. **46**(13): 7037-7045.

66. Liu, J., X. Hu, S. Hou, T. Wen, W. Liu, X. Zhu, J.-J. Yin, and X. Wu, *Sens. Actuators, B*, 2012. **166**: 708-714.

67. Josephy, P.D., T. Eling, and R.P. Mason, *J. Biol. Chem*, 1982. **257**(7): 3669-3675.

68. Jiang, B., D. Duan, L. Gao, M. Zhou, K. Fan, Y. Tang, J. Xi, Y. Bi, Z. Tong, and G.F. Gao, *Nat. Protoc.*, 2018. **13**(7): 1506.

69. Plauck, A., E.E. Stangland, J.A. Dumesic, and M. Mavrikakis. Active sites and mechanisms for H2O2 decomposition over Pd catalysts. in *Proc. Natl. Acad. Sci. USA*. 2016.

70. Wei, H. and E. Wang, *Anal. Chem.*, 2008. **80**(6): 2250-2254.

71. Weibel, M.K. and H.J. Bright, *J. Biol. Chem*, 1971. **246**(9): 2734-2744.

72. Fine, J., *Br. Med. J.*, 1965. **1**(5444): 1209-1214.

CHAPTER 5

Conclusions and future work

This chapter summarises the key findings of the current work and provides scope for potential future endeavours.

5.1 Summary

The work presented in this thesis outlines the applicability of free-standing peroxidase-mimicking Cu-based NanoZymes for glucose detection in urine. A simple approach combining electroless deposition and galvanic replacement reactions were employed for the fabrication of Cu and Cu-based bimetallic nanoparticles on individual cotton strands interwoven into a 3D matrix of cotton fabric. The high catalytic ability of Cu-based NanoZymes allowed the detection of glucose even in an undiluted sample of urine in the biologically-relevant concentration range outlining the robustness of the newly developed NanoZyme sensing system.

Chapter 3 focused on developing a NanoZyme with high catalytic ability and loading of high concentration of this NanoZyme to push the linear dynamic range of glucose detection into the biologically-relevant concentration. The chapter outlined the fabrication of a free-standing Cu@Fabric NanoZyme by an electroless deposition technique. The 3D interwoven matrix of the cotton fabric template, high porosity and absorbent nature of the fabric combined with the high catalytic activity of Cu nanoparticles allowed this system to show outstanding catalytic properties. The catalytic efficiency *i.e.,* the peroxidase-mimicking activity of Cu@Fabric showed, for the first time, the formation of both oxidation products of TMB. The NanoZyme system catalysed the reaction to first form the blue colored charge transfer complex and further pushed the reaction to generate the double oxidised diimine derivative yellow product of TMB without changing the reaction conditions. This product is typically only formed at highly acidic conditions of pH 1, as outlined during ELISA assay where a stopping reagent is added to obtain the yellow product. Owing to the high catalytic ability, the Cu@Fabric NanoZyme was used to quantify glucose initially in a buffer and then in human urine samples. The system showed the capability to detect glucose in the

biologically-relevant concentration of 1-15 mM. The robustness of the NanoZyme sensor was demonstrated by quantifying glucose in urine samples from both healthy and diabetic volunteer which showed high precision and accuracy even in a complex biological matrix of urine.

Although the Cu@Fabric NanoZyme system showed significant promise, further improvement was necessary to (i) obtain an intense colorimetric response, (ii) decrease the leaching of Cu from the fabric, and (iii) further reduce the margin of error. Considering that bimetallic nanoparticles can show enhanced properties than the individual counterparts, in Chapter 4, the Cu nanoparticles on the cotton fabric were used as a sacrificial template to deposit small quantities of expensive noble metals of Au, Ag, Pt, or Pd to create bimetallic nanoparticles on the surface of the fabric. This was achieved by a simple method of galvanic replacement where the nanostructures could be fabricated directly on the 3D matrix of cotton fabric. The free-standing bimetallic NanoZyme, in fact, showed higher peroxidase-mimicking catalytic activity over the Cu@Fabric NanoZyme. An interesting observation was that the bimetallic NanoZyme favoured the generation of the blue colored charge transfer complex over the diimine derivative. Among the different Cu-M@Fabrics (M = Au, Ag, Pt, or Pd), the Cu-Pt@Fabric showed the highest catalytic activity within a short span of time. Another important aspect that was observed was that the addition of noble metal prevented the oxidation of the Cu nanoparticles, which is otherwise prone to surface oxidation. Additionally, the addition of Pt also reduced the leaching of Cu ions from the surface during catalytic reactions. This reduced leaching allowed the system to detect urine glucose with higher recovery (99.5 – 100.2%) in comparison the Cu@Fabric NanoZyme outlined in Chapter 3 (97.6 – 99.7%). While the linear dynamic range decreased from 15 mM (Cu@Fabric) to 12.5 mM (Cu-Pt@Fabric), the intense colorimetric response (this may be due to the ability of the bimetallic NanoZyme system favouring the generation of the blue-colored

charge transfer complex product over the diimine derivative), improved sensor performance and eliminated the need for urine dilution, outlining the strength of the bimetallic NanoZyme.

5.2 Future work

The work shown in this thesis outlines a strategy to develop new free-standing NanoZyme systems that have outstanding catalytic properties. Although the field of NanoZymes has progressed significantly over the last decade, there is still a lack of fundamental understanding of how these systems work. For instance, the mechanism of H_2O_2 degradation by NanoZymes is still unknown and needs further in-depth understanding. Further, iron and copper ions are known to show Fenton-like reaction wherein the metal goes to a higher oxidation state while simultaneously reducing H_2O_2 to hydroxyl radicals. Considering that the NanoZyme system developed in the current work is in elemental state, it would be interesting to understand if the Cu nanoparticles are directly involved in the generation of hydroxyl radicals or if it the generation of localised Cu ions on the surface promotes the generation of hydroxyl radicals [1-3]. It was also evident that the NanoZymes used in the current work had particular preference for positively charged peroxidase substrates. This specificity towards some substrates is typically attributed to the surface charge of the NanoZyme. However, it would be interesting to determine if the NanoZymes have a similar response to other positively charged substrates that can either generate a colorimetric response or fluorogenic response. For instance, the ability of the NanoZyme to oxidise substrates such as 3,3'-Diaminobenzidine (DAB), pyrogallol, and Amplex Red can be probed and the affinity constants and kinetic parameters can be calculated to gain better understanding of the substrate specificity. Another aspect that needs further investigation is based on the fact that the field of NanoZymes has been focused primarily on peroxidase, oxidase, superoxide dismutase, and catalase-mimic enzyme activities. However, there are several other classes of

natural enzymes that have interesting catalytic properties. It is, however, an open question as to if the inorganic NanoZymes can promote other such catalytic reactions. Although there have been a few reports of other activities observed in NanoZymes in recent times [4, 5], a significant amount of investigation is required in this area to validate the universality of NanoZymes. One can, in fact, say that the field of NanoZymes is still at its infancy and needs significant research inputs to understand how NanoZymes work and in parallel establish a structure-function relationship between nanomaterials and their enzyme-mimicking ability.

In terms of glucose sensing, the work presented in this thesis has shown the capability of a low-cost template in enhancing the catalytic activity of NanoZymes due to increased loading of the nanoparticles, while the wettability and absorbency play an additional role to bring the substrates in the close vicinity of the catalytic site of the NanoZyme. This enhanced catalytic activity allows shifting the dynamic range of the sensor to detect glucose at biologically-relevant higher concentrations, in a complex matrix. Although the working of the sensor has been established, there is still a significant amount of work that needs to be done to develop a point-of-care device for sensing of glucose in urine. The current work uses a spectrophotometer to analyse the colorimetric response of the sensor. However, for a home-based detection kit, it is essential to quantify the intensity of color using a smartphone [6-8]. This will enable the user to not only get a qualitative response but also get a quantitative measure of glucose in urine. Developing such tools will expedite the pathway to commercialisation.

5.3 References

1. Gao, L., J. Zhuang, L. Nie, J. Zhang, Y. Zhang, N. Gu, T. Wang, J. Feng, D. Yang, and S. Perrett, *Nat. Nanotechnol.*, 2007. **2**(9): 577.
2. Wei, H. and E. Wang, *Anal. Chem.*, 2008. **80**(6): 2250-2254.
3. Shan, Z., M. Lu, L. Wang, B. MacDonald, J. MacInnis, M. Mkandawire, X. Zhang, and K.D. Oakes, *Chem. Commun.*, 2016. **52**(10): 2087-2090.

4. Walther, R., A.K. Winther, A.S. Fruergaard, W. van den Akker, L. Sørensen, S.M. Nielsen, M.T. Jarlstad Olesen, Y. Dai, H.S. Jeppesen, P. Lamagni, A. Savateev, S.L. Pedersen, C.K. Frich, C. Vigier-Carrière, N. Lock, M. Singh, V. Bansal, R.L. Meyer, and A.N. Zelikin, *Angew. Chem. Int. Ed.*, 2019. **58**(1): 278-282.

5. Jin, L., Y. Sun, L. Shi, C. Li, and Y. Shen, *J. Mater. Chem. B*, 2019. **7**(29): 4561-4567.

6. Chun, H.J., Y.M. Park, Y.D. Han, Y.H. Jang, and H.C. Yoon, *Biochip J.*, 2014. **8**(3): 218-226.

7. Roda, A., E. Michelini, M. Zangheri, M. Di Fusco, D. Calabria, and P. Simoni, *TrAC, Trends Anal. Chem.*, 2016. **79**: 317-325.

8. Lafleur, J.P., A. Jönsson, S. Senkbeil, and J.P. Kutter, *Biosens. Bioelectron.*, 2016. **76**: 213-233.